2021
Volume 4
Issue 2
ISSN: 2578-1995

CHARACTERIZATION AND APPLICATION OF NANOMATERIALS

https://systems.enpress-publisher.com/index.php/CAN

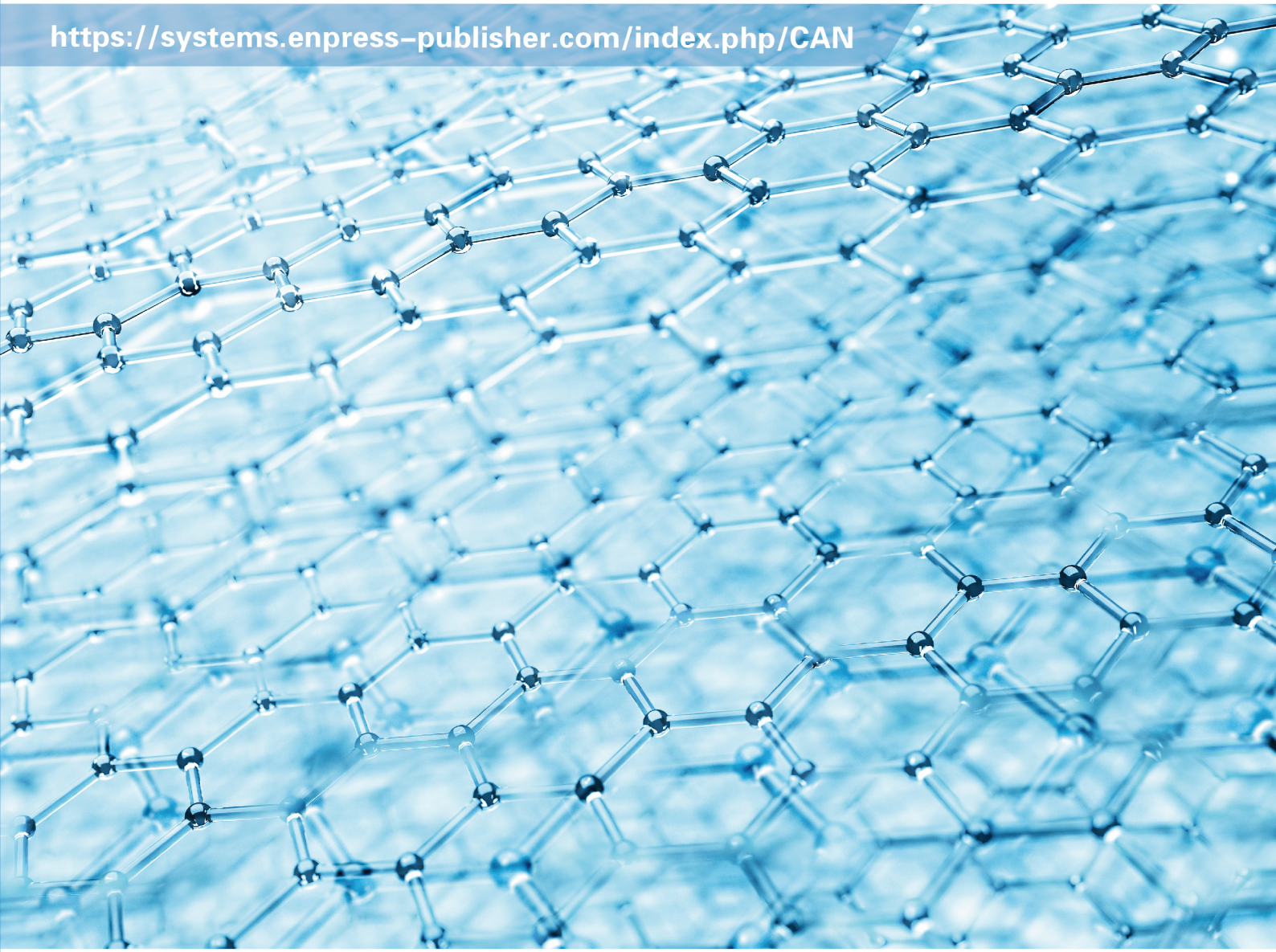

CAN

ISSN 2578-1995
02
9 772578 199042

EnPress Publisher

Editorial Board

Editor-in-Chief

Editorial Board Member

Volume 4 Issue 2 • 2021

Characterization and Application of Nanomaterials

EnPress Publisher

2021 | Volume 4 | Issue 2

Characterization and Application of Nanomaterials

https://systems.enpress-publisher.com/index.php/CAN

Contents

Original Research Articles

Review Article

Characterization and Application of Nanomaterials (2021) Volume 4 Issue 2
doi:10.24294/can.v4i2.1293

ORIGINAL RESEARCH ARTICLE

Sapindus emarginatus extract embedded with gold nanoparticles: An antiproliferative agent against MCF7 breast cancer cell line

S Vignesh Kumar[1*], V Kavimani[2]

[1] *Department of Biotechnology, Anna University Regional Centre, Coimbatore, India. E-mail: svigneshkum6@gmail.com*

[2] *Department of Mechanical Engineering, Anna University Regional Centre, Coimbatore, India*

ABSTRACT

There are numerous studies reported on the usage of the sapindus emarginatus (SE) fruit in cancer and other treatments in the past few years. In this study, crude SE fruit extract was prepared and it was further used to synthesis gold nanoparticles (Au Nps). The synthesized Au Nps were left embedded in the SE fruit extract. The Au Nps embedded in the SE fruit extract (SE-Au Nps) were characterized using UV-Visiable Spectroscopy, Centrifugal Particle Size analyzer (CPS), Scanning Electron Microscope (SEM) and Fourier Transform Infrared Spectroscopy (FTIR). MTT assay was carried out for both SE fruit extract and SE-Au Nps on MCF7 breast cancer cell line and thus compared. The UV-Visible Absorbance for the SE-Au Nps was obtained at 543 nm. The centrifugal particle size analysis of the Au Nps embedded in SE fruit extract showed the size of the nanoparticles to be widely varying with higher fraction of particles between the size ranges of 15 to 20 nm. The morphology of the Au Nps embedded in SE fruit extract was observed using SEM. The presence of Au Nps in SE fruit extract was confirmed using FTIR. The results of the MTT assay on MCF7 breast cancer cell line proved that the % cell viability was less for SE-Au Nps than that of the SE fruit extract alone. Thus, the antiproliferative activity of the SE fruit extract was significantly enhanced by embedding it with Au Nps and it can be effectively used in therapeutic applications after further studies.

Keywords: Gold Nanoparticles; Sapindus Emarginatus; Antiproliferative; MCF7

ARTICLE INFO

Received: 25 March 2021
Accepted: 11 May 2021
Available online: 18 May 2021

1. Introduction

Cancer is the abnormal growth of cells with uncontrolled division resulting in increased number of cells[1]. Cancer is observed as the most dangerous class of disease categorized by uncontrolled cell growth[2,3]. There is a marginal increase in cancer cases in the last few years, and most of the time, it ends up with taking life[4,5]. Breast cancer is a complex and heterogeneous disease[6]. In world, breast cancer represents 9% of the global cancer burden and is the third most common tumour. Human breast cancer MCF7 cells represent one of the most widely used experimental models for *in vitro* studies on breast carcinoma[7].

A considerable part of the current knowledge on breast carcinomas is based on *in vivo* and *in vitro* studies performed with cell lines derived from breast cancer. In reference to the treatments available for cancer, the characteristics of the cancer determine the treatment, which may include surgery, medications (hormonal therapy and chemotherapy), radiotherapy and immunotherapy. There are currently three main

groups of medications for breast cancer, such as hormone blocking agents (Tamoxifen, Anastrozole or Letrozole), chemotherapy (cyclophosphamide, methotrexate and fluorouracil) and monoclonal antibodies (Trastuzumab). Radiotherapy is given after surgery to the region of the tumor bed and regional lymph nodes, to destroy microscopic tumor cells that may have escaped surgery. Radiation can reduce the risk of recurrence by 50%–60%[8]. Most chemotherapy medications work by destroying fast-growing and/or fast-replicating cancer cells, either by causing DNA damage upon replication or by other mechanisms. Along with the medications chemotherapy and radiation can also affect healthy cells. For example, damage to the heart muscle is the most dangerous complication of doxorubicin. Trastuzumab is very expensive and its use may cause serious side effects (approximately 2% of patients who receive it suffer from significant heart damage). Due to growing resistance and side effects to these therapies search for new therapeutics for breast cancer has become essential. Scientific interest in medicinal plant has bloomed in recent times due to increased efficiency of new plant derived drugs and wide spread concerns about the side effects of modern medicine[9].

Sapindus emarginatus Vahl found in South India is commonly known as soap nut tree. The tree species is inadequately distributed in diverse geographical provinces like Gangetic plains, Western Ghats and Deccan Plateau in India[10]. The genus Sapindus possesses tremendous medicinal value. Since past, it is used as emetic, tonic, astringent, anthelmintic, for asthma, colic, diarrhea, cholera, tubercular glands and paralysis of limbs. Methanolic extract of fruit of Sapindus emarginatus (SE) found to produce CNS depressant activity[11]. The fruits are usually used for hair problems and also in preparation of shampoos. Traditionally SE is used as anti-inflammatory and antipruritic medicine. The seed is an intoxicant and the fruit rind has oxytropic action. Its powder is used as nasal insufflations[12]. Saponins isolated from different plants and animals have been shown to specifically inhibit the growth of cancer cells *in vitro*[13–18]. The saponins from SE fruit extract found to have significant antihyperlipidemic activity[19].

The combined application of saponins with other antitumor compounds may increase cytotoxic activity of the latter, which is an interesting new possibility in cancer treatment research[20]. The noble metal nanoparticles like gold nanoparticles represent smart and promising candidates in the drug delivery applications due to their unique dimensions, tunable functionalities on the surface, and controlled drug release[21]. Another essential aspect while working with Au NP in bio-applications is safety and biocompatibility (Au NP is already approved by the US Food and Drug Administration.) Biologically synthesized and functionalized, Au NP provides many desirable attributes for use as carriers in drug delivery systems as the functionalized Au NP core is essentially inert and nontoxic reported in recent studies[22]. The labeling of AuNPs with biological ligands to specifically bind to desired cancer cells increases the effectiveness of thermal energy transfer to cancer cells without harming non-cancerous cells[23]. After cellular uptake, the Au Nps can act as tiny, precise and powerful heaters (thermal scalpels) to kill cancer and they are capable of inducing apoptosis in B-chronic lymphocytic leukemia[24].

It has been found that gold nanoparticles embedded in Rubia cordifolia (RC) matrix significantly enhanced anti-inflammatory characteristics by inhibiting nitric oxide release[25]. It was reported in terms of inhibitory concentration for 50% inhibition compared to either RC extract or Au NPs. Hence, in this work the SE fruit extract was embedded with gold nanoparticles with the vision of increasing its antiproliferative activity.

2. Materials and methods

2.1 Preparation of plant extract

Fresh fruits of SE were collected from the nursery of Institute of Forest Genetics and Tree Breeding (IFGTB), Coimbatore, Tamilnadu. Collected SE fruits were dried under shade, mechanically powdered and stored in an airtight container. Dried and powdered SE fruits were extracted with 95% methanol in a Soxhlet extractor. The methanolic extract was concentrated to give a dark brown residue which

was partitioned between water-n-Butanol (1:1). The n-butanolic layer was evaporated to give the crude saponin fraction as a brown residue[26].

2.2 Synthesis of gold nanoparticles (Au NPs) embedded in SE fruit extract (SE-AU NPs)

A solution of 50 ml, 0.001 M (0.39382 mg/ml) gold (III) chloride trihydrate ($HAuCl_4 \cdot 3H_2O$) and 50 ml SE fruit extract, diluted in 50 ml of distilled water, was added together drop by drop and stirred on a magnetic stirrer. The solution was ultrasonicated at a high frequency of 10 KHz for 3 h and then maintained at a stationary position for 2 h at room temperature.

2.3 Characterization of SE-AU NPs

SE-Au Nps were characterized by UV-Visible Absorption Spectroscopy, Centrifugal Particle Size analyzer (CPS), Fourier Transform Infrared Spectroscopy (FTIR) and a Scanning Electron Microscope (SEM).

2.4 UV-Visible Absorptance Spectroscopy studies

UV-Visible Absorptance Spectroscopy have been proved to be quite sensitive to the formation of gold colloids because gold nanoparticles exhibit an intense absorption peak around 540 nm due to the surface plasmon (it describes the collective excitation of conduction electrons in a metal) excitation. The sample was analyzed using UV-9000S Spectrophotometer (Lark, India). Distilled water was used as a blank.

CPS

The gold nanoparticles embedded in the plant extract were isolated by centrifugation. Diluted suspensions of sucrose, on the order of 0.01–1.0 [wt%], were prepared. The sugar solution and our sample solutions were injected in disc centrifuge. Nanoparticle size was analyzed by injection of 350 µl of sample into CPS operating at a speed of 20,000 rpm. All analyses were run against a known calibration standard and the particles in the solution were analyzed by size distribution graph.

SEM

Morphology of the synthesized Au Nps in the SE fruit extract was analyzed using SEM. Few drops of the SE fruit extract embedded with the Au Nps was spread on a cover slip and dried. Then the sample on the cover slip was coated with gold in a sputter coating unit for few minutes.

FTIR

The samples were completely dissolved in respective solvents, non-sticky and the pH was found to be less than 8 which are necessary conditions to analyze the liquid samples. The sample analysis was carried out using FTIR (Brucker–Tensor 27) in ATR mode with a range from 500 to 4000 cm^{-1}. The liquid samples are directly placed onto the ZnSe crystal to obtain the spectrum.

3. Cell proliferation assay on MCF7 cell line

3.1 Chemicals and reagents

MTT (3-[4,5-dimethylthiazol-2-yl]-2,5-diphenyl tetrazolium bromide) Invitrogen, USA. Acridine orange was obtained from Sigma, USA. All other fine chemicals were obtained from Sigma–Aldrich, St. Louis.

3.2 Cell culture

MCF7 cells obtained from NCCS (National Centre for Cell Science, Pune) were cultured in Rose well Park Memorial Institute medium (RPMI), supplemented with 10% fetal bovine serum, penicillin/streptomycin (250 U/ml), gentamycin (100 µg/ml) and amphotericin B (1 mg/ml) were obtained from Sigma Chemicals, MO, USA. All cell cultures were maintained at 37 °C in a humidified atmosphere of 5% CO_2. Cells were allowed to grow to confluence over 24 h before use.

4. Cell growth inhibition studies by MTT assay

Cell viability was measured with the conventional MTT reduction assay, as described previously with slight modification. Briefly, MCF7 cells were

seeded at a density of 5 × 103 cells/well in 96-well plates for 24 h, in 200 µl of RPMI with 10% FBS. Then culture supernatant was removed and RPMI containing various concentrations (0.11–100 µg/ml) of test compound was added and incubated for 48 h. After treatment, cells were incubated with MTT (10 µl, 5 mg/ml) at 37 °C for 4 h and then with DMSO at room temperature for 1 h. The plates were read at 595 nm on a scanning multi-well spectrophotometer. Data represented the mean values for six independent experiments[27]. Cell viability (%) = (Mean OD/ Control OD) × 100.

5. Results and discussion

5.1 Preparation of SE fruit extract

Crude extract of SE fruits was obtained as brown colored mixture from the Soxhlet apparatus. The mixture was separated into upper phase (butanol and crude saponin) and lower phase. The upper phase was evaporated and the crude saponin obtained was brown in color with a colorless lower phase.

5.2 Synthesis of SE-AU NP

The change in the brown color of SE fruit extract into purple color after its treatment with $HAuCl_4 \cdot 3H_2O$ solution clearly indicated the formation of Au Nps. The color change was observed within 1 h in room temperature. Jannathul Firdhouse and Lalitha have earlier reported the similar color change as the indicator for the formation of Au Nps[28]. The reduction of metal ions was roughly monitored by visual inspection as described earlier[29]. The process performed simply at room temperature is comparatively free of toxic chemical hazards.

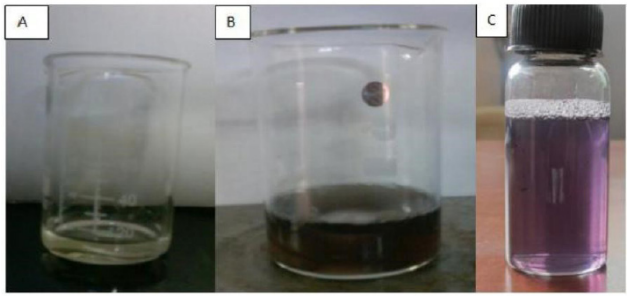

Figure 1. Synthesized Au Np. **(A)** $HAuCl_4 \cdot 3H_2O$; **(B)** Plant Extract + $HAuCl_4 \cdot 3H_2O$; **(C)** SE-Au NP.

5.3 Characterization of SE-Au Nps UV-Visible Spectroscopy

The UV-Visable Absorbance for the SE-Au Nps was obtained at 543 nm and it is due to the excitation of surface plasmon vibrations in the gold nanoparticles. The spectra are consistent with previous experimental results. Parida *et al.* reported the synthesis of gold nanoparticles using Allium cepa extract as the reducing agent and the absorption peak was broad and found at 540 nm which might be due to polydispersity nature of the nanoparticles[30].

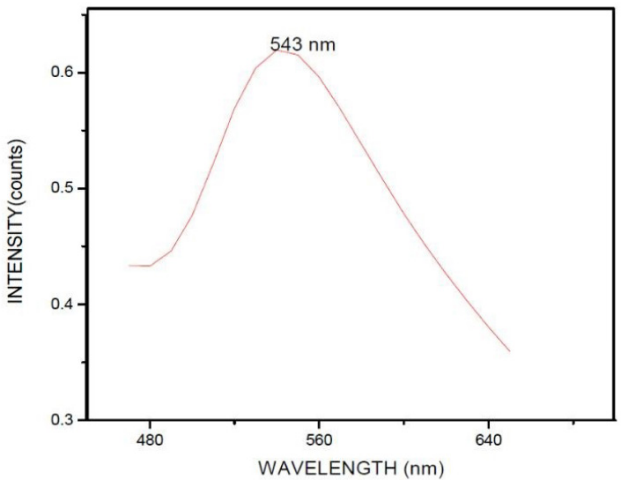

Figure 2. UV-Visible Spectroscopy for SE-Au NPs.

CPS

The particle size analyzer (**Figure 3**) showed various diameter ranges of nanoparticles. The diameter versus % fraction was plotted. The size of the Au Nps embedded in SE fruit extract was found to be widely varying with higher fraction of particles between the size ranges of 15 to 20 nm.

The particle size analyzer displayed a total weight of injected gold sample as 57.26 µg. In the injected sample 20 to 15.9 nm diameter of particles are present in high level whereas the 15.9 to 12.7 nm sized particles were in minimum level. This variation may be due to the aggregation of the nanoparticles in the extract.

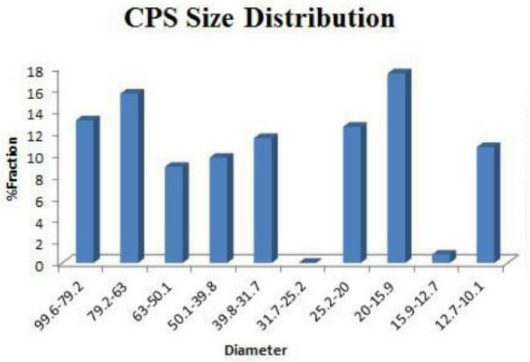

Figure 3. Particle size distribution of Au NPs.

SEM

The SEM image (**Figure 4**) of SE-Au Nps showed the Au Nps distributed over the extract. The Au Nps embedded in the SE fruit extract were found to be aggregated and was not clear. The result obtained was similar to that of Paz Elia *et al.* who observed the morphology of Au Nps using plant extracts as reducing agents[31].

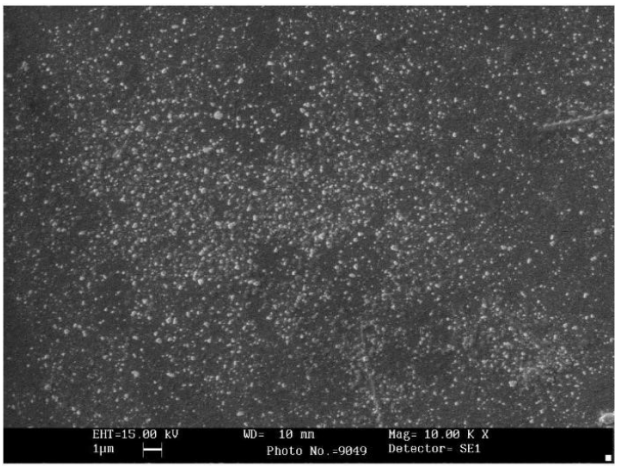

Figure 4. SEM image of SE-Au Nps.

FTIR

FTIR spectrum of methanolic fruit extract of SE showed characteristic peaks for several functional groups like hydroxyl group in the range 3500 to 3000, C-O-C in the range of 1500 to 1000 and C-Br (alkyl) in the range of 1000 to 500. For SE-Au Nps the peak in the range of 3500 to 3000 indicates the presence of -NH_2 (amino) group, C-H group at 2119 and carbonyl group C=O in the range of 2000 to 2500. By comparing the spectrum of SE-Au Nps with the spectrum of SE fruit extract and the standard spectrum of gold nanoparticles[32], it is clear that the spectra of SE embedded with gold nanoparticles indicates the presence of both the extract and the gold nanoparticle in it.

6. Cell proliferative study—MTT assay

The antiproliferative activity of SE fruit extract and SE-Au Nps under in vitro conditions were examined on cell proliferation by the MTT assay. MCF-7 cells were exposed to the two samples at varying concentrations for 48 h and cytotoxicity was determined using MTT assays. MTT results have shown that as the concentration of the samples increase, increased cytotoxicity was observed in a dose-dependent manner. In MTT assay, cell viability was significantly reduced to 47, 60 and 81.9% for the concentrations of 100, 10 and 1 µg respectively for SE-Au Nps and 69.9, 85.76 and 90% for 100, 10 and 1 µg respectively for crude SE fruit extract (**Figure 7**). The SE-AU Nps was found to be more effective compared to the crude SE fruit extract alone which indicates that Au Nps increases the cytotoxicity and has great potential as conjugate with the fruit extract and can be effectively used as anticancer agent.

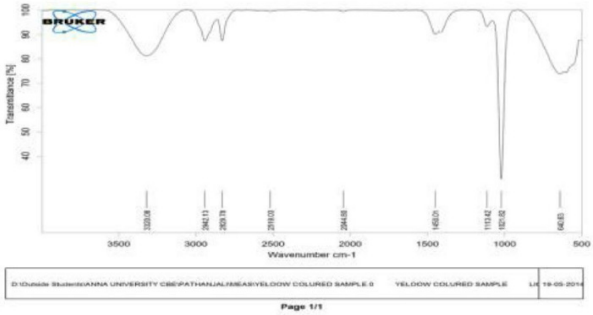

Figure 5. FTIR of SE fruit extract.

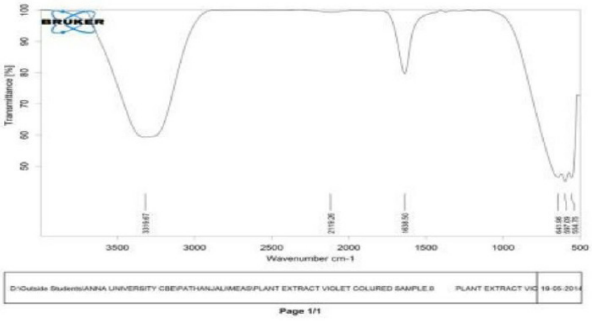

Figure 6. FTIR of SE-Au Nps.

Table 1. MTT assay for cell viability

Concentration	Cell viability (%)	
	Sample A	Sample B
100 µg	47.38003	69.93933
10 µg	60.28682	85.76944
1 µg	81.9636	90.12686
100 ng	98.78654	95.58742
1 ng	97.90403	98.67632

7. Conclusion

The SE fruit extract was prepared using the soxhlet apparatus. The SE fruit extract was used to synthesize the gold nanoparticles. The synthesized gold nanoparticles embedded in the SE fruit extract (SE-Au Nps) were confirmed by its absorbance at 543 nm using the UV Vis spectrophotometer. The size of the Au Nps was found to be widely varying with higher fraction of particles between the size ranges of 15 to 20 nm. This may be due to the agglomeration of the particles. Morphology of the SE-Au Nps was observed using SEM. The FTIR analysis of the SE-Au Nps confirmed the presence of gold nanoparticles in the extract. MTT assay was carried out for both SE fruit extract and SE-Au Nps on MCF7 breast cancer cell line and compared. The results of the MTT assay on MCF7 breast cancer cell line proved that the % cell viability was less for SE-Au Nps than that of the SE fruit extract alone. Thus, the antiproliferative activity of the SE fruit extract was significantly enhanced by embedding it with Au Nps and it can be effectively used in therapeutic applications after further studies. The SE-Au Nps can be further taken to in vivo studies and then to clinical applications.

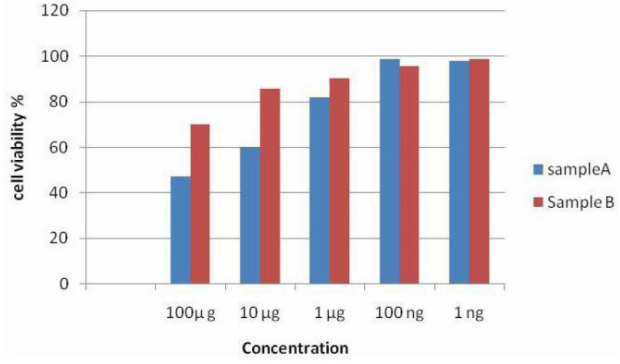

Figure 7. Cell viability determined by MTT assay. Sample A: SE-Au Nps. Sample B: SE fruit extract.

Conflict of interest

No conflict of interest was reported by the authors.

References

1. Manoharan S, Palanimuthu D, Baskaran N, *et al.* Modulating effect of lupeol on the expression pattern of apoptotic markers in 7, 12-dimethylbenz (a) anthracene induced oral carcinogenesis. Asian Pacific Journal of Cancer Prevention 2012; 13(11): 5753–5757.
2. Chow AY. Cell cycle control by oncogenes and tumor suppressors: Driving the transformation of normal cells into cancerous cells. Nature Education 2010; 3(9): 7.
3. Suriamoorthy P, Zhang X, Hao G, *et al.* Folic acid-CdTe quantum dot conjugates and their applications for cancer cell targeting. Cancer Nano 2010; 1: 19–28.
4. Dite GS, Whittemore A, Knight JA, *et al.* Increased cancer risks for relatives of very early-onset breast cancer cases with and without BRCA1 and BRCA2 mutations. British Journal of Cancer 2010; 103: 1103–1108.
5. Parveen S, Sahoo SK. Evaluation of cytotoxicity and mechanism of apoptosis of doxorubicin using folate-decorated chitosan nanoparticles for targeted delivery to retinoblastoma. Cancer Nano 2010; 1(1): 47–62.
6. Holliday DL, Speirs V. Choosing the right cell line for breast cancer research. Breast Cancer Research 2011; 13: 215.
7. Selim ME, Hendi AA. Gold nanoparticles induce apoptosis in MCF-7 human breast cancer cells. Asian Pacific Journal of Cancer Prevention 2012; 13(4): 1617–1620.
8. Florescu A, Amir E, Bouganim N, *et al.* Immune therapy for breast cancer in 2010 — Hype or hope? Current oncology 2011; 18(1): 9–18.
9. Parekh J, Chanda S. In vitro antibacterial activity of the crude methanol extract of Woodfordia fruticose Kurz. Flower (Lythraceae). Brazilian Journal of Microbiology 2007; 38: 204–207.

10. Mahar KS, Rana TS, Ranade SA, *et al.* Genetic variability and population structure in Sapindus emarginatus Vahl from India. Gene 2011; 485(1): 32–9.
11. Chattopadhyay D, Arunachalam G, Mandal SC, *et al.* CNS activity of *Mallotus peltatus* (Geist) Muell Arg. leaf: An ethnomedicine of Onge. Journal of Ethnopharmacology 2003; 85(1): 99–105.
12. Nair R, Kalariya T, Chanda S. Antibacterial activity of some selected Indian medicinal flora. Turkish Journal of Biology 2005; 29: 41–47.
13. Kuznetzova TA, Anisimov MM, Popov AM. A comparative study in vitro of physiological activity of triterpene glycosides of marine invertebrates of echinoderm type. Comparative Biochemistry and Physiology 1982; 73C: 41–43.
14. Rao AV, Sung MK. Saponins as anticarcinogens. Journal of Nutrition 1995; 125: 717S–724S.
15. Konoshima T, Takasaki M, Tokuda H, *et al.* Anti-tumor-promoting activity of majonoside-R2 from Vietnamese ginseng, Panax vietnamensis HA et GRUSHV. (I). Biological and Pharmaceutical Bulletin 1998; 21: 834–838.
16. Marino SD, Iorizzi M, Palagiano E, *et al.* Starfish saponins. 55. Isolation, structure elucidation, and biological activity of steroid oligoglycosides from an Antarctic starfish of the family Asteriidae. Journal of Natural Products 1998; 61: 1319–1327.
17. Mimaki Y, Kuroda M, Kameyama A, *et al.* Steroidal saponins from the underground parts of Ruscus aculeatus and their cytostatic activity on HL-60 cells. Phytochemistry 1998; 48: 485–493.
18. Podolak I, Elas M, Cieszka K. *In vitro* antifungal and cytotoxic activity of triterpene saponosides and quinoid pigments from *Lysimachia vulgaris* L. Phytotherapy Research 1998; 12: S70–S73.
19. Jeyabalan S, Palayan M. Antihyperlipidemic activity of Sapindus emarginatus in Triton WR-1339 induced albino rats. Research Journal of Pharmacy and Technology 2009; 2(2): 319–323.
20. Hebestreit P, Weng A, Bachran C, *et al.* Enhancement of cytotoxicity of lectins by Saponinum album. Toxicon 2006; 47(3): 330–335.
21. Datar RH, Richard JC. Nanomedicine: Concepts, status and the future. Medical Innovation & Business 2010; 2(3): 6–17.
22. Han G, Ghosh P, Rotello VM. Functionalized gold nanoparticle for drug delivery system. Nanomedicine 2007; 2: 113–123.
23. Jain PK, El-Sayed IH, El-Sayed MA. Au nanoparticles target cancer. Nanotoday 2007; 2: 18.
24. Mukherjee P, Pathangey LB, Bradley JB, *et al.* MUC1-specific immune therapy generates a strong anti-tumor response in a MUC1-tolerant colon cancer model. Vaccine 2007; 25(9): 1607–1617.
25. Singh AK, Tripathi YB, Pandey N, *et al.* Enhanced anti-lipopolysaccharide (LPS) induced changes in macrophage functions by Rubia cordifolia (RC) embedded with Au nanoparticles. Free Radical Biology and Medicine 2013; 65: 217–223.
26. Prawat U, Tuntiwachwuttikul P, Taylor WC. Steroidal saponins of *Costus lacerus*. Science Asia 1989; 15: 139–147.
27. Pina EML, Araújo FWC, Souza IA, *et al.* Pharmacological screening and acute toxicity of bark roots of Guettarda platypoda. Revista Brasileira de Farmacognosia 2012; 22(6): 1315–1322.
28. Firdhouse MJ, Lalitha P, Sripathi SK. An undemanding method of synthesis of gold nanoparticles using Pisonia grandis (R.Br.). Digest Journal of Nanomaterials and Biostructures 2014; 9: 385–393.
29. Fang J, Chen X, Liu B, *et al.* Liquid-phase chemoselective hydrogenation of 2-ethylanthraquinone over chromium-modified nanosized amorphous Ni-B catalysts. Journal of Catalysis 2005; 229: 97–104.
30. Parida UK, Bindhani BK, Nayak P. Green synthesis and characterization of old nanoparticles using onion (Allium cepa) extract. World Journal of Nanoscience and Engineering 2011; 1: 93–98.
31. Elia P, Zach R, Hazan S, *et al.* Green synthesis of gold nanoparticles using plant extracts as reducing agents. International Journal of Nanomedicine 2014; 9: 4007–4021.
32. Baker S, Satish S. Biosynthesis of gold nanoparticles by *Pseudomonas veronii* AS41G inhabiting *Annona squamosa* L. Spectrochemica Acta Part A: Molecular and Bimolecular Spectroscopy 2015; 150: 691–695.

Characterization and Application of Nanomaterials (2021) Volume 4 Issue 2
doi:10.24294/can.v4i2.1331

ORIGINAL RESEARCH ARTICLE

Electrospun $Li_3V_2(PO_4)_3$/carbon nanofiber as cathode materials for the high-performance lithium-ion batteries

Mengxi Zhao[1], Zhongpei Lu[1], Lin Chen[2], Xuefan Jiang[3], Fan Yin[1,2], Gang Yang[1,2*]

[1] *School of Chemistry and Material Engineering, Changshu Institute of Technology, Changshu 215500, Jiangsu, China. E-mail: gyang@cslg.cn*

[2] *School of Chemistry and Chemical Engineering, Jiangsu University, Zhenjiang 212013, Jiangsu, China*

[3] *School of Physics and Electronic Engineering, Changshu Institute of Technology, Changshu 215500, Jiangsu, China*

ABSTRACT

In this paper, a series of $Li_3V_2(PO_4)_3$/C composite nanofibers is prepared by a facile and environmentally friendly electrospinning method and calcined under different temperatures. The LVP nanofiber calcined under 900 ºC exhibits the best electrochemical performance. The bicontinuous morphologies of LVP/CNF are the fibers shrunk and the LVP crystals simultaneously grown. At the range of 3.0–4.3 V, LVP/CNF obtained under 900 ºC delivers the initial capacity of 135 mAh/g, close to the theoretical capacity of LVP. Even at high current density, the sample of LVP/CNF still presents good electrochemical performance.

Keywords: Lithium-ion Batteries; Cathode Material; Graphene; Nanocomposite; Electrochemical Performance

ARTICLE INFO

Received: 1 April 2021
Accepted: 20 May 2021
Available online: 28 May 2021

1. Introduction

Lithium battery has the advantages of high specific energy, high battery voltage, wide working temperature range and long storage life. It has been widely used in small electrical appliances, such as portable computers, cameras, electric tools, etc. In recent years, with the increasing shortage of non-renewable resources, such as oil and coal and the urgent needs of environmental protection, energy conservation and emission reduction, countries all over the world such as the United States, Japan Germany and France actively carry out the research on electric vehicle (EV) and hybrid electric vehicle (HEV), and put the development and application of lithium power battery on the important agenda. Because lithium battery has no pollution to the environment, it is more suitable to be used as the power supply of electric vehicle and large power reserve, so it has a very broad application prospect[1].

In recent years, great progress has been made in the research of positive and negative active materials for lithium batteries. At present, the most widely studied positive materials include layered lithium cobalt oxide $LiCoO_2$, spinel oxide $LiMn_2O_4$, phosphate $LiMPO_4$ (M = Mn, Fe, Co, etc.) and $Li_3V_2(PO_4)_3$, but these materials have their own shortcomings, It is difficult to meet the increasing requirements for lithium batteries[2–4]. Therefore, the existing electrode materials and search methods are improved. Finding new high-energy electrode materials

is the top priority of research work, especially new cathode materials, which have become the key factor restricting the further improvement of the overall performance of Lithium batteries.

Monoclinic $Li_3V_2(PO_4)_3$ (LVP), as the cathode material of lithium-ion battery, has gradually attracted extensive attention because of its high theoretical capacity and energy density. The stable frame structure of LVP provides a three-dimensional channel for the insertion/removal of Li^+, and its theoretical capacity is as high as 197 mAh/g in the voltage range of 3.0–4.8 V[5–7]. However, the electronic conductivity of LVP is very poor. It affects the electrochemical performance of LVP and limits its commercial application. Researchers have proposed many methods to overcome the problem of electronic conductivity of LVP. In addition to effective carbon coating and metal ion doping, reducing the particle size or embedding LVP particles into carbon Nanonetworks can also effectively improve the electronic conductivity of LVP[8,9]. As we all know, the migration rate of ions and electrons in LVP plays a key role in improving its electrochemical properties. Therefore, it is a very effective method to improve both ionic conductivity and electronic conductivity, because nanostructured LVP is conducive to the movement and intercalation/de-intercalation of Li^+ in active electrode materials. It can improve the ionic conductivity of LVP. Conductive carbon materials can effectively improve the electronic conductivity of LVP. Nanostructured LVP/C materials can meet the requirements of high electronic and ionic conductivity at the same time. In recent years, LVP nanocomposites with different morphologies, such as spherical particles, nanorods, nanobelts, nanoplates and films, have attracted more and more attention. It is proved that it is beneficial to improve the electrochemical properties of LVP.

The preparation of nanofiber materials by electrospinning technology is a hot spot in the field of material science and technology in the world in recent ten years. Electrospinning has become the main way to effectively prepare nanofiber materials because of its simple manufacturing device, low spinning cost, wide variety of spinnable materials and controllable process. Electrospinning technology is a simple and low-cost method for preparing nanofibers, which has been widely used to prepare materials with one-dimensional nanostructures. With long length and porous structure, nanofibers obtained by electrospinning generally have a large specific surface volume ratio. Many nanofibers are randomly dispersed to form a multi space dense 3D structure. In recent years, the research on the preparation of olivine structure $LiMPO_4$ (M = Mn, Fe, Co, etc.) nanofibers by electrospinning is increasing, and the obtained $LiMPO_4$ fibers show good electrochemical properties[11–13]. However, there are few reports on the preparation of NASICON structure $Li_3V_2(PO_4)_3$. Considering that nanofibers are conducive to improvement. In this paper, $Li_3V_2(PO_4)_3$ with nanofiber structure was prepared by electrospinning, which improved the conductivity and electrochemical properties of $Li_3V_2(PO_4)_3$ as electrode material.

2. Experimental part

Firstly, electrospinning precursor was synthesized, an appropriate amount of citric acid was dissolved in deionized water, NH_4VO_3 and stoichiometric $NH_4H_2PO_3$ and $CH_3COOLi{\cdot}2H_2O$ were added, and the reaction was stirred in oil bath for 4 h to obtain uniform mixed sol A. Polyvinylpyrrolidone (PVP) was added to an appropriate amount of H_2O and stirred for 4 h to obtain transparent viscous liquid B. Drop sol solution A into solution B and stir for 4 h to obtain uniform solution C. The precursor film is prepared by electrospinning method. The obtained white film is raised to 350 °C at a heating rate of 5 °C/min in nitrogen atmosphere and kept at a constant temperature for 4 h to decompose the mixture and release gas. Then it is cooled to room temperature with the furnace. After full grinding, it is burned in a high-temperature tubular furnace. In this process, PVP is carbonized. At the same time, lithium vanadium phosphate (LVP) is generated under high temperature. In order to study the optimal calcination temperature, the effects of heat treatment at four temperatures of 600 °C, 700 °C, 800 °C and 900 °C on the morphology and electrochemical properties of LVP/carbon nanofibers were tried.

The samples were analyzed by X-ray diffraction

(XRD) using D/max-2200/PC X-ray diffractometer of RIGAKU (Science) Company in Japan. The test conditions were Cu target, tube pressure 40 kV. The tube current is 100 Ma, the continuous scanning speed is 4°/min, and the step width is 0.02°. The sample surface morphology is analyzed by JSM-6700F scanning electron microscope produced by JEOL (Japan Electronics) Co., Ltd., the tube voltage is 10 kV and 15 kV, and the tube current is 10 μA.

The electrochemical performance test process of the sample is as follows: weigh the synthesized cathode material, conductive carbon black and polytetrafluoroethylene (PTFE) binder according to the mass percentage of 80:15:5, fully mix, and roll the material into 40 by manual membrane rolling machine μm thin film, cut into a square positive electrode sheet with a side length of 6 mm. The negative electrode adopts high-purity metal lithium sheet with a purity of 99.9%, a thickness of 0.4 mm and a diameter of 10 mm. In order to reduce the impact of humidity on the battery performance, the positive electrode sheet needs to be vacuum dried at 120 °C for 12 h before simulating the battery assembly. The battery assembly is carried out in a glove box filled with high-purity argon. The diaphragm used is Celgard 2500 microporous film, and the battery shell is 2016 button type. Place the positive shell, positive plate, diaphragm, negative plate and negative shell in order from top to bottom, and inject an appropriate amount of electrolyte. The solvent in the electrolyte is a 1:1:1 mixture of vinyl carbonate, diethyl carbonate and dimethyl carbonate, and the solute is $LiPF_6$. The charge discharge performance test of the assembled button battery with a concentration of 1 mol/l was carried out on the land CT2001A battery performance test system produced by Wuhan Lantian Electronics Co., Ltd.

3. Results and discussion

Figure 1 shows the surface morphology of the precursor of LVP/C composite nanofibers after drying in a 60 °C oven. It can be seen from **Figure 1(a)** that the fibers obtained by electrospinning are distributed continuously, and each fiber is interwoven vertically and horizontally to form a dense nanofiber film. However, it can be seen that the diameter distribution of the fibers is uneven. The fiber with larger diameter may be caused by the superposition of several fibers. **Figure 1(b)** shows the specific characteristics of the fiber more intuitively: the diameter is about 500 nm and the fiber surface is smooth.

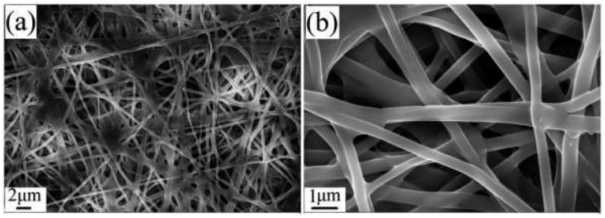

Figure 1. SEM image of the nanofiber precursors obtained from electrospinning.

The LVP nanofiber film obtained by electrospinning was treated at high temperature in a nitrogen atmosphere tubular furnace for 4 h. as shown in Figure 2, the SEM images after heat treatment at different temperatures. It can be seen from the figure that after high temperature treatment, the fibrous morphology of the precursor was not damaged, but different changes occurred on the basis of fiber dimension. However, temperature has a great influence on the morphology of the material. As shown in **Figure 2(a)** and **2(b)**, after calcination at 600 °C for 4 h, the fiber breaks, the diameter is about 600 nm, and small holes are formed on the fiber surface. Combined with XRD data analysis, we know that after calcination at 600 °C, no LVP phase is formed. Therefore, it can be judged that the fiber with rough surface shown in **Figures 2(a)** and **2(b)** is the carbon fiber obtained by PVP carbonization. After increasing the calcination temperature to 700 °C, the fiber surface changes significantly. As shown in **Figures 2(c)** and **2(d)**, the fiber does not break and the diameter becomes smaller at 600 °C, with improved continuity. In addition to similar pores, needle and block particles also appear on the fiber surface. It can be seen from the above analysis that the fiber is the carbide of PVP. Combined with the XRD analysis results, it can be inferred that the needle and block formed on the fiber surface should be the particles of LVP phase. When the temperature continues to rise to 800 °C, as shown in **Figure 2(e)** and **2(f)**, the diameter of the nanofibers obtained at 700 °C is close to that of

the nanofibers, but the needles disappear, the number of massive particles gradually increases, distributed on the surface of the nanofibers, and the particle surface is smooth, which indicates that the LVP phase formed gradually increases with the increase of the calcination temperature. **Figure 2(g)** and **2(h)** are the SEM images after calcination for 4 h when the temperature rises to 900 °C, which can be clearly seen from the figure. The diameter of nanofibers is about 100 nm, and the LVP particles grow gradually. At this time, the PVP transformed carbon fibers still exist continuously and play a supporting role, and the LVP particles are distributed on its surface. It can be seen that the sintering temperature has an effect on the formation of LVP phase, and the heat treatment temperature affects the change of morphology in the treatment of electrospinning precursors.

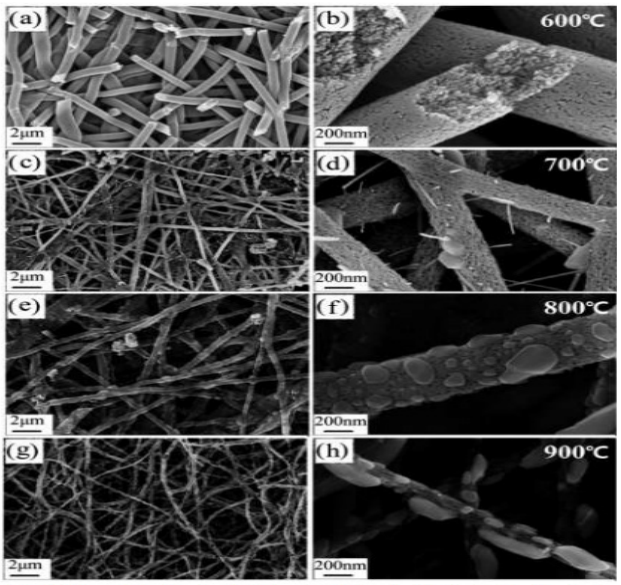

(a)(b):600 ℃;(c)(d):700 ℃;(e)(f):800 ℃;(g)(h):900 ℃

Figure 2. SEM profile of LVP at different calcination temperatures.

After high temperature treatment at different temperatures, the XRD diffraction patterns of each sample are shown in **Figure 3**. It can be seen from the figure that the XRD of the obtained LVP is obviously different. After high temperature treatment at 600 °C at the same heat treatment time, as shown in **Figure 3(a)**, there is no diffraction peak of LVP, showing amorphous characteristics. It shows that it is not enough to react at 600 °C to form LVP phase. When the heat treatment temperature rises to 700 °C, it can be clearly seen from **Figure 3(b)**, the XRD spectrum of the sample shows the characteristic diffraction peak of LVP, but the diffraction peaks of (002) and (111) crystal planes around 15° do not appear, indicating that the temperature still needs to be increased. When the temperature rises to 800 °C, as shown in **Figure 3(c)**. As shown in **Figure 3(d)**, in addition to the enhancement of the diffraction peak intensity, the diffraction peaks of (002) and (111) crystal planes also began to appear. **Figure 3(d)** shows the XRD diffraction peaks of LVP samples obtained after calcination for 4 h after the temperature increased to 900 °C, with monoclinic structure, belonging to P21/n space group, which corresponds to the standard spectral peaks one by one. From the analysis of XRD results, at the same time, Heat treatment temperature plays an important role in the formation of LVP phase.

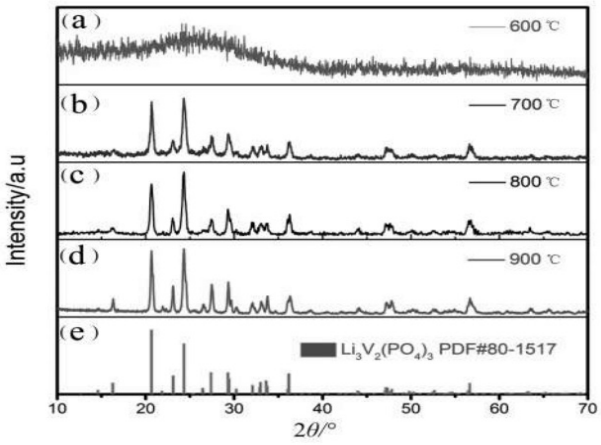

(a)600 ℃,(b)700 ℃,(c)800 ℃,(d)900 ℃

Figure 3. The XRD spectrogram of the LVP at the different calcination temperatures.

After high temperature heat treatment at 700 °C, 800 °C, 900 °C, the obtained LVP nanofibers were ground and prepared into electrode sheets, and then assembled into batteries. The electrochemical properties were tested respectively in the voltage range of 3.0–4.3 V and 3.0–4.8 V. **Figure 4** shows the constant magnification (0.1 C, 1 C = 133 MAH/g) of LVP samples in the voltage range of 3.0–4.3 V. It can be seen from the charging curve that there are three platforms at 3.59, 3.68 and 4.09 V, but these three platforms are not obvious for the LVP samples calcined at 700 °C and 800 °C, which is consistent with the XRD data because the crystallinity of LVP

phase in the samples is not high. With the increase of temperature, the crystallinity of LVP phase gradually increases. The characteristic platform of LVP in the charge discharge curve is also gradually obvious. The cycle performance of each sample after 50 charge discharge cycles at a constant magnification of 0.1 C is shown in **Figure 4(b)**. It can be seen from the figure that with the increase of calcination temperature, the discharge specific capacity of LVP samples gradually increases, and the cycle stability also improves. After 50 cycles, specific discharge capacity of LVP at 900 °C, 800 °C, 700 °C retains 132 mAh/g, 119 mAh/g, and 92 mAh/g respectively, which are 90%, 91% and 76% of the initial discharge specific capacity respectively. According to the charge discharge test results at small magnification (0.1 C), the LVP samples treated at 700 °C have shown poor capacity and cycle stability. In order to further study the effect of 800 °C and 900 °C on the performance of LVP, the variable rate charge and discharge performance at high voltage was tested.

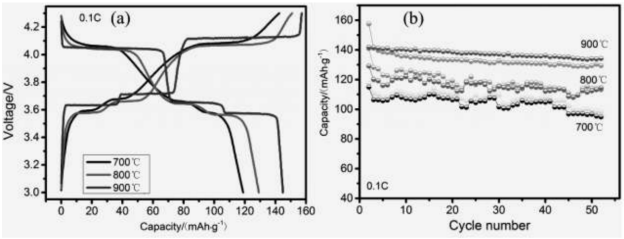

Figure 4. First circle charge and discharge curve and cycle performance diagram of the LVP in the 3.0–4.3 V voltage range obtained at different calcination temperatures, and the charge and discharge ratio is 0.1 C.

Figure 5 is the first charge discharge curve and cycle performance diagram of each electrode material under the charge discharge ratio of 0.1 C and 50 cycles in the voltage range of 3.0–4.8 V. When the battery is charged to 4.8 V, three Li^+ are completely separated from the LVP, with two-phase electrochemical platforms of 3.59, 3.68, 4.09 and 4.56 V respectively. The platforms of LVP charge curve obtained by calcination at 700 °C are not obvious, and in the discharge curve, the platforms of the three samples at about 4.0 V are inclined because of the irreversibility of the reaction. Two platforms can be seen in the discharge process, and the three discharge platforms are LVP electrodes. According to the cycle performance diagram in **Figure 5(b)**, the capacity of each sample decreases because the electrode material may dissolve in the electrolyte under high voltage, resulting in the instability of the LVP frame structure. After 50 cycles, the discharge specific capacities of the three samples are 114.2 mAh/g, 134.7 mAh/g, 151.6 mAh/g respectively, 74%, 73% and 77% of the specific discharge capacity of the first cycle are retained.

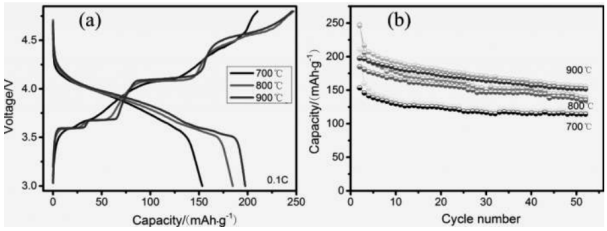

Figure 5. First cycle charge discharge curve and cycle performance diagram of LVP obtained at different calcination temperatures in the voltage range of 3.0–4.8 V. The charge discharge ratio is 0.1 C.

Similarly, we studied the variable rate performance of LVP samples calcined at 800 and 900 °C. As shown in **Figure 6**, the two samples were charged at constant current rate of 0.1 C and discharged at different discharge rates of 0.1 C, 1 C, 2 C, 5 C, 10 C and 20 C. It can be seen that with the increase of discharge ratio, the platform of charge discharge curve decreases gradually, and the first discharge specific capacity at each ratio decreases. LVP electrode calcined at 900 °C. Under the variable rate performance test, although the coulomb efficiency is less than 800 °C, the material shows good electrochemical performance. Even at higher rates, such as 10 C and 20 C, its specific discharge capacity can still maintain 88 mAh/g and 50 mAh/g. LVP nanoparticles are attached to carbon nanofibers with excellent conductivity. The composite structure effectively improves the electrochemical properties of LVP particles.

4. Conclusion

LVP nanofibers were prepared by a simple and feasible electrospinning method. LVP nanofibers with different morphologies were obtained after treatment at different calcination temperatures for

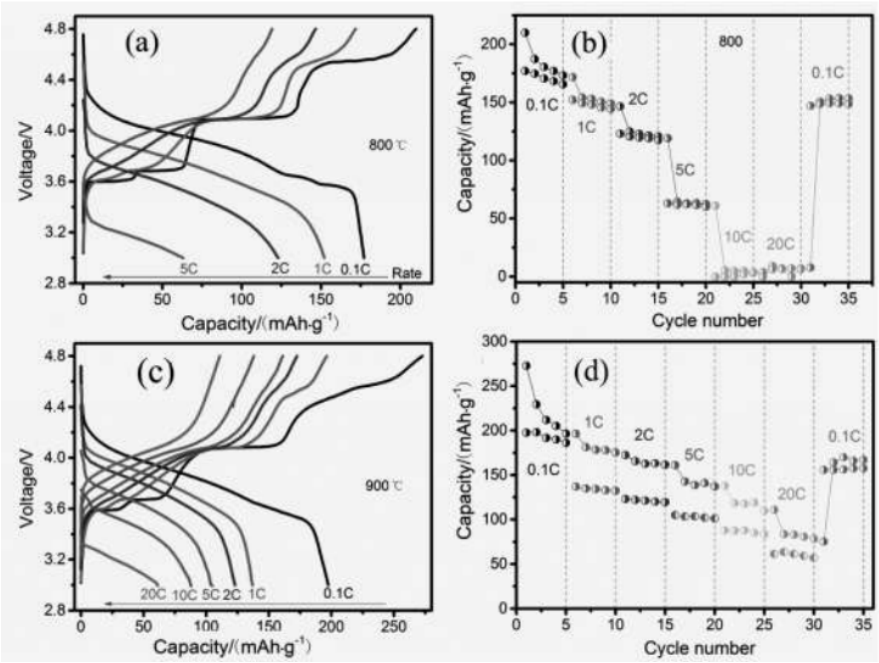

Figure 6. Magnification performance diagram of LVP/CNF obtained at 800 °C and 900 °C.

4 h. LVP particles can be embedded on the surface of nanofibers at higher temperatures. The sintering temperature plays an important role in the phase formation of LVP. The higher the temperature, the more LVP phase is formed, Through the test of electrochemical properties, the LVP calcined at 900 °C has good cycle performance and rate performance. Therefore, the LVP phase with high electrochemical activity is the most at this temperature. LVP nanoparticles are embedded on polymer fibers, and the particles are connected through fibers. Through comparison, the optimal sintering temperature is 900 °C. The first discharge capacities of LVP samples calcined at 800 °C and 900 °C are 134 mAh/g and 135 mAh/g in the voltage range of 3.0–4.3 V, reaching the theoretical capacity of $Li_3V_2(PO_4)_3$, which is 133 mAh/g. At high magnification, the LVP/C fiber composite sample still has excellent electrochemical properties.

Conflict of interest

The authors declare that they have no conflict of interest.

Acknowledgements

This work was supported by the Jiangsu Natural Science Foundation "Synthesis and Electrochemical Properties of Cathode Material Lithium Nickel Manganite of High Performance Lithium Batteries" (BK20141229).

References

1. Huang K, Wang Z, Liu S. Principle and key technology of lithium batteries (in Chinese). Beijing: Chemical Industry Press; 2007. p. 12.
2. Yang G, Liu H, Ji H, *et al.* Temperature-controlled microwave solid-state synthesis of $Li_3V_2(PO_4)_3$ as at cathode materials for lithium batteries. Journal of Power Sources 2010; 195: 5374–5378.
3. Zhang X, Wang K, Wei X, *et al.* Carbon-coated V_2O_5 Nanocrystals as high performance cathode materials for lithium ion batteries. Chemistry of Materials 2011; 23: 5290–5292.
4. Son J, Kim G, Kim M, *et al.* Carbon coated NASICON type $Li_3V_{2-x}M_x(PO_4)_3$ (M=Mn, Fe and Al) materials with enhanced cyclability for Li-ion batteries. Journal of the Electrochemical Society 2013; 160: A87–A92.
5. Sun C, Rajasekhara S, Dong Y, *et al.* Hydrothermal synthesis and electrochemical properties of $Li_3V_2(PO_4)_3$/C-based composites for Lithium batteries. ACS Applied Materials & Interfaces 2011; 3: 3772–3776.

6. Kuang Q, Zhao Y, Liang Z. Synthesis and electrochemical properties of Na-doped $Li_3V_2(PO_4)_3$ cathode materials for Li-ion batteries. Journal of Power Sources 2011; 196: 10169–10175.
7. Chen L, Yan B, Xu J, *et al.* Bicontinuous structure of $Li_3V_2(PO_4)_3$ clustered via carbon nanofiber as high-performance cathode material of Li-ion batteries. ACS Applied Materials & Interfaces 2015; 7: 13934–13943.
8. Liu H, Yang D, Zhang X, *et al.* Kinetics of conventional carbon coated-$Li_3V_2(PO_4)_3$ and nanocomposite $Li_3V_2(PO_4)_3$/graphene as cathode materials for power lithium ion batteries. Journal of Materials Chemistry 2012; 22: 11039–11048.
9. Wang H, Li Y, Huang C, *et al.* High-rate capability of $Li_3V_2(PO_4)_3$/C composites prepared via a polyvinylpyrrolidone-assisted sol-gel method. Journal of Power Sources 2012; 208: 282–287.
10. Yang Y, Wang H, Zhou Q, *et al.* Improved lithium storage properties of electrospun TiO_2 with tunable morphology: from porous anatase to necklace rutile. Nanoscale 2013; 5: 10267–10274.
11. Hagen RV, Lorrmann H, Moller KC, *et al.* Electrospun $LiFe_{1-y}Mn_yPO_4$/C Nanofiber Composites as Self-Supporting Cathodes in Li-ion batteries. Advanced Energy Materials 2012; 2: 553–559.
12. Damen L, Giorgio F D, Monaco S, *et al.* Synthesis and characterization of carbon-coated $LiMnPO_4$ and $LiMn_{1-x}Fe_xPO_4$ (x=0.2, 0.3) materials for lithium-ion batteries. Journal of Power Sources 2012; 218: 250–253.

Characterization and Application of Nanomaterials (2021) Volume 4 Issue 2
doi:10.24294/can.v4i2.1332

ORIGINAL RESEARCH ARTICLE

Synthesis and application of nano-MH/MPB as intumescent flame retardant (IFR)

Aiming Zhao, Yanmao Dong, Qiuyang Ni, Zhiyu Bao*

School of chemistry and Bioengineering, Suzhou University of Science and Technology, Suzhou 215009, Jiangsu, China.
E-mail: bzy1952@126.com

ABSTRACT

Magnesium hydroxide/melamine phosphate borate (nano MH/MPB), a novel nano-composition intumescent flame retardant, was synthesized with the in-situ reaction method from $MgCl_2 \cdot 6H_2O$ sodium hydroxide (NaOH) and melamine phosphate borate (MPB) in the absence of H_2O. The structure of the product was confirmed by EDAX IR and XRD. The effects of reaction temperature and time on the dimension of magnesium hydroxide were observed. The effects of mass ratio of magnesium hydroxide to MPB on the flame retardancy of nano-MH/MPB/EP were examined with the limiting oxygen test. The results show that the optimal condition of synthesis of MH/MPB is mMH/mMPB = 0.25, reacting under 75 °C for 30 minutes. Finally, the mechanism for flame retardancy of nano-MH/MPB/EP was pilot studied by means of IR of char layer and TG of MH/MPB.

Keywords: Intumescent Flame Retardant; Magnesium Hydroxide; Nano-Composition; Melamine Phosphate Borate; Synergistic Agents

ARTICLE INFO

Received: 23 April 2021
Accepted: 16 June 2021
Available online: 23 June 2021

1. Introduction

In recent years, intumescent flame-retarded (IFR) has become a research hotspot because of its high thermal stability and environmental friendliness[1]. IFR is mainly composed of carbon source (such as pentaerythritol), acid source (such as ammonium polyphosphate) and gas source (such as melamine), which can be divided into mixed type and simple type. Among them, hybrid IFR has some disadvantages, such as easy moisture absorption, poor thermal stability, low flame-retarded efficiency and difficult compatibility with polymers[2]. Simple IFR can effectively solve the above problems, but it also has the disadvantages of single element composition and high cost.

In order to improve the above problems, IFR and nanoparticles can be used as flame-retarded polymers. Nanoparticles have the characteristics of high surface atomic ratio, large specific surface area and good dispersion, showing a unique volume effect and surface effect[3], which can improve the mechanical properties and flame-retarded properties of materials. It is reported that clay[4,5], nano magnesium hydroxide (MH)[6], nano aluminum hydroxide[7], nano SiO_2[8], nano zinc oxide (ZnO)[9,10], nano TiO_2 can be used as synergistic agents of IFR to flame-retarded PP, PE, PA66, etc.[11] However, the current research mainly focuses on Intumescent clay nanocomposite flame-retarded PP and PA66[12].

Magnesium hydroxide (MH) decomposes at 340–490 °C, and the initial decomposition temperature is 100 °C higher than that of $Al(OH)_3$; the heat absorption capacity of 1.37kj·g^{-1} is higher than that of $Al(OH)_3$ (1.17kj·g^{-1}), and the heat capacity is also 17%, which is helpful to improve the flame-retarded efficiency[13,14]; in addition, magnesium hydroxide is a good smoke suppressant[15]. Nano MH was introduced into IFR system to flame-retarded EP for the first time to improve the disadvantages of IFR, such as low flame-retarded efficiency and incompatibility with materials. Nano MH/MPB intumescent nanocomposite flame-retarded was prepared by in-situ generation method. The flame-retarded synergistic effect of MH and MPB in EP was studied.

2. Experiment

2.1 Main raw materials

Melamine phosphate borate (MPB), self-made (as shown in **Figure 1**)[16]; $MgCl_2·6H_2O$, analytical reagent, produced by Shanghai Tongya Chemical Technology Development Co., Ltd; ethylenediamine, analytical pure, produced by Shanghai Qiangshun Chemical Co., Ltd; E-44 epoxy resin (EP), produced by Zhenjiang Danbao Resin Co., Ltd.

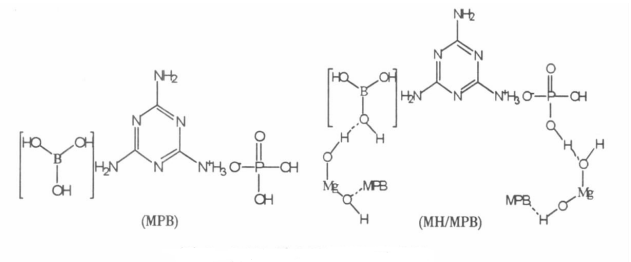

Figure 1. Sketch pattern of MPB and MH/MPB.

2.2 Synthesis of MH/MPB

MPB, $MgCl_2·6H_2O$ and water are added into a three-mouth bottle in a certain proportion, heated and stirred, and completely dissolved by ultrasonic oscillation. Then, slowly drop the prepared precipitant NaOH solution into the aqueous solution of MPB and $MgCl_2·6H_2O$, gradually appear white turbidity, ultrasonic oscillation, stirring and holding for a period of time. Cool, filter, wash with water and absolute ethanol until there is no CL ($AgNO_3$ detection), dry at 60 °C and weigh.

2.3 Preparation of flame-retarded epoxy resin samples of MH/MPB

Ethylenediamine was used as curing agent, 10 g epoxy resin and 1 g ethylenediamine were mixed at room temperature, stirred evenly, and a certain amount of MH/MPB flame-retarded was added. After stirring evenly, it is injected into a self-made aluminum mold with specific size, cured at room temperature for 24 hours, and then cured at 80 °C for 2 hours. After complete curing, it shall be trimmed into the required spline for testing.

2.4 Testing and characterization

1) The products were detected by Prostar LC240 infrared spectrometer (KBr tablet pressing method).

2) The X-ray powder diffraction test is continuously scanned on the German Bruker D8 X-ray diffractometer for XRD test. The test conditions are: Cu target, rear monochrome tube, 45 kV of tube pressure, 20 mA of tube flow, scanning ranging $10° \leq 2\theta \leq 80°$, 4°·min^{-1} of scanning speed.

3) The elemental composition of the product was detected by S-570 scanning electron microscope (SEM) (equipped with edaxpv9900 energy spectrometer).

4) The oxygen index test (LOI) adopts HC900-2 oxygen index tester according to GB/T 2406-93, and the flame-retarded epoxy resin spline size is 110 mm × 6 mm × 3.5 mm; limiting oxygen index test is conducted.

5) American Pekin Elmer TGA7 thermogravimetric analyzer is used for thermogravimetric analysis.

3. Results and discussion

3.1 Theory

MPB molecules contain -NH_2, -OH, P=O and other groups. These groups can form hydrogen bonds with -OH of nano MH (as shown in **Figure 1**). At the same time, nanoparticles have high activity and are easy to combine with macromolecules. In this way, nano MH/MPB intumescent nanocomposite

flame-retarded was prepared by combining MH and MPB through chemical and physical effects.

3.2 Infrared spectrum analysis

The infrared spectra of MH, MPB and MH/MPB are shown in **Figure 2**. Infrared spectrum analysis is as follows[17]: in **Figure 2a**, 3,698 cm^{-1} is O-H stretching absorption peak in the MH crystal structure, 1,467 cm^{-1} is the bending vibration absorption peak of -OH, and the wide absorption peak near 1,643 cm^{-1} and 3,413 cm^{-1} should be the absorption peak of H_2O in MH crystal. This result is consistent with the MH results reported in literature[18]. **Figure 2c** is obviously different from **Figures 2a** and **2b**. In **Figure 2c**, there are not only the O-H stretching absorption peak 3,702 cm^{-1} in MH structure, but also the overlapping 3,339 cm^{-1} and 3,132 cm^{-1} of N-H stretching vibration absorption peaks in $-NH^{3+}$, -OH and $-NH_2$ in MPB structure, P=O stretching vibration absorption peak 1,265 cm^{-1}, C=N stretching vibration absorption peak 1,656 cm^{-1}. This shows that MH/MPB composite flame-retarded was prepared.

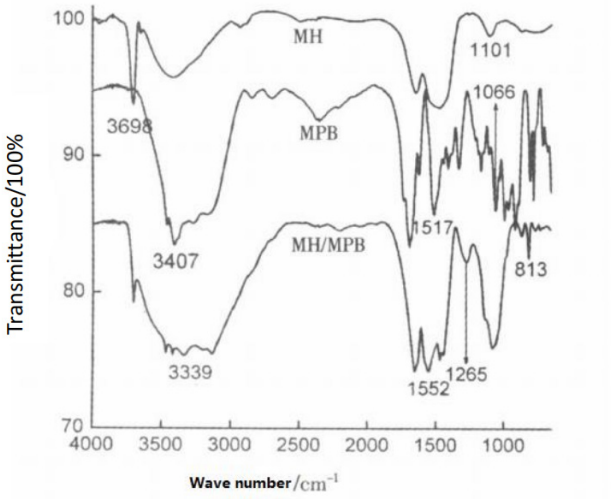

Figure 2. Infrared spectrum of MH/MPB and MH/MPB.

3.3 Elemental analysis

The energy spectrum of MHMPB (mMH/mMPB = 0.25) is shown in **Figure 3**. It can be seen from **Figure 3** that the product mainly contains C, N, O, P, Mg and other elements, which further confirms the preparation of MH/MPB composite flame-retarded.

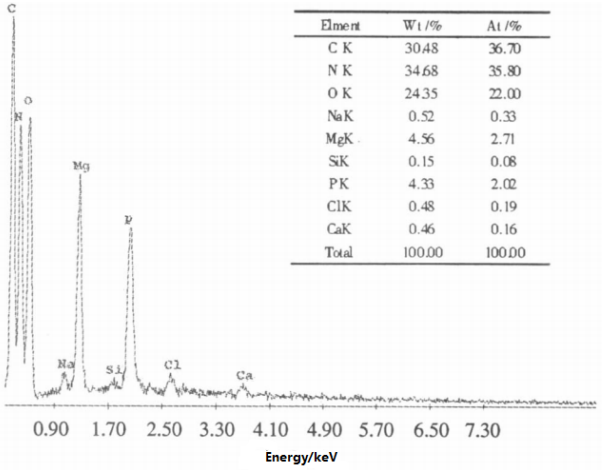

Elment	Wt /%	At /%
C K	30.48	36.70
N K	34.68	35.80
O K	24.35	22.00
NaK	0.52	0.33
MgK	4.56	2.71
SiK	0.15	0.08
PK	4.33	2.02
ClK	0.48	0.19
CaK	0.46	0.16
Total	100.00	100.00

Figure 3. Energy spectrum of MH/MPB (mMH/mMPB).

3.4 XRD analysis of MH, MPB and MH/MPB

The XRD spectra of MH, MPB and MH/MPB are shown in **Figure 4**. It can be seen from the comparison of the diffraction peak positions of **Figure 4C** with **Figure 4A** and **Figure 4B** that in **Figure 4C**, MPB and $Mg(OH)_2$ diffraction peaks exist. Thus, the preparation of MH/MPB complex was further confirmed. The diffraction peak position of crystal plane of MH's (001), (100), (101) in **Figure 4C** is obvious and widened, indicating that the particle size is small[19]. The grain size can be determined by XRD using Scherrer formula. The peak is calculated to obtain, and the calculation results are shown in **Table 1**[20]. The calculated results show that $Mg(OH)_2$ in the prepared MH/MPB composite has reached nano level.

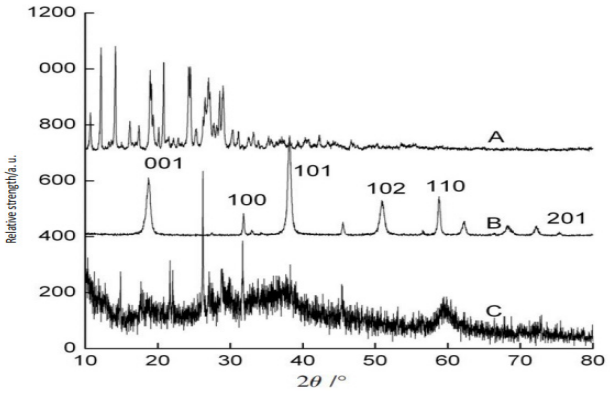

Figure 4. XRD spectra of MH, MPB and MH/MPB (**A**: MPB; **B**: MH; **C**: MH/MPB).

Table 1. Grain size of MH/MPB

2θ/°	Crystal plane/hkl	Half peak width/°	Grain size/nm
17.72	001	0.33	24.12
31.70	100	0.19	43.03
38.24	101	0.15	55.51
59.34	110	0.40	20.12

3.5 Effect of reaction temperature on grain size of MH/MPB

Using single factor experimental analysis, keep other influencing factors unchanged, change the reaction temperature to 35 °C, 45 °C, 55 °C, 65 °C and 75 °C, and compare the effect of MH/MPB XRD spectrum (**Figure 5**), and the grain size is calculated and compared by Scherrer formula (**Table 2**).

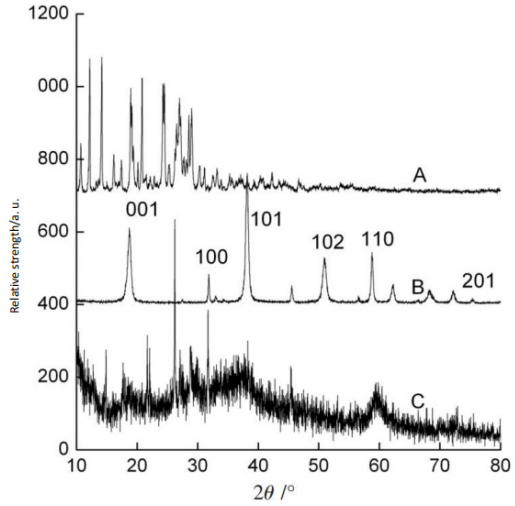

Figure 5. XRD patterns of MH/MPB at different reaction temperatures (**A**: 35 °C; **B**: 45 °C; **C**: 55 °C; **D**: 65 °C; **E**: 75 °C).

Figure 5 shows that when the temperature is too high, the diffraction peak is obviously refined, indicating that the grain size becomes larger, and the change of (201) crystal plane is obvious. In addition, it can be concluded from **Table 2** that when the stress temperature is lower than 75 °C, the grain size of MH/MPB decreases slightly with the increase of temperature; when the reaction temperature reaches 75 °C, the grain size of MH/MPB increases sharply. This is because the reaction temperature has an effect on the formation and growth of nuclei[21]. The nucleation rate in low temperature region is higher than that in crystal. The growth rate is fast, that is, low temperature is conducive to the formation of crystal nucleus, which is not conducive to the growth of crystal nucleus. Generally, fine crystals are obtained; as the temperature increases, the solubility decreases. The viscosity of the liquid increases the mass transfer coefficient and greatly improves the crystal growth rate, so as to increase the crystal nucleus. When the temperature exceeds 75 °C, the crystal nuclei agglomerate and the grain size increases sharply.

3.6 Effect of reaction time on grain size of MH/MPB

Keep other influencing factors unchanged, change the reaction time to 10, 20, 30, 40 and 50 minutes, and compare the XRD spectra of MH/MPB (**Figure 6**). The grain size is calculated and compared by Scherrer formula (**Table 3**). As shown in **Figure 6**, when the reaction time is less than 30 min, the diffraction peak broadening is obvious, indicating that the grain size is small; more than 30 minutes, the diffraction peak is obviously refined, indicating

Table 2. Grain size of MH/MPB at different reaction temperatures

Temperature /°C	Crystal plane / hkl	2θ/°	Half peak width /°	Grain size / nm	Average size /nm	Temperature /°C	Crystal plane / hkl	2θ/°	Half peak width /°	Grain size /nm	Average size /nm
	001	17.86	0.40	19.91			001	17.76	0.50	15.92	
35	100	31.76	0.25	32.71	26.50	65	100	31.74	0.37	22.10	21.93
	101	38.48	0.31	26.88			101	38.34	0.30	22.76	
	001	17.86	0.26	30.61			001	17.94	0.13	61.23	
45	100	31.72	0.41	19.94	27.53	75	100	31.74	0.20	40.89	51.39
	101	38.46	0.26	32.04			101	38.32	0.16	52.05	
	001	18	0.28	28.44							
55	100	31.84	0.40	20.45	23.80						
	101	38.46	0.37	22.52							

that the grain size becomes larger; (101) and (110) crystal planes change significantly. This moment the image is confirmed by **Table 3**. When the reaction time is 30 minutes, the grain size of MH/MPB is the smallest, close to 19 nm. The reaction speed between magnesium chloride and sodium hydroxide is very fast, and the whole reaction can be completed in an instant. At the initial stage of the reaction, fine MH is easy to agglomerate and form larger MH; but with the extension of time, the energy and activity of MH crystal increase, and the smaller MH can be removed from the larger MH crystal separated to form MH particles with small particle size[22]. If the reaction time is too long, MH particles will agglomerate again. So it's not easy to react too short or too long and the optimum reaction time is 30 minutes.

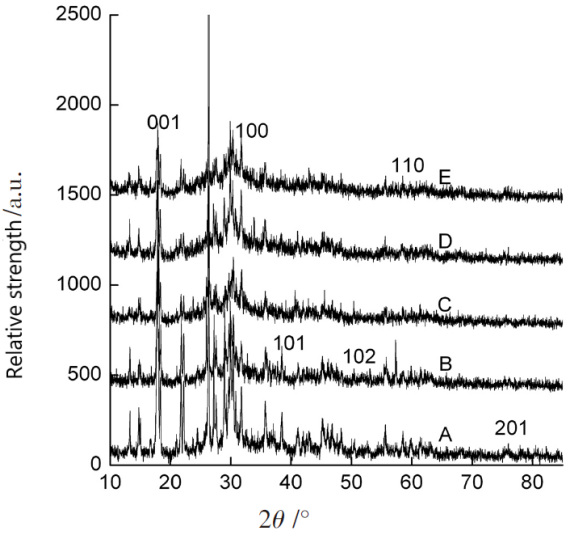

Figure 6. XRD pattern of MH / MPB at different reaction times.

Table 3. Grain size of MH/MPB at different reaction temperatures

Temperature /°C	Crystal plane / hkl	2θ/°	Half peak width /°	Grain size /nm	Average size /nm	Temperature /°C	Crystal plane / hkl	2θ/°	Half peak width /°	Grain size /nm	Average size /nm
	001	17.74	0.14	58.86			001	17.82	0.16	49.76	
10	101	37.66	0.24	34.63	37.86	40	101	37.92	0.14	59.41	48.94
	110	59.32	0.45	20.11			110	58.96	0.24	37.65	
	001	17.72	0.33	24.12			001	17.7	0.13	61.24	
20	101	38.24	0.15	55.50	34.08	50	101	39.12	0.08	104.35	90.48
	110	59.34	0.4	22.63			110	59.3	0.06	105.85	
	001	17.7	0.3	26.5							
30	101	38.26	0.47	17.71	19.05						
	110	59.46	0.7	12.94							

Table 4. Effect of MMH/MMPB on LOI of epoxy resin

Order	1	2	3	4	5	6	7	8	9
Fire retardant		MPB	MH/MPB (0.05:1)*	MH/MPB (0.15:1)*	MH/MPB (0.25:1)*	MH/MPB (0.35:1)*	MH/MPB (0.5:1)*	MH/MPB (0.5:1)*	MH/MPB (0.75:1)*
LOI/%	18	25	27	27	28	26	25	24 (self-extinguish)	24

Note: (*) is mMH/mMPB.

3.7 Effect of mMH/mMPB on LOI of MH/MPB flame-retarded epoxy resin

Table 4 is the limiting oxygen index of MH/MPB with different mMH/mMPB ratio when adding 20% (mass fraction) to epoxy resin. It can be seen from **Table 4** that MH and MPB have good flame-retarded synergistic effect. When mMH/mMPB is 0.05, the LOI of EP increases from 25% to 27%, and when mMH/mMPB is 0.25, the LOI of EP reaches the highest point of 28%. With the increase of mMH/mMPB, the amount of MgO produced by hydrolysis is more, which leads to the increase of flame-retarded effect of flame-retarded composites in the combustion process of the flame-retarded composite increased. However, when the mMH/mMPB value exceeds 0.25, the LOI of EP decreased significantly, even lower than that of MPB/EP. The reason may be that there is too much MH, which leads to the rela-

tive reduction of MPB and the impact on its flame retardancy. Therefore, 0.25 mMH/mMPB is the best ratio.

3.8 MH/MPB thermogravimetric analysis

According to the TG analysis of MH/MPB (**Figure 7**), MH/MPB is mainly decomposed at 200–300 °C; after 300 °C, MH/MPB is decomposed very little; at 700 °C, there is still a high carbon residue rate, up to 39%, which shows that MH/MPB has better flame retardancy. The DTG diagram (**Figure 8**) shows that, MH/MPB has three main thermogravimetric rate peaks 106.2 °C, 261.3 °C and 303.7 °C. Small molecular water contained in MH/MPB shall be at 106.2 °C, 261.3 °C and 303.7 °C are the thermal weight loss rate peaks of MH/MPB. The main peaks of DTA (**Figure 9**) are 266.9 °C and 317 °C, which is basically consistent with the DTG peak.

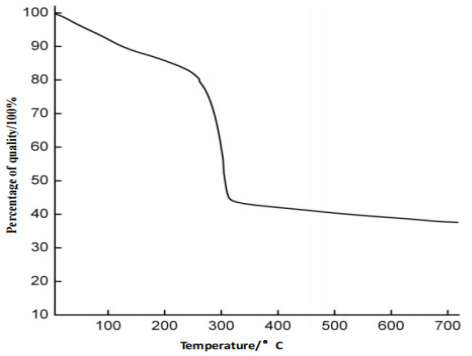

Figure 7. TG pattern of MH/MPB.

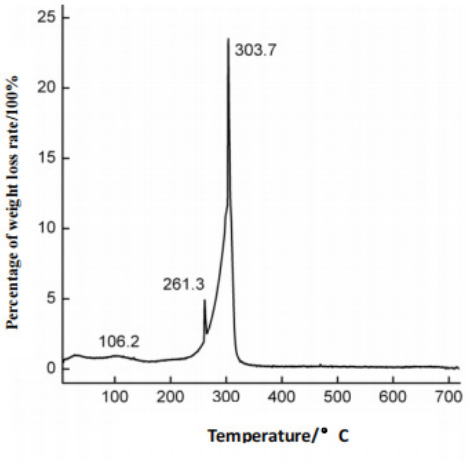

Figure 8. DTG pattern of MH/MPB.

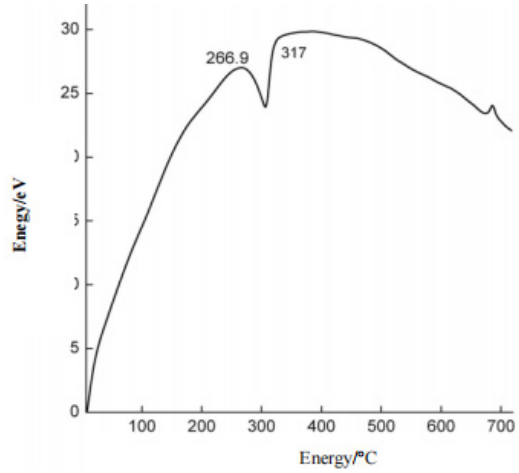

Figure 9. DTA pattern of MH/MPB.

Table 5. Effect of addition amount of MH/MPB (0.25:1)* on LOI

Order	1	2	3	4	5
Addition amount /%	0	10	20	30	40
LOI /%	18	25	28	29 (self-extinguish)	30

Note: (*) is mMH/mMPB = 0.25:1.

3.9 Preliminary study on the mechanism of MH/MPB flame-retarded epoxy resin

It can be seen from **Table 5** that the LOI of MH/MPB/EP is significantly higher than that of EP without MH/MPB (0.25:1)* (LOI is 18%), and the LOI of EP gradually increases with the increase of MH/MPB addition. When the addition amount reaches 40%, the LOI of epoxy resin reaches 31%. When the addition of MPB was 20%, the LOI of epoxy resin increased significantly, and then tended to be flat. It can be seen that the best addition amount of MH/MPB is 20%, LOI reached 28%. XRD analysis of carbon residue (**Figure10**) shows that the addition of MH makes the peak of carbon residue tend to be flat, and the carbon residue tends to amorphous carbon. So MH changed the morphology of carbon residue.

The carbon slag produced by EP, EP/MPB and EP/MH/MPB in the oxygen index test experiment shall be tested by infrared to understand the carbon layer structure, as shown in **Figure 11**. By analyzing **Figure 11**, the infrared spectrum of carbon residue of EP/MH/MPB is obviously different from the other two, and the position of absorption peak changes.

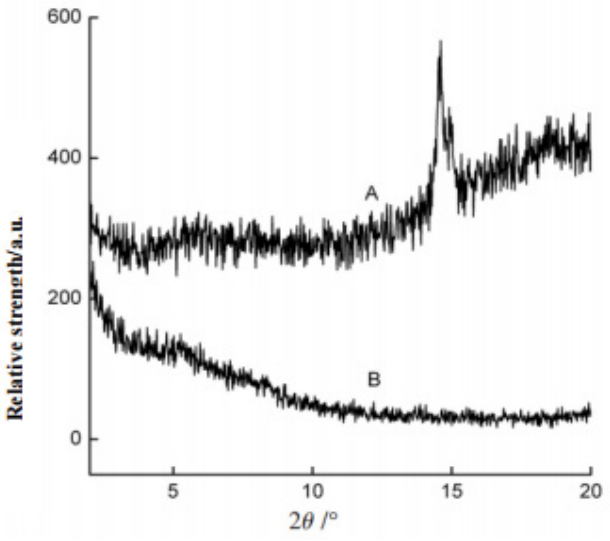

Figure 10. XRD pattern of carbon slag.

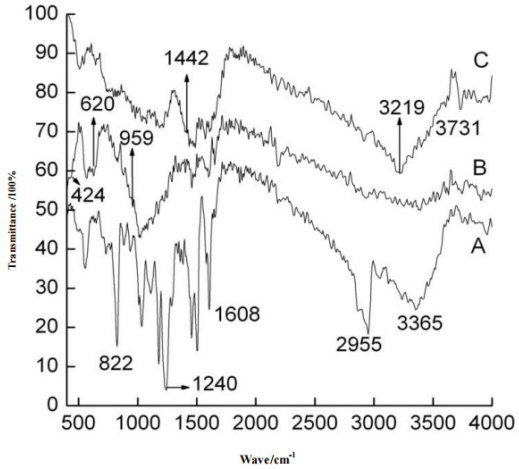

Figure 11. Infrared spectra of EP, EP/MPB and EP/MH/MPB carbon residues (**A**: EP; **B**: EP/MH/MPB; **C**: EP/MPB).

In **Figure 11B**, the peak at 424 cm^{-1} is the stretching vibration absorption peak of Mg-O bond, 1,317 cm^{-1} is the stretching vibration absorption peak of B-O, 959 cm^{-1} is the stretching vibration absorption peak of P-O-P, 1,652 cm^{-1} is the stretching vibration peak of C=C double bond, and 620 cm^{-1} is the characteristic peak of aromatic ring[17,23]. This shows that the combustion carbon residue contains Mg-O bond, B-O bond, P-O-P bond and C=C double bond. In **Figure 11C**, the bi-peaks at 2,955 cm^{-1} as C=O characteristic peaks disappeared in **Figure 6B**. It is seen that the addition of MH affects the structure and composition of EP combustion carbon slag and the EP combustion thermal decomposition process. During thermal degradation or combustion processes, MH/MPB produces phosphate-polyphosphate-polydephosphate, and forms a nonvolatile phosphate layer (P-O-P bond) protective layer. Polydephosphate has dehydration, so it can form the carbonized layer[24]; MH/MPB produces boric anhydride or boric acid during combustion. Boric acid can form a glass-like melt (B-O bond) during thermal cracking, which is covered on the material; the combustion carbon residue contains Mg-O bond, B-O bond, P-O-P bond and C=C double bond. In **Figure 11C**, the double peak at 2,955 cm^{-1} is C=O, and the characteristic peak disappeared in **Figure 6B**. It can be seen that the addition of MH affects the structure and composition of EP combustion carbon slag and the thermal decomposition process of EP combustion. During thermal degradation or combustion or the burning process, MH/MPB produces phosphoric acid–metaphosphoric acid–polymetaphosphoric acid to form a non-volatile phosphoric acid layer (P-O-P bond) protective layer. Polymetaphosphoric acid has dehydration and it can form a carbonization layer[24]; during the combustion of MH/MPB, boric anhydride or boric acid is produced. Boric acid can form a glass like molten metal during thermal cracking. The melt (B-O bond) is covered on the material; the high temperature decomposition of MH in MH/MPB produces MgO, which can interact with the pyrolysis products of EP and MPB. It can be transformed into a more stable carbon layer containing Mg, P, B, C and other elements, promote the direct oxidation of the material into carbon dioxide and reduce the combustible gas carbon monoxide. The generation of stable carbon layer can isolate the air and prevent the outward diffusion of combustible gas, so as to achieve the purpose of flame-retarded. In addition, MH/MPB contains nitrogen, which can release refractory gas NH_3 when heated, diluting the concentration of oxygen in the air. High temperature MH contained in MH/MPB decomposition endothermic has cooling effect and flame-retarded effect. It can be seen that the flame-retarded EP of MH/MPB has flame-retarded mechanisms such as condensed phase, gas phase and synergy. It can't be explained by one mechanism. It contains nitrogen, which can release refractory gas NH_3 when heated, diluting the concentration of oxygen in the air.

4. Conclusion

(1) MH/MPB nanocomposite flame-retarded was prepared by in-situ formation method. Through single factor experimental analysis, it is concluded that the grain size of MH/MPB synthesized is small when the reaction temperature is lower than 75 °C and the reaction time is 30 min. It can be seen that MH reaches nano level through Scherrer formula. (2) When mMH/mMPB is 0.25, MH and MPB have the best synergistic effect and the best flame-retarded performance; when the addition amount of epoxy resin (EP) is 20%, the limiting oxygen index (LOI) of epoxy resin reaches 28%. (3) The thermogravimetric analysis of MH/MPB shows that MH/MPB has a high decomposition temperature, and the remaining carbon rate is still 39% at 700 °C. (4) XRD and IR analysis of carbon slag show that the carbon slag contains Mg-O bond, B-O bond, P-O-P bond, C=C double bond and so on. The addition of MH not only plays an endothermic and cooling role, but also makes MH/MPB flame-retarded EP produce stable carbon layer with element structure of Mg, P, B, C and other elements in the combustion process, so as to achieve flame-retarded and heat insulation effect.

Conflict of interest

The authors declare that they have no conflict of interest.

References

1. Chen X, Jiao C. Synergistic effects of hydroxy silicone oil on intumescent flame-retarded polypropylene system. Fire Safety Journal 2009; 16(44): 1010–1014.
2. Bao Z, Dong Y. Progress in studying expansive flame retardants (in Chinese). Chemical World 2006; 47(5): 311–315.
3. Cai Y, Fan H, Chen H, *et al.* Progress in epoxy nano flame- retarded materials (in Chinese). Thermosetting Resin 2007; 22(6): 50–53.
4. Marosi G, Marton A, Szep A, *et al.* Fire retardancy effect of migration in polypropylene nanocomposites induced by modified interlayer. Polymer Degradation and Stability 2003; 82(2): 379–385.
5. Hu Y, Song L. Flame-retarded polymer nanocomposites (in Chinese). Beijing: Chemical Industry Publishing House; 2008. p. 128–130.
6. Wang Z, Han E, Ke W. Study on improving the water resistance of APP/PER/MEL fire-proof coating (in Chinese). Journal of Chinese Society for Corrosion and Protection 2006; 26 (2): 103–107.
7. Wang J, Wang X, Wang W, *et al.* Study on PEPA/nanometer $Al(OH)_3$ instrument flame-retarded polypropylene. Plastics Additives 2006; 56(2): 35–38.
8. Feng C, Zeng Z, Ye J, *et al.* Effect of Nano-SiO_2 on properties of flame retarded PP by MPP/PEPA. Plastics Science and Technology 2009; 37(4): 67–70.
9. Mao W, Li Q. Study on the coefficieffect of nano zinc oxide on expanded flame-retarded nylon 66(in Chinese). Insulating Materials 2007; 40(3): 32–34.
10. Zhou J, Fang C, Sheng , *et al.* Synergistic action of Nanometer ZnO prepared by sol-gel method on halogen free flame-retarded polypropylene. Rare Metal Materials and Engineering 2008; 37(s2): 617–619.
11. Xian C, Meng H, Sun D, *et al.* Application of nanomaterials in fire-proof coatings of water-thin expansion steel structures (in Chinese). Journal of Material Engineering 2006; 23(8): 40–44.
12. Liu Z, Ou Y, Wu J. Combustion behaviors of PA6/OMMT nanocomposites flame-retarded by MPP/PER/APP system. Journal of Functional Polymers 2004; 17(4): 625–62.
13. Chen M, Wu Z, Hu Y. Research progress of magnesium hydroxide synergistic flame retardants (in Chinese). Applied Chemical Industry 2008; 37(8): 939–942.
14. Zhou B, Yang Y. Research status and development trend of magnesium hydroxide flame retardants (in Chinese). Journal of QiLu Normal University 2006; 116(4): 100–102.
15. Qu Z, Liu S, Jiang Z, *et al.* Study of the PA6/SAMH/PE ternary compound halogen-free flame-retarded system (in Chinese). China Plastics Industry 2009; 37(2): 50–53.
16. Zhao A, Dong Y, Bao Z. Synthesis of phosphate melamine borate flame-retardants (in Chinese). Shandong Chemical Industry 2009; 38(12): 1–6.
17. Robert M, Francis X, David J. Spectrometric identi-

fication of organic compounds. Shanghai: East China University of Science and Technology Press; 2007. p. 101–110.
18. Fan W, Sun S, Song X, *et al.* Controlled synthesis of single-crystalline $Mg(OH)_2$ nanotubes and nanorods via a solvothermal process. Journal of Solid State Chemistry 2004; 177(7): 2329–2338.
19. Song C, Hu Z, Fu X. Preparation and characterization of $Mg(OH)_2$ nanosheets. Journal of Qingdao University of Science and Technology (Natural Science Edition) 2009; 30(3): 200–202.
20. Zhang F, Zhang X, Tang Y. Synthesis and synthesis of highly pure ultra-thin sheet nano-magnesium hydroxide (in Chinese). Fire Protection Technique and Products Information 2009; (1): 7–9.
21. Han D, Shi L. Preparation of hydrophobic nano-$Mg(OH)_2$ by one-step method of alcohol water system. Chemical Minerals & Processing 2008; (6): 13–17.
22. Yin W, Nan L, Han Y, *et al.* Synthesis and crystallization mechanism analysis of nanometer magnesium hydroxide (in Chinese). Metal Mine 2005; 345(3): 38–41.
23. Zhou W, Zhou J, Yang H, *et al.* Flame retardant synergistic effect of nano $Mg(OH)_2$ and silicone on polypropylene (in Chinese). Rare Metal Materials & Engineering 2008; 37(S2): 312–315.
24. Laoutid F, Bonnaud L, Alexandre M, *et al.* New prospects in flame retardant polymer materials: From fundamentals to nanocomposites. Materials Science and Engineering: R Reports 2009; 63(3): 100–125.

Characterization and Application of Nanomaterials (2021) Volume 4 Issue 2
doi:10.24294/can.v4i2.1294

ORIGINAL RESEARCH ARTICLE

Template assisted nano-structured nickel for efficient methanol oxidation

S Mohanapriya*, V Raj

Advance Materials Research Lab, Department of Chemistry, Periyar University, Salem-636 011, India. E-mail: priyaechem@gmail.com

ABSTRACT

Nanoporous nickel has been prepared by electrodeposition using non-ionic surfactant based liquid crystalline template under optimized processing conditions. Physicochemical properties of nanoporous nickel are systematically characterized through XRD, SEM and AFM analyses. Comparison of electrocatalytic activity of nanoporous nickel with smooth nickel was interrogated using cyclic voltammetry (CV), chronoamperometry (CA) and electrochemical impedance spectroscopy (EIS) analyses. Distinctly enhanced electrocatalytic activity with improved surface poisoning resistance related to nanoporous nickel electrode towards methanol oxidation stems from unique nanoporous morphology. This nanoporous morphology with high surface to volume ratio is highly beneficial to promote active catalytic centers to offer readily accessible Pt catalytic sites for MOR, through facilitating mass and electron transports.

Keywords: Template Deposition; Electrocatalysis; Methanol Oxidation; Direct Methanol Fuel Cell

ARTICLE INFO

Received: 20 May 2021
Accepted: 11 July 2021
Available online: 18 July 2021

1. Introduction

Owing to the simplified system design, high energy density, and ease of transportation of fuel, direct methanol fuel cells (DMFCs) are currently at the forefront as renewable energy sources which involve electrochemical energy conversion and hence suitable for automotive as well as portable power applications[1–4]. Till now, Platinum (Pt) and its alloys represent the most extensively used DMFC electrocatalysts on account of their superior catalytic activity and stability towards oxidation of methanol at the anode side[5–7]. But the catalytic activity of the Pt surface could easily be deteriorated by the adsorption of CO generated during methanol oxidation reaction (MOR).

Promoting the effect of Ni over Pt catalytic activity both in acidic and alkaline mediums is well established in the literature[8–10]. Earlier studies established the role of nickel in assisting the dissociative adsorption of water molecules to produce-OH ads species, which facilitates the oxidation of CO adsorbed on Pt surface, thereby favors regeneration of Pt catalytic centers. Many electrodes involving nickel as a component in their manufacture can be used as catalysts in fuel cells. It is commonly used as an electrocatalyst for both anodic and cathodic reactions in organic synthesis and water electrolysis[15–18].

A very important application of nickel as a catalyst is the

oxidation of alcohol. Several studies on the electro-oxidation of alcohol on nickel have been reported. Alkaline direct methanol fuel cells are now receiving considerable attention because they allow the use of anion exchange membranes that reduce methanol cross-over—a serious problem with cation exchange membrane used in acidic methanol fuels[8]. Another reason for using an alkaline medium is because the kinetics for both methanol oxidation and oxygen reduction reactions is found to be more facile in an alkaline medium than in an acidic one[9–12]. In recent years, researchers focus on finding cheaper alternative electrocatalysts and improving the overall cell performance. Non-noble transition metal electrocatalysts such as copper[13–16], nickel[17–24], which oxidize methanol and other alcohols, offer good alternative electrocatalysts. The activity of nickel- based electrocatalysts depends on the method of preparation of these electrodes. Rahim *et al.*[24] showed that only nickel dispersed in graphite is catalytically active for methanol oxidation while massive nickel is not. In addition, this nickel electrocatalyst loses its performance due to the possible loss of nickel oxide activity after continuous circulation[24]. This is believed to be due to the increased thickness of NiO(OH), which acts as a barrier inhibiting the charge transfer process for methanol oxidation. Alternative approaches to prepare nickel electrocatalysts that can minimize the buildup of such a barrier layer would be of great interest in the development of non-noble metal electrodes for methanol oxidation. The purpose of the present work is to establish the electro-catalytic oxidation of methanol on Nanoporous nickel in a solution of 1.0 M NaOH. Surfactant mesophases come under the category of soft template systems and electrodeposition through them is a very useful and versatile method for the synthesis of nanostructured materials. In addition, lyotropic liquid crystalline phases possess a long-ranged spatially periodic architecture with lattice parameters in the range of a few nanometers. This makes them ideal candidate systems for the synthesis of nanomaterials. In this study, we report a simple electrochemical method of preparing a high surface area for nanoporous nickel deposit, using a new hexagonal liquid crystalline phase as a template. This room-temperature deposited nickel has been characterized by electrochemical techniques such as cyclic voltammetry (CV) and electrochemical impedance spectroscopy. Besides, scanning electron microscopy (SEM), atomic force microscopy (AFM), and X-ray diffraction (XRD) are also used for surface characterization. The catalytic efficiency of synthesized nanoporous nickel is evaluated by methanol oxidation using the techniques such as CV, Impedance, etc. And morphology and composition of nanoporous nickel cloud easily be tuned through controlling parameters involved in electrodeposition.

2. Materials and methods

2.1 Chemicals

Triton X-100 (Spectrochem), Polyacrylic acid (PAA) (Aldrich), sodium hydroxide pellets (Emerck), Ni(II) chloride (EMerck), nickel sulphamate (Grauer and Wheel), boric acid (Sarabhai chemicals) were used in this study. All chemical reagents used were AnalaR (AR) grade. Millipore water having a resistivity of 18 M cm was used in all the experiments.

2.2 Preparation and characterization of hexagonal liquid crystalline phase

The hexagonal liquid crystalline phase was prepared from a ternary mixture of Triton X-100, PAA, and water. We have carried out our studies at two different weight compositions viz., Triton X-100 + water (42/58 vol%). The mixture was stirred in a magnetic stirrer at a temperature of 33–35 °C for 1 h and cool down to room temperature. When viewed under a polarized light microscope, the mixture shows the characteristic birefringence of a hexagonal liquid crystalline phase-stable up to 29 °C. All the electrodeposition using this phase as a template has been done at the room temperature of 25 °C.

2.3 Nickel electroplating through hexagonal liquid crystalline

The electrodeposition of Nanoporous nickel was performed in a standard three-electrode glass cell using Al as a working electrode, a saturated calomel

electrode (SCE), and Pt foil served as a reference and counter electrodes respective. Nanoporous nickel synthesizes through electrodeposition at a constant of –1 V for a different periods. For electrodeposition, we have prepared the aqueous phase of the above described hexagonal liquid crystalline system from the standard nickel sulfamate bath[21] of the composition: 300 g/L nickel sulfamate, 6 g/L nickel chloride, and 30 g/L boric acids.

3. Results and discussion

3.1 Micro-structural analyses

Interesting electrocatalytic properties is exhibited by mesoporous nickel owing to their high surface area, unique morphology and high conductivity. Schematics of synthesis of steps involved in the process of preparation of Nanoporous nickel is illustrated in **Figure 1**. Triton X 100 forms micelles aggregated in the aqueous phase. Nickel ions encapsulated in the micelles of Triton X100 undergoes electrochemical reduction in such way that meso domains are created over the surface. Textural properties of nickel deposit are modified due to entrapment of nickel ions inside the micelles.

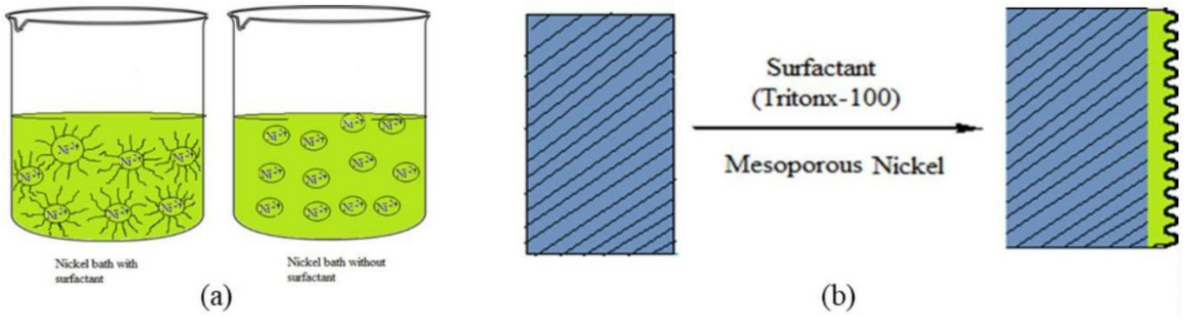

Figure 1. Preparation of the nanoporous nickel. **(a)** Pictorial representation of nickel bath with and without surfactant; **(b)** Schematic representation for preparation of Nanoporous nickel.

Nanoporous nickel was characterized by X-ray powder diffraction (XRD). XRD pattern of nickel deposited electrodes reveals the characteristic peaks expected for nickel with face-centered cubic (FCC) structure in addition to the reflections observed for bare Al electrode. Nanoporous nickel deposited show the peaks at 44.3° and 51.8° corresponding to (111) and (200) planes respectively and are indicated by the asterisk mark in the figure. The ratio of intensities of (111) and (200) planes associated with these nickel electrodes with and without surfactant suggests that there is a preferential growth and orientation of nickel film along (200) direction in the case of surfactant electro deposition. It can be noticed from the figure that the XRD pattern of nickel deposited electrodes reveals the characteristic peaks expected for nickel with a face-centered cubic structure.

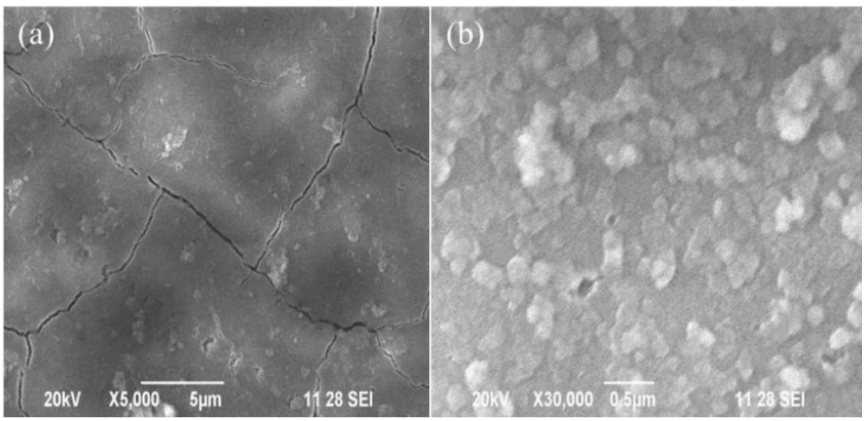

Figure 2. SEM images of **(a)** nanoporous nickel and **(b)** smooth nickel.

SEM pictures of nickel deposited on with and without the addition of Triton-X 100 are shown in **Figure 2**. The morphology of an individual deposit depends upon the electrolyte used for deposition. These images display the distinguishable structural features indicating the homogeneous growth of nickel deposits. Compared with nickel electrode produced without template, nickel deposited by template shows higher uniform growth.

The particles are same-sized spheres with smooth surfaces, the surface area can be related to the average equivalent particle size by $d = 6000/(\rho.s)$ (in nm), where d is the average diameter of spherical particle in manometer; ρ is the theoretical density of nickel (g/cm^3) and s represents the measured surface area of the powder in m^2/g. The size of the particles is in the range of 5–10 μm. Compared to the both images, nanoporous nickel surface morphologies present higher roughness.

AFM studies also validate the above observation as presented by **Figure 3**. AFM studies are used to demonstrate the difference in topography of nanoporous nickel and smooth nickel. Difference in the surface topographies related to nanoporous nickel and smooth nickel are evaluated through AFM analysis. Nanoporous structure helps to improve electronic conductivity which is highly advantageous for efficient electrocatalysis. The modulations in the height profile indicate that synthesized nanoporous nickel is associated with high degree of roughness. Surface modulations on the nanoporous nickel drastically increase the roughness factor associated with it, however nickel deposited using electrolyte bath without addition of surfactant exhibits two times lower roughness.

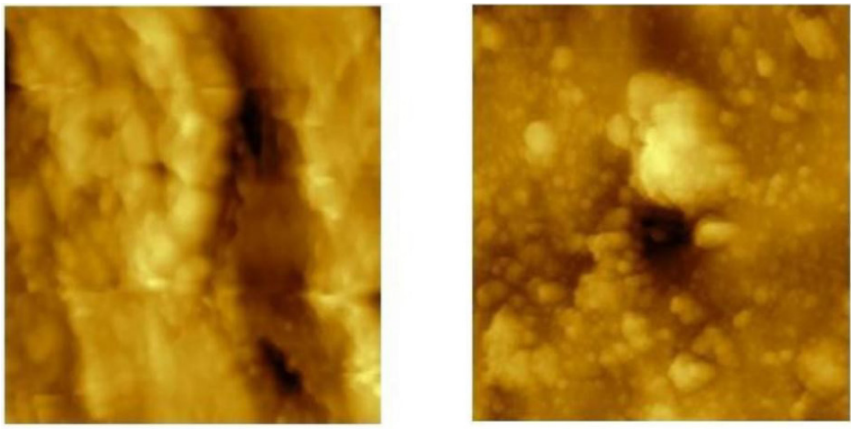

Figure 3. AFM images of smooth nickel and Nanoporous nickel.

It is because that this unique porous structure electrocatalytic activity of nanoporous nickel is higher. Distinct porous structure of nanoporous deposits substantially increases the surface area. SEM and XRD studies are in good agreement with AFM results.

3.2 Electrochemical studies

The electrochemical activity of mesoporous nickel electrode was studied by cyclic voltammetry, amperometry and electrochemical impedance techniques. The cyclic voltammograms (CV) of nickel deposited with and without the addition of Triton-X100 were recorded in alkaline medium. The CV measurements were conducted in 0.1 M NaOH at scanning rate of 100 mV/s. The applied potential was limited between 1 and –1 V.

When discussing the electrochemical behavior of nickel, it is convenient to consider the three oxide phases formed when a positive potential is applied to the metallic nickel electrode. A cyclic voltammetry (CV) profile of nickel in aqueous alkaline solution reveals features corresponding to the formation of three oxide species as the potential increased from –1 to 1 V vs hydrogen evolution reaction. The an-

odic peak corresponding to the formation of the first surface oxide, α-$Ni(OH)_2$, is present in the V range of –1 to 1 V. If the CV scan is reversed at a potential lower than 0.50 V, the full reduction of α-$Ni(OH)_2$ to metallic nickel will occur, giving rise to a cathodic peak in the CV profile at $-1 \leq E \leq 1$ V. When the potential is brought to values lower than 0 V, appreciable current density as a result of the hydrogen evolution reaction (HER) is observed along with the formation of H_2 (gas) bubbles at the electrode. The HER overlaps in potential with the reduction of α-$Ni(OH)_2$.

If the forward CV scan continues to have potentials higher than 0.50 V, the α- $Ni(OH)_2$ already present on the electrode converts to β-$Ni(OH)_2$, and an additional β-$Ni(OH)_2$ is formed. This species forms in the E region between 0.50 V and 1.30 V, which is known as the passive potential region for a nickel. Of these two $Ni(OH)_2$ structures, the β phase is more stable. The formation of this phase is irreversible, meaning that β-$Ni(OH)_2$ cannot be removed from the surface of the electrode by simply reversing the potential and reducing the oxide electrochemically. Once formed, β-$Ni(OH)_2$ can be removed through chemical etching, mechanical polishing, and thermal reduction in a hydrogen environment. The α- and β-$Ni(OH)_2$ species have different crystallographic structures; the α phase incorporates either water or alkali cations from the electrolyte and has a lattice constant that is larger than that of β-$Ni(OH)_2$. The final oxidation species to be formed is NiOOH. At $E >$ 1.30 V, the β-$Ni(OH)_2$ species is oxidized reversibly to β-NiOOH, which has a similar crystallographic structure and lattice constant. If an increasing positive potential is continuously applied, a γ-NiOOH phase is formed. This species adopts a crystallographic structure similar to that of α-$Ni(OH)_2$ and can be electrochemically reduced back to β-$Ni(OH)_2$.

From **Figure 4a**, it is evident that nanoporous nickel deposits present a higher current density compared to smooth nickel prepared without the addition of surfactant. It reports that periodic nanoporous structures with a high surface area can have charge storage capacity by one order over that of the bulk materials. Increased electrochemical surface area of nanoporous deposits are due to the presence of Triton-X100 molecules during a deposition process. These surfactant molecules act as a template during deposition, create mesopores in the nickel surface, and favor the formation of highly active nanoporous nickel deposits. Owing to the larger surface area, electrochemically active surface area is also higher for the nanoporous nickel deposits.

Higher roughness associated with mesopores nickel is due to the larger number of electrolytes accessing channels formed over nanoporous nickel due to more availability of electrolyte access-electrochemical surface area. In other words, through the nanoporous deposits, electrolytes could easily reach the nickel surface compared to smooth nickel.

The electrocatalytic response of prepared nickel deposits is evaluated through the addition of 1 M methanol. CV curves of nickel deposits before and after the addition of 1 M methanol in 0.1 M aqueous

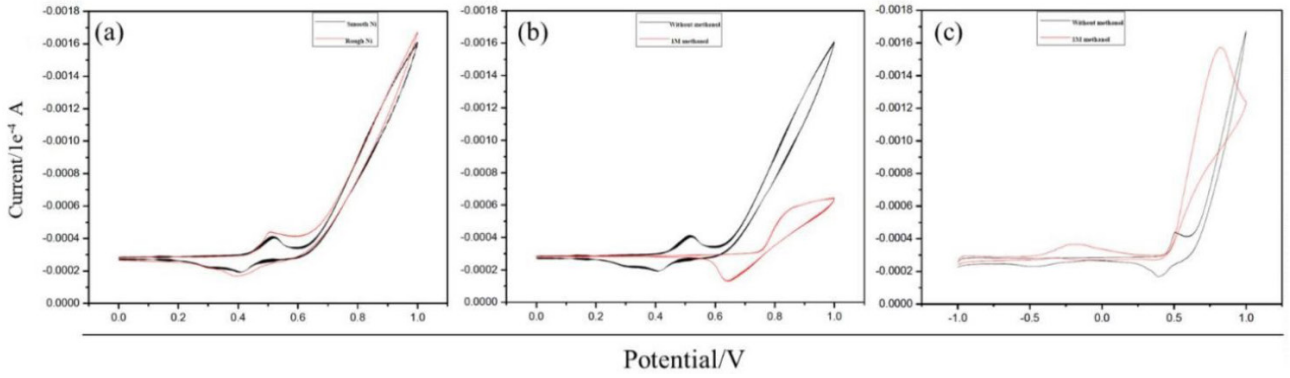

Figure 4. Cyclic voltammetric curves of different nickel materials scanned from –1 to 1V at a rate of 50 mV/s in 0.1 M NaOH. **(a)** Nanoporous nickel and smooth nickel; **(b)** smooth nickel with and without 1M methanol, and **(c)** nanoporous nickel with and without 1 M methanol.

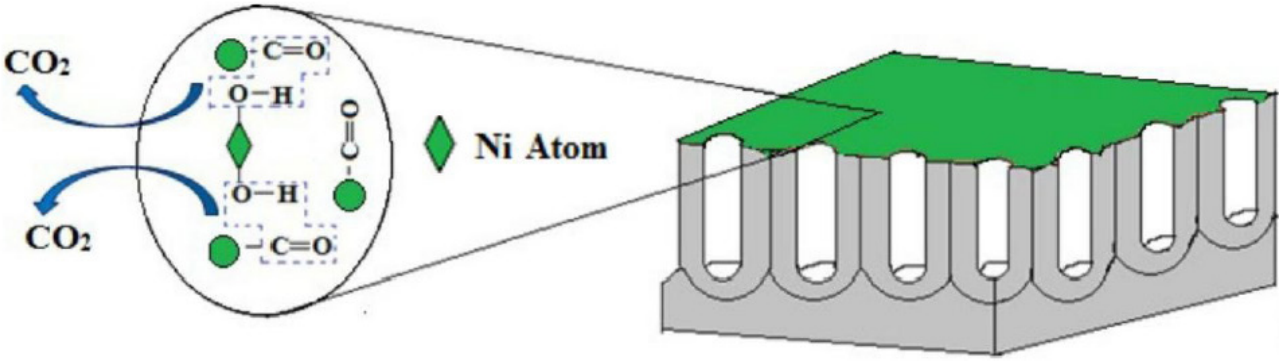

Figure 5. Mechanism of electro-oxidation of methanol on nanoporous nickel catalyst.

NaOH solution are given in **Figure 4b** and **Figure 4c** correspondingly. Since NiOOH was constantly being reduced back to $Ni(OH)_2$, once methanol oxidation started, some anodic current could always be attributed to the continuous re-oxidation of $Ni(OH)_2$ back to NiOOH. Furthermore, during the cathodic scans, lingering methanol oxidation caused some portion of the electrode surface to be prematurely reduced to the Ni(II) oxidation state before the Ni(III)/Ni(II) reduction occurred, thus decreasing the amount of NiOOH on the surface and the magnitude of the corresponding peak. By comparing the electrocatalytic response of methanol on nanoporous nickel and smooth nickel, it is clear that the anodic peak current associated with methanol electro-oxidation is higher for nanoporous nickel. An increase in the anodic peak current on the addition of 1 M methanol is 0.0012 and 0.0002 mA/cm^2 for nanoporous nickel and smooth nickel respectively. The improved current response demonstrates the significance of nanoporous structure.

The onset of methanol oxidation occurs at about 500 mV at the nanoporous nickel electrode whereas methanol oxidation begins from 550 mV with a smooth nickel electrode. A lower onset potential associated with nanoporous nickel evidences higher electrocatalytic activity for MOR. The superior catalytic activity of nanoporous nickel may stem from unique porous morphology associated with higher ESCA. It is evident that the peak potential at which methanol oxidation occurs on nanoporous nickel is 0.75 V, but 0.85 V for a smooth nickel.

As well known, the forward current peak (*If*) is attributed to the oxidation of methanol molecule and the backward current peak (*Ib*) to the oxidation of adsorbed intermediates such as CO, CH_xOH ($0 < x < 2$), CH_xO, HCOO- and so on. Hence, the number of oxidizable intermediates adsorbed over the catalytic surface could be predicted by the relative magnitude of backward peak. (*If*)/(*Ib*) ratio is a measure of the efficiency of a catalyst to tolerate the poisoning of the surface due to adsorption of incompletely oxidized intermediates. (*If*)/(*Ib*) value for nanoporous nickel and smooth nickel is 1.3 and 1.17 respectively, which are higher than that of pure Pt as reported earlier. A higher (*If*)/(*Ib*) value indicates that most of the intermediate carbonaceous species were oxidized to carbon dioxide in the forward scan on the nanoporous nickel electrode. Increased CO tolerance of nanoporous nickel electrode may be attributed due to the basic difference in methanol oxidation between nanoporous and nonporous structure, which could be explained on the basis of morphology-dependent CO tolerance as demonstrated earlier.

Based on the results, it could be inferred that nanoporous architecture increases poisoning tolerance of the catalyst through influencing the availability of continuous binding sites for C-H bond cleavage and enhances a greater number of readily accessible active catalytic sites for methanol oxidation reaction (MOR). The schematic illustration of the mechanism of CO removal over nanoporous nickel is depicted in **Figure 5**.

Various concentrations of methanol 2 M, 3 M, 4 M, and 5 M were added to smooth nickel and nanoporous nickel. Smooth nickel has good electrocatalytic activity, but surfactant tritonx-100 nickel has high electrocatalytic activity shown in **Figures**

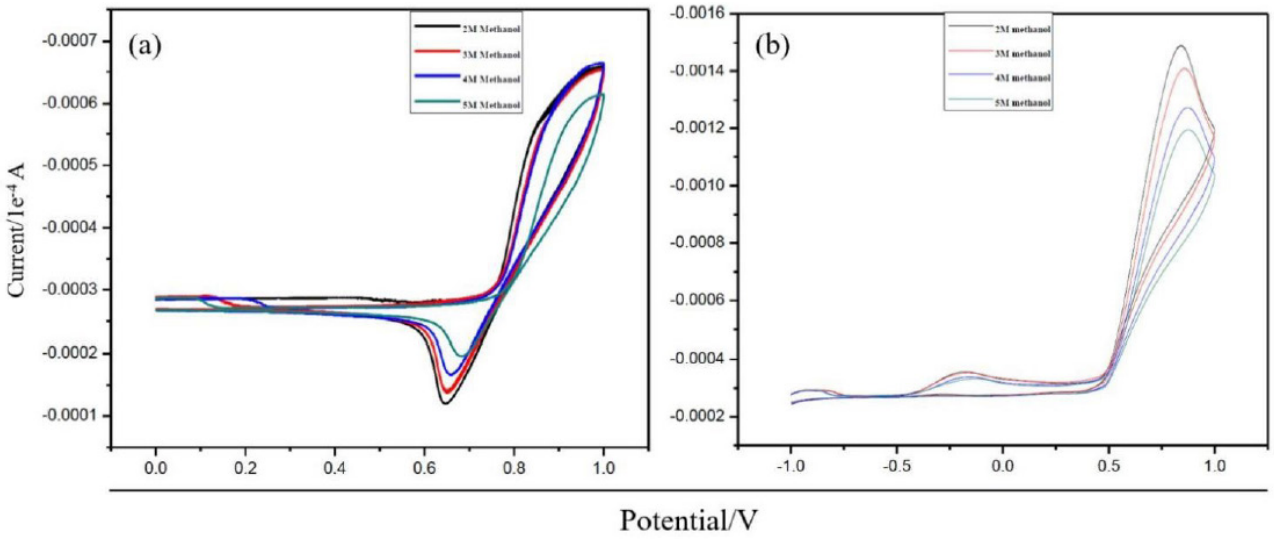

Figure 6. Cyclic voltametric curves of **(a)** smooth nickel and **(b)** nanoporous nickel in various concentration of methanol scanned from –1 to 1V at a rate of 50 mV/s performed in 0.1 M NaOH.

6a and **6b** respectively.

CV curves were used to examine the electrochemical properties of nanoporous nickel in an aqueous alkaline electrolyte and to relate such acquired insight to their chemical composition and surface characteristics. Typical CV curves for bulk nickel in aqueous NaOH solution in the –1 to +1 V potential (E) range show the following anodic features:

i. Oxidation of metallic nickel to α-$Ni(OH)_2$ at $0.20 < E < 0.40$ V;

ii. Concurrent conversion of α- to β-$Ni(OH)_2$ and oxidation of metallic nickel to β-$Ni(OH)_2$ at $0.50 < E < 1.30$ V;

iii. The oxidation state of Ni Increases from +2 to +3 through the oxidation of β-$Ni(OH)_2$ to β-NiOOH at $1.30 < E < 1.55$ V;

iv. Oxygen evolution reaction (OER) at $E \geq 1.55$ V.

The β phase of $Ni(OH)_2$ is the most stable and thermodynamically favored oxide of nickel; it is the passive layer that develops on the surface of metallic nickel upon contact with the ambient environment. The conversion of α- to β-$Ni(OH)_2$ is irreversible, and once it takes place, the cathodic peak corresponding to the reduction of α-$Ni(OH)_2$ is not observable anymore. The reduction of β-$Ni(OH)_2$ cannot be accomplished electrochemically and can be achieved at elevated temperatures in the presence of H_2 (g). The anodic and cathodic peaks characteristic of α-$Ni(OH)_2$ formation and reduction are not observed because a layer of β-$Ni(OH)_2$ has developed as the result of several prior CV scans. The CV curves for nickel nanoporous display the same features as those observed for smooth nickel in alkaline media. The CV curves for nanoporous nickel reveal pronounced differences, especially in the anodic scan. Compared to the mesoporous nickel, the peak is shifted towards higher potentials and overlaps the region of OER. The value of I_s for OER is greater than that of nickel nanoporous; the specific current for the cathodic feature is greater than that of nickel nanoporous, but the difference is small. Nickel and nanoporous nickel have very different surface morphologies, and the rough, bubbly surface of nanoporous nickel gives rise to a larger surface area than a smooth nickel. The charges under the two cathodic peaks are similar, thus indicating that both samples have similar amounts of β-NiOOH on the surface. The difference in Q_s values for smooth nickel is less than 40%, and that nanoporous nickel has a significantly larger actual surface area, we conclude that β-NiOOH does not make up the entire surface of nanoporous nickel.

3.3 Chronoamperometry

To evaluate the long-term activity of the catalyst, the steady-state current responses of nanoporous nickel and smooth nickel were recorded (**Figure 7**).

Initial rapid current decay for both catalysts is due to double-layer capacitance. Transient current due to methanol oxidation attains a steady state after 820 s and 1600 s with nanoporous nickel electrode and smooth nickel electrode respectively, indicating the better catalytic performance of the former. It could be noticed from chronoamperometric results that the addition of 1 M methanol shows an increased electrocatalytic response on nanoporous nickel surface but the increased current response is not very high with smooth nickel. As evident from the figures, the addition of 1 M methanol causes an increase in current 0.07 A/cm^2 for nanoporous nickel and 0.0001 mA/cm^2 for smooth nickel.

Methanol oxidation current tends to decrease due to the accumulation of adsorbed species on catalyst surfaces due to the decomposition of methanol molecules. By comparing the current responses, it is obvious that the nanoporous nickel electrode possesses enhanced catalytic durability. Unique nanoporous structure comprising continuous Meso channels is highly favorable to provide easy transport paths of electrons and reaction intermediates, therefore, enhances MOR activity of nanoporous nickel electrode.

3.4 Impedance studies

To further extract information about the electro catalytic process, EIS studies are performed. **Figures 8a** and **8b** represent Nyquist plots recorded at 500 mV dc-offset potential in 0.1 M NaOH with methanol for nanoporous nickel and smooth nickel electrodes respectively.

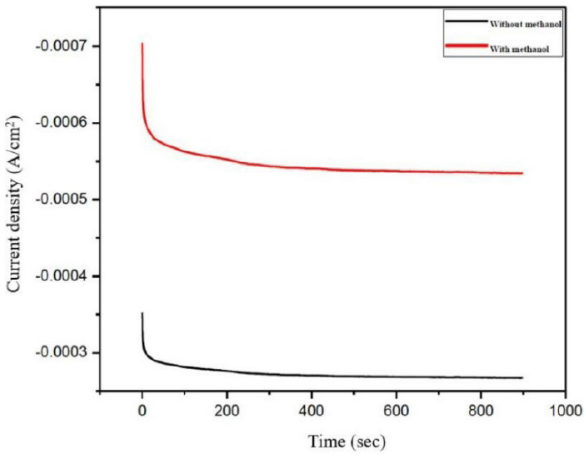

Figure 7. Amperometric curves of Nanoporous nickel with and without 1 M methanol.

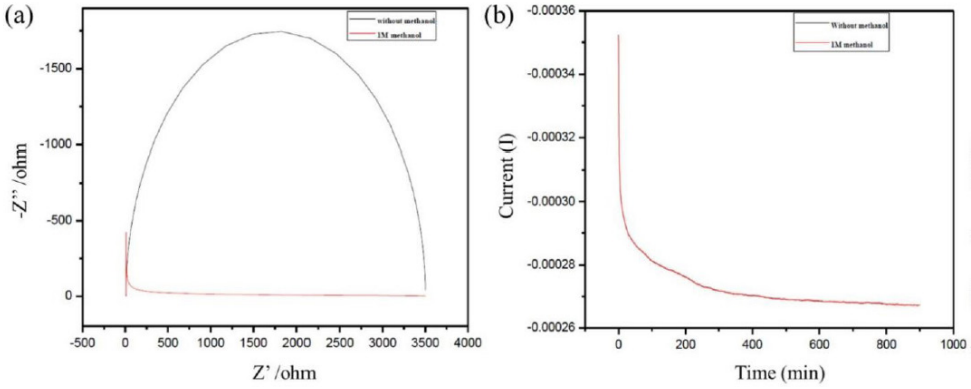

Figure 8. Impedance of **(a)** Nanoporous nickel and **(b)** smooth nickel deposition, with or without 1 M methanol.

General pattern of Nyquist plot obtained with electrodes under study is unaltered on changing the concentration of methanol from 0.1 to 4 M, pointing that mechanism of methanol oxidation is not affected by methanol concentration. Conversely, diameter of semicircle has been dramatically decreased on increasing the concentration of methanol, denoting that charge transfer resistance (Rct) regularly drops.

EIS analysis was carried out by fitting the data with appropriate equivalent circuit as shown in **Table 1**. Equivalent circuit is composed of solution resistance (R_s), double layer capacitance (CPE_1) and charge transfer resistance (R_{ct}) associated with MOR. Porous nature of electrode is attributed by the presence of additional elements namely CPE_2 and R_f. The values for all the parameters R_{ct}, CPE_1, CPE_2, and their associated % error determined by the fitting of the experimental EIS data are summarized in **Table 1**.

Table 1. Numerical values of elements in the equivalent circuit fitted with Nyquist plots of nanoporous and smooth nickel

Type	R_s (Ω)	CPE_1 ($\times 10^6$ ΩS^n)	n_1	R_{ct} (Ω)	CPE_2 ($\times 10^6$ ΩS^n)	n_2	R_f (Ω)	[Methanol] (mol/L)
Nanoporous nickel	14.80	4.186	0.91	1866.7	9.930	0.92	32380	0
	12.78	5.636	0.87	875.5	7.950	0.94	632.7	1
	11.65	6.100	0.88	153.3	4.280	0.91	449.7	2
	11.50	2.680	0.92	102.2	2.998	0.93	427.2	3
	11.58	4.220	0.96	82.2	1.746	0.89	499.1	4
Smooth nickel	15.10	5.767	0.88	3381.9	2.500	0.89	89342	0
	15.02	3.761	0.89	1505.0	4.536	0.90	6861.4	1
	12.50	2.504	0.85	771.4	3.089	0.91	739.5	2
	12.30	5.766	0.91	537.8	5.292	0.89	324.8	3
	12.32	4.340	0.89	331.7	4.700	0.95	241.9	4

The parallel combination of the charge-transfer resistance (R_{ct}) and CPE take into account for methanol adsorption and oxidation on porous thin film.

From **Figure 8a**, it can be seen that the R_{ct} values are found to decrease in the order 1 M methanol > without methanol. Without methanol is low resistance compared to 1 M methanol. The diameter of the semicircle is proportional to the value of the impedance. The smaller the value of impedance, the better the conducting property of the coating will be. This can be further confirmed by its low resistance and high capacitance.

Likewise, the equivalent circuit shown **Figure 8b** is a simplified electrochemical model, which has been used to fit the impedance data obtained for the composite coatings present on substrate. As can be seen from the equivalent circuit, R_s refers to the resistance of the solution, C_{dl} is the electric double layer capacitance and R_{ct} is the charge transfer resistance that represents the electrochemical activity of the electrode. Based on equivalent circuit model proposed, these EIS curves were best fitted. Various concentration of methanol solution in Tritonx-100 surfactant of the deposited nickel has low resistance and high capacitance.

The parallel combination R_{ct} with CPE leads to a depressed semicircle in the corresponding Nyquist impedance plot. It is noteworthy that R_{ct} is an order lower for nanoporous nickel than that of smooth nickel, which reflects the enhanced electrocatalytic activity of the former (**Figure 9**). The electrochemical impedance spectroscopic (EIS) is a power tool for studying the electrochemical behavior of electrode.

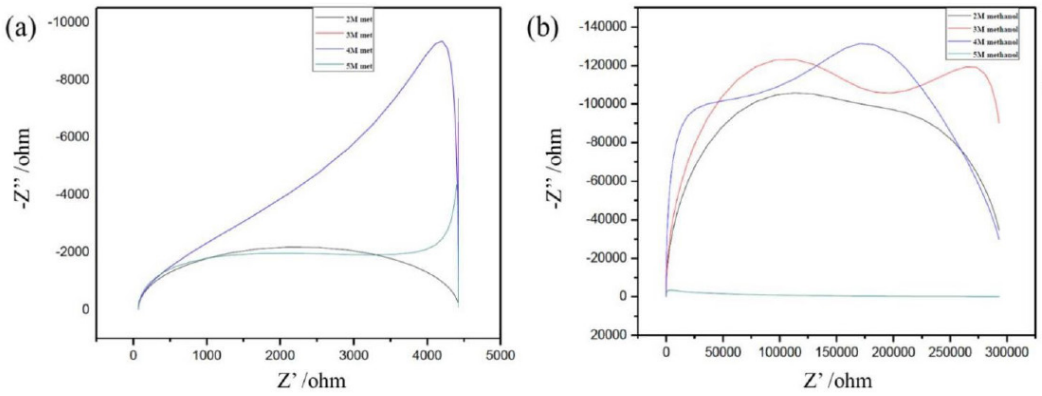

Figure 9. Impedance of **(a)** nanoporous and **(b)** smooth nickel deposition at 2, 3, 4 and 5 M methanol.

4. Conclusions

In a nutshell, a facile and simple approach to produce nanoporous nickel through electrode-position is by using surfactant Triton-X100. The developed methods are scalable and reproducible Triton-X100 template could be easily removed by washing the electrode with water. Nanoporous nickel has been prepared by surfactant assistant assisted electrochemical deposition of nickel under optimized process conditions. Surface characteristics of the nanoporous nickel and smooth nickel were systematically characterized through XRD, SEM, and AFM analyses. Nanoporous morphology is highly beneficial to offer readily accessible catalytic sites for methanol oxidation reaction (MOR), through facilitating mass and electron transport. The prepared nickel was used as electrocatalyst for DMFC. Comparison of electrolytic activity of nanoporous nickel with smooth nickel was interrogated using cyclic voltammetry (CV), chronoamperometry (CA) and electrochemical impedance spectroscopy (EIS) analyses. Distinctly enhanced electrocatalytic activity with improved CO tolerance associate with nanoporous nickel electrode towards methanol oxidation stems from readily accessible high surface area associated with nanoporous structured, which facilitate mass transport of both the reactants and products.

Conflict of interest

No conflict of interest was reported by the authors.

Acknowledgements

One of the authors S. Mohanapriya is grateful to University Grants Commission (UGC), Government of India, for providing fund under the scheme of "UGC-Dr. D. S. Kothari Post-Doctoral Fellowship". (Ref: No. Award Letter No.F.4-2/2006 (BSR)/CH/14-15/0102 dated 5-5-2015).

References

1. Liu H, Song C, Zhang L, *et al.* A review of anode catalysis in the direct methanol fuel cell. Journal of Power Sources 2006; 155(2): 95–110.
2. Neburchilov V, Martin J, Wang H, *et al.* A review of polymer electrolyte membranes for direct methanol fuel cells. Journal of Power Sources 2007; 169(2): 221–238.
3. Mohanapriya S, Bhat SD, Sahu AK, *et al.* A new mixed-matrix membrane for DMFCs. Energy & Environmental Science 2009; 2(11): 1210–1216.
4. Mohanapriya S, Bhat SD, Sahu AK, *et al.* Sodium-alginate-based proton-exchange membranes as electrolytes for DMFCs. Energy & Environmental Science 2010; 3(11): 1746–1756.
5. Mohanapriya S, Sahu AK, Bhat SD, *et al.* Bio-composite membrane electrolytes for direct methanol fuel cells. Journal of the Electrochemical Society 2011; 158(11): B1319–B1328.
6. Mohanapriya S, Bhat SD, Sahu AK, *et al.* Modified-bio-polymeric-mixed-matrix-membrane electrolytes for direct methanol fuel cells. Journal of Bionanoscience 2009; 3(2): 131–138.
7. Suganthi S, Mohanapriya S, Raj V. Biocomposite proton-exchange membrane electrolytes for direct methanol fuel cells. Journal of Applied Polymer Science 2016; 133(25): 43514.
8. Iwasita T. Electrocatalysis of methanol oxidation. Electrochimica Acta 2002; 47: 3663–3674.
9. Radmilovic V, Gasteiger HA, Ross PN. Structure and chemical composition of a supported Pt-Ru electrocatalyst for methanol oxidation. Journal of Catalysis 1995; 154(1): 98–106.
10. Antolini E, Salgado J, Gonzalez ER. The methanol oxidation reaction on platinum alloys with the first row transition metals: The case of Pt–Co and –Ni alloy electrocatalysts for DMFCs: A short review. Applied Catalysis B Environmental 2006; 63(1-2): 137–149.
11. Wasmus S, Kuver A. Methanol oxidation and direct methanol fuel cells: A selective review. Journal of Electroanalytical Chemistry 1999; 461(1-2): 14–31.
12. Iwasita T, Hoster H, John-Anacker A, *et al.* Methanol oxidation on PtRu electrodes. Influence of surface structure and Pt-Ru atom distribution. Langmuir 2000; 16(2): 522–529.
13. Wang K, Gasteiger HA, Markovic NM, *et al.* On the

reaction pathway for methanol and carbon monoxide electrooxidation on Pt-Sn alloy versus Pt-Ru alloy surfaces. Electrochimica Acta 1996; 41(16): 2587–2593.
14. Hu Y, Zhang H, Wu P, *et al.* Bimetallic Pt-Au nanocatalysts electrochemically deposited on graphene and their electrocatalytic characteristics towards oxygen reduction and methanol oxidation. Physical Chemistry Chemical Physics Cambridge Royal Society of Chemistry 2011; 13: 4083–4094.
15. Liu X, Cui C, Gong M, *et al.* Pt–Ni alloyed nanocrystals with controlled architectures for enhanced methanol oxidation. Chemical Communications 2013; 49: 8704–8706.
16. Xu D, Liu Z, Yang H. Solution-based evolution and enhanced methanol oxidation activity of monodisperse platinum-copper nanocubes. Angewandte Chemie International Edition 2009; 48(23): 4217–4221.
17. Mohanapriya S, Suganthi S, Raj V. Mesoporous Pt–Ni catalyst and their electro catalytic activity towards methanol oxidation. Journal of Porous Materials 2017; 24(2): 355–365.
18. Abdel Rahim MA, Hassan HB, Abdel Ham RM. Graphite electrodes modified with platinum-nickel nano-particles for methanol oxidation. Fuel cells 2007; 7(4): 298–305
19. Niu Z, Wang D, Yu R, *et al.* Highly branched Pt–Ni nanocrystals enclosed by stepped surface for methanol oxidation. Chemical Science 2012; 3(6): 1925–1929.
20. Ganesh V, Lakshminarayanan V. Preparation of high surface area nickel electrodeposit using a liquid crystal template technique. Electrochimica Acta 2004; 49(21): 3561–3572.
21. Xia Y, Xiong Y, Lim B, *et al.* Shape-controlled synthesis of metal nanocrystals: Simple chemistry meets complex physics? Angewandte Chemie International Edition 2009; 48(1): 60–103.
22. Mohanapriya S, Tintula KK, Bhat SD, *et al.* A novel multi-walled carbon nanotube (MWNT)-based nanocomposite for PEFC electrodes. Bulletin of Materials Science 2012; 35(3): 297–303.
23. Julia van D, Brandy Kinkead P, Yoseif M, *et al.* Electrochemically active nickel foams as support materials for nanoscopic platinum electrocatalysts. ACS Applied Materials & Interfaces 2014; 6(15): 1–73.
24. Mohanapriya S, Suganthi S, Raj V. Mesoporous Pt–Ni catalyst and their electro catalytic activity towards methanol oxidation. Journal of Porous Materials 2017; 24(2): 355–365.
25. Xing W, Li F, Yan Z, *et al.* Synthesis and electrochemical properties of mesoporous nickel oxide. Journal of Power Sources 2004; 134(2): 324–330.
26. Skowronski JM, Wazny A. Nickel foam-based $Ni(OH)_2$/NiOOH electrode as catalytic system for methanol oxidation in alkaline solution. Journal of New Materials for Electrochemical Systems 2006; 9(4): 345–351.
27. Rahim M, Hameed R, Khalil MW. Nickel as a catalyst for the electro-oxidation of methanol in alkaline medium. Journal of Power Sources 2004; 134(2): 160–169.

Characterization and Application of Nanomaterials (2021) Volume 4 Issue 2
doi:10.24294/can.v4i2.1333

ORIGINAL RESEARCH ARTICLE

Sedimentation of nanoparticle titanium dioxide in the presence of ammonium

Duo Li[1,2], Nan Xu[1,2*]

[1] *School of Chemistry, Biology and Materials Engineering, Suzhou University of Science and Technology, Suzhou 215009, Jiangsu, China*

[2] *Jiangsu Key Laboratory of Environmental Functional Materials, Suzhou 215009, Jiangsu, China. E-mail: nanxu@mail.usts.edu.cn*

ABSTRACT

Due to its physicochemical properties, nanoparticles titanium dioxide ($nTiO_2$) is being put into mass production and widespread applications, which inevitably results in their increasing exposure to the water body. After it entering the water body, the chemical properties of $nTiO_2$ can be influenced by ion compositions, ion strength and pH, which affects their ecological risk. Excess of ammonium (NH^{4+}) fertilizer has contaminated soil and water environments. In this paper, the Zeta potentials and hydrodynamic radius of $nTiO_2$ were studied in NH^{4+} solution compared to those in Na^+ solution. In addition, the sedimentation rate of $nTiO_2$ was also investigated. The experiment results show that high pH inhibits the sedimentation of $nTiO_2$. Moreover, NH^{4+} increases the stability of $nTiO_2$ more than Na^+ at the same IS, which was attributed the more negative Zeta potentials and the smaller hydraulic radius. Our results provide a theoretical basis for evaluating the ecological risk of $nTiO_2$ in aqueous solution containing NH^{4+}.

Keywords: Ammonium; Chloride; Nanoparticles Titanium Dioxide ($nTiO_2$); Sedimentation; Zeta Potential

ARTICLE INFO

Received: 13 June 2021
Accepted: 5 August 2021
Available online: 12 August 2021

1. Introduction

Nanomaterials have small size effects, surface effects, quantum size effects, and macroscopic quantum tunneling effects, so that nanomaterials are widely used in medical[1], chemical[2], environmental[3], microelectronics[4] and other industries. Nanotitanium oxide ($nTiO_2$), as common nanomaterial, is heavily produced and widely used due to low production cost, good chemical stability and strong photocatalytic capacity[5]. In the production and consumption of $nTiO_2$, some $nTiO_2$ cannot be released into the natural environment[6,7]. After entering the environment, they will resemble other environmental pollutants and participate in the circulation of the biosphere, where complex migration and transformation processes occur, which will produce ecological effects. For example, Yamamoto *et al.* found that $nTiO_2$ increases the generation of reactive oxygen species in skin cells[8], which may damage DNA or mutation of the gene and eventually develop to cellular cancer[9,10]. It was found that the nanoparticles affect the properties of the particles themselves. Particle size, surface potential, ion species, ion concentration, and pH values all affect the aggregation and settling of nanoparticles in water, hence their reactivity and biotoxicity. Therefore, studying the sedimentation capacity of $nTiO_2$ in water bodies can

provide important theoretical support for assessing the potential ecological risk of $nTiO_2$.

At present, the global economy is developing rapidly, and science and technology are becoming more and more developed. In agricultural production, a large number of pesticides and fertilizers containing ammonia nitrogen are being used, and the phenomenon of ammonia nitrogen pollution in lakes, groundwater and rivers has become more and more serious. Therefore, preventing and controlling ammonia nitrogen pollution is an urgent task in Chinese agricultural science, and it is of great practical significance to study the harm of ammonia nitrogen pollution. For example, the fixation of phosphorus in soil was studied by Li Yanan *et al.* in the case of synthetic calcium magnesium carbonate, and high pH favored fixation of phosphorus by the material[11]. At the same time, Na^+ is one of the most widely distributed and abundant ions in groundwater, which is inevitably considered when studying the relevant water environment.

It has been shown that $nTiO_2$ can be used to remove ammonia nitrogen from sewage[12,13]. After entering the water environment, $nTiO_2$ causes aggregation and settlement under van der Waals force and electrostatic attraction, which may lead to short stay in water, but also reduce the specific surface area of the particles, affect $nTiO_2$ reactivity, reduce photocatalytic performance, and ultimately affect the ability of $nTiO_2$ to remove ammonia nitrogen. So far, most reports have been on the effect of $nTiO_2$ migration. For example, Liu Cheng *et al.* studied the effect of phosphate on $nTiO_2$ migration in soil[14], and Xu Xiaoting *et al.* studied the effect of phosphate and humic acid on $nTiO_2$ migration[15]. However, to date, no report has been reported on the impact of ammonia nitrogen on $nTiO_2$ settlement performance, so it is very important to study the aggregation and settlement capacity of $nTiO_2$ in water bodies containing ammonia nitrogen.

In view of this, the authors mainly studied the mechanism of NH^{4+} on $nTiO_2$ particle settlement, studied the settlement curve of pH values, calculated the settlement rate through Zeta potential and nanopularity, and then explained the influence and mechanism of NH^{4+} on the settlement rate of $nTiO_2$ particles in water bodies.

2. Materials and methods

2.1 Experimental reagents

$nTiO_2$ was purchased from Shanghai Gaoquan Chemical Co., Ltd. All other reagents were analytical reagents (AR).

2.2 Aggregation experiment of $nTiO_2$

Accurately measure 1 g of TiO_2, transfer it to a 100 ml beaker, add 100 ml NH_4Cl solution and NaCl solution with different concentrations (1, 5 and 10 $mmol \cdot L^{-1}$) respectively, adjust the pH value to 6.0 and 8.0 with HCl and NaOH respectively, place the TiO_2 suspension in the ultrasonic instrument for ultrasonic for 30 min, and then stand for interval sampling, sampling 2 ml each time. The measurement method of $nTiO_2$ was measured by diantipyrylmethane method, and the absorbance was measured at 390 nm by Shimadzu uv-2450 UV spectrophotometer[16]. Dilute 1000 $mg \cdot L^{-1}$ titanium standard solution to 1–5 $mg \cdot L^{-1}$ for measurement, and obtain the standard curve of $nTiO_2$ concentration (as shown in **Figure 1**).

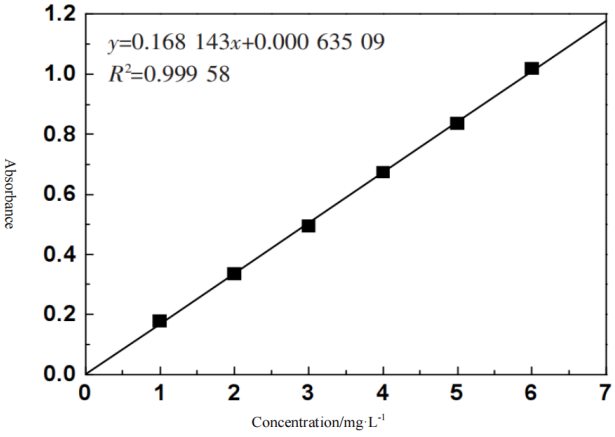

Figure 1. Curve for $nTiO_2$ concentration was determined by UV spectrophotometry.

2.3 The Zeta potential and hydraulical diameter measurements of $nTiO_2$

Accurately weigh 0.01 g of TiO_2, transfer it to a 100 ml beaker, add 100 ml of NH_4Cl solution and NaCl solution with different concentrations (1, 5 and

10 mmol·L^{-1}) respectively, and adjust the pH to 6.0 and 8.0 with HCl and NaOH respectively. Referring to the research method of Fang *et al.*[17], in order to promote the better dispersion of $nTiO_2$ in the solution, the suspension was placed in the ultrasonic instrument for ultrasonic for 10 min, and then each sample was sampled three times. The zeta potential and hydraulic diameter were measured by Malvin Nano-ZS90, and finally the average value was taken.

2.4 Settlement efficiency model

The sedimentation data were analyzed using the empirical model of Quik *et al.* and Velzeboer *et al.*[18,19]:

$$C_t = C_{res} + (C_0 - C_{res}) \times e^{-t \times V_s / h} \quad (1)$$

in which t is the settlement time, C_t is the colloidal concentration (g·L^{-1}) at the time t, Cres is the residual concentration (g·L^{-1}), C_0 is the initial concentration (g·L^{-1}), V_s is the sedimentation rate (mm·min^{-1}), h is the height of the water surface distance sampling point, aggregate V_s. According to equation (1), assuming not in each solution, the $nTiO_2$ samples were dissolved in ionic states.

3. Results and discussion

3.1 Zeta potential and hydroechanical diameter of $nTiO_2$ in NaCl solution

In **Figure 2**, it studied the Zeta potential (a) and hydroechanical diameter (b) of $nTiO_2$ at pH = 6.0 and 8.0, in NaCl solution.

In **Figures 2(a)** and **2(b)**, the Zeta potential becomes slightly less negative with Na^+ concentration, with particle size (hydroechanical diameter) larger and prone to reunion. When the pH value continues to increase to 8.0, the Zeta potential of $nTiO_2$ in the water environment becomes more negative and the hydraulical diameter decreases. For specific pH values, both Zeta potentials become less negative with increasing Na^+ concentration, mainly because the charge shielding effect and electrostatic bielectric layer on the $nTiO_2$ surface are compressed resulting in reduced net negative charge and reduced Zeta potention the particle surface[20,21].

3.2 Zeta potential and hydroechanical diameter of $nTiO_2$ in NH_4Cl solution

In **Figure 3**, it studied The Zeta potential (a) and hydroechanical diameter (b) of $nTiO_2$ at pH = 6.0, were studied in NH_4Cl solution 8.0.

In **Figure 3(a)**, the Zeta potentials of $nTiO_2$ at pH = 6.0 and 8.0 are all negative. At the same NH_4Cl concentration, the Zeta potential at pH = 6.0 is less negative than that at pH = 8.0; in **Figure 3(b)**, at the same NH_4Cl concentration, the particle size of $nTiO_2$ decreases with increasing pH values. The possible mechanism leading to this phenomenon is that, Zeta, with less than a negative potential. This results in a smaller electrostatic repulsion between the $nTiO_2$ particles, making it easier to reunite between $nTiO_2$ particles and then leading to a larger particle size. In **Figure 3(a)**, the Zeta potential of $nTiO_2$ becomes less negative with increasing ion concentrations for spe-

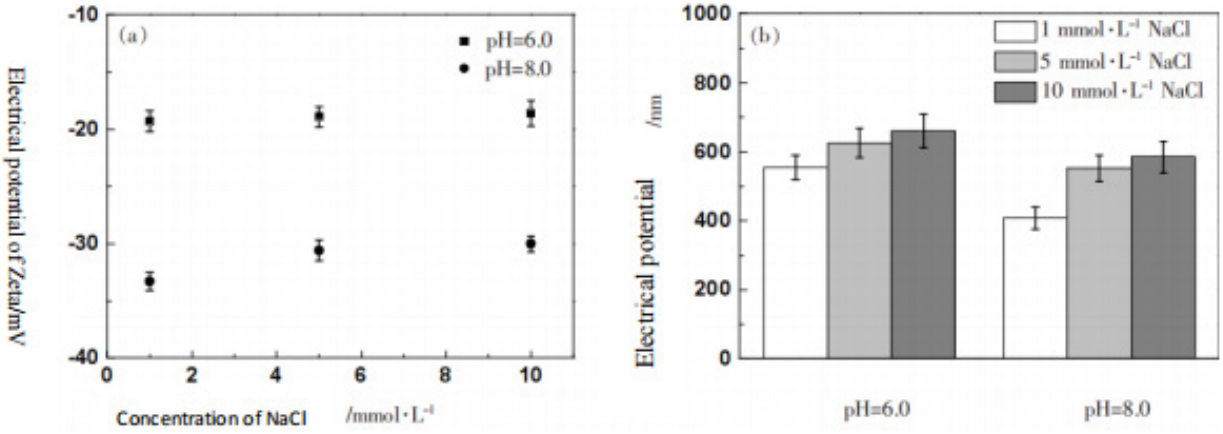

Figure 2. Zeta potentials **(a)** and Hydraulical diameter **(b)** of $nTiO_2$ in different concentrations of NaCl solution under pH= 6.0 and 8.0.

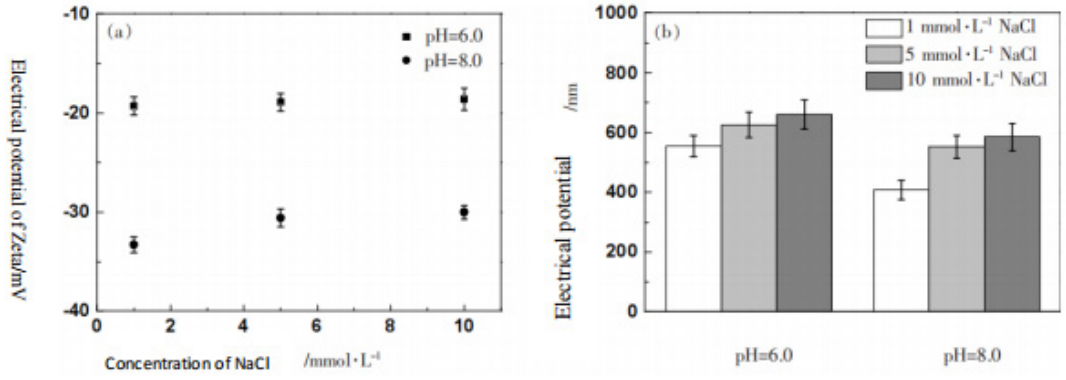

Figure 3. Zeta potentials **(a)** and Hydraulical diameter **(b)** of $nTiO_2$ in different concentrations of NH_4Cl solution under pH = 6.0, and 8.0.

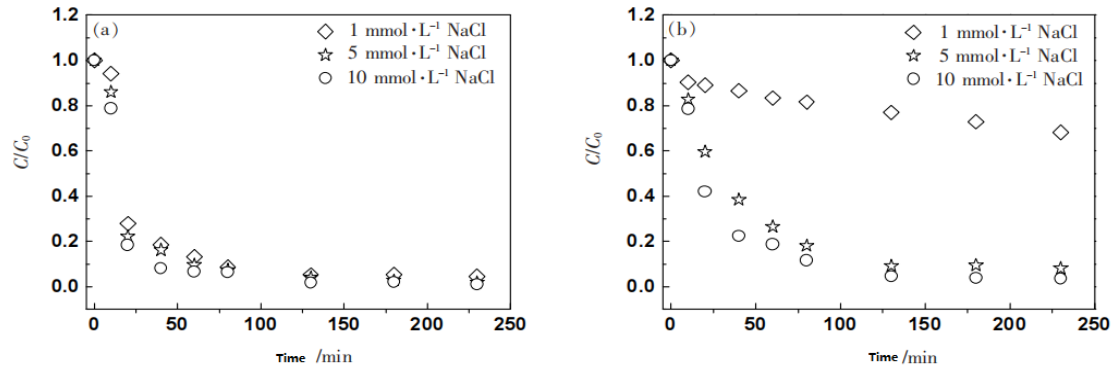

Figure 4. Settlement curves of $nTiO_2$ in different concentrations of NaCl solution pH = 6.0 (a) and 8.0 (b).

cific pH values, consistent with the phenomenon in Na^+. The increase in the hydrotomechanical diameter in **Figure 3(b)** is consistent with the less negative of the Zeta potential in **Figure 3(a)**. Compared to **Figures 3** and **2**, the Zeta potential of $nTiO_2$ is more negative and smaller particle size in NH_4Cl electrolyte solution at the same pH values and the same ion concentration. For example, under the condition of pH = 6.0, the Zeta potential and hydroechanical diameter of $nTiO_2$ in 1 mmol·L^{-1} NaCl solution are –19.3 mV, 554 nm, and the corresponding value becomes -20.6 mV, 472 nm. When the electrolyte solution is 1 mmol·L^{-1} NH_4Cl, the corresponding values are changed to –20.6 mV, 472 nm.

3.3 Settlement of $nTiO_2$ in the NaCl solution

Figure 4 is the settlement curve of $nTiO_2$ in NaCl solution in pH = 6.0 and 8.0.

The abscissa represents the settling time, and the ordinate represents the ratio of the concentration of $nTio_2$ (c) in the sampled liquid to the initial concentration of $nTio_2$ (C_0) under the corresponding settling time. The smaller the ratio, the lower the concentration of $nTiO_2$ in the representative sample, and the more $nTiO_2$ settled in the corresponding solution. **Figure 4(a)** shows that under the condition of pH = 6.0, although the concentration of NaCl solution has no obvious effect on the sedimentation performance of $nTiO_2$, on the whole, the higher the ion concentration, the faster the sedimentation rate and the worse the suspension stability. The increase of ion concentration is conducive to the sedimentation of particles, but this effect is not very obvious. According to the sedimentation rate (V_s) simulated and calculated according to formula (1), it is found that with the increase of ion concentration, V_s only increases from 0.507 mm·min^{-1} to 0.534 mm·min^{-1}. In **Figure 4(b)**, under the condition of pH = 8.0, low NaCl concentration (1 mmol·L^{-1}) has obvious sedimentation effect on $nTiO_2$, which significantly enhances the suspension stability of $nTiO_2$ in water environment. Comparing **Figure 4(a)** and **Figure 4(b)**, under the condition of 1 mmol·L^{-1} NaCl, pH

value is an important factor affecting the sedimentation performance of $nTiO_2$ in water environment; at higher ion concentration, the inhibition effect of high pH value on sedimentation is not obvious.

3.4 Settlement of $nTiO_2$ in the NH_4Cl solution

As shown in **Figure 5(a)**, $nTiO_2$ settles at pH = 6.0 with increasing NH^{4+} concentration, indicating that $nTiO_2$ sedimentation performance is affected by NH^{4+} concentration, and higher sedimentation rate and worse suspension stability, mainly due to the charge shielding effect of the $nTiO_2$ surface and electrostatic double electric layer compression theory, and enhanced electrostatic repulsion between particles[19,20].When the pH value increased to 8.0, the suspension stability of $nTiO_2$ still weakened with increasing NH^{4+} concentration. The data in **Table 1** explain this well: it does increase with ion concentration. This suggests that NH^{4+} concentration is an important factor influencing the settling properties of $nTiO_2$. By comparing **Figures 5(a)** and **5(b)**, we also found that when the pH increases at the same NH^{4+} concentration, the smaller the settlement rate, the better the suspension stability. This is consistent with previous Zeta potential and hydroechanical diameter results: the Zeta potential of $nTiO_2$ is more negative and smaller hydraulical diameter at high pH. Moreover, the data in **Table 1** indicate values at pH = 6.0 higher than those at pH = 8.0, indicating that increased high pH improves the suspension stability of $nTiO_2$ in the water environment. Comparing **Figures 4(a)** and **5(a)**, it is not difficult to find that NH^{4+} inhibited the aggregate deposition of $nTiO_2$ compared to Na^{+} under the same ionic strength at pH = 6.0. If settlement equilibrium is reached, the value of C/C_0 is 0.029 in 10 mmol·L^{-1} NaCl solution, and the ratio is 0.011 in NaCl solution. This phenomenon still applies when pH increases to 8.0. The Zeta potential and hydraulical diameters in **Figures 2** and **3** also show that a more negative Zeta potential and a smaller hydraulical diameter will make the nanoparticles difficult to settle and enhance stability. It can be seen that NH^{4+} is conducive to improve the suspension stability of $nTiO_2$ in the water environment.

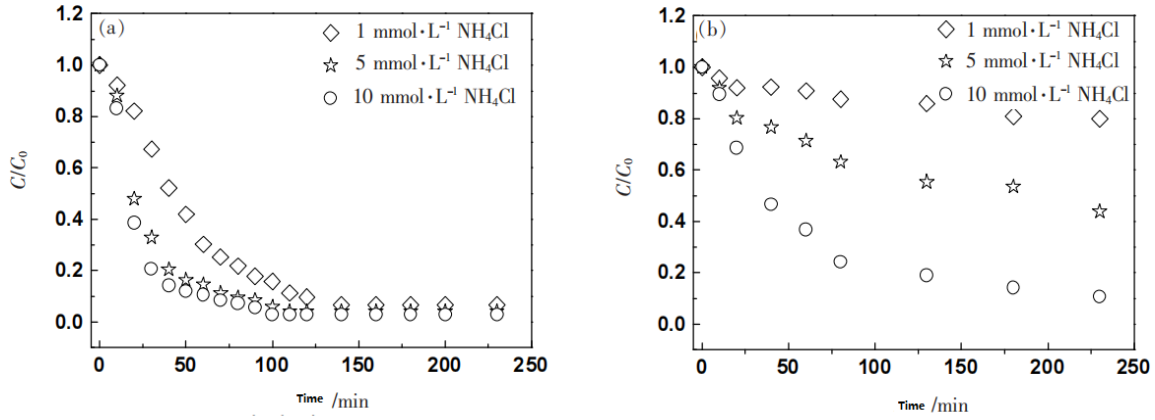

Figure 5. Settlement curve of $nTiO_2$ at pH = 6.0 **(a)** and 8.0 **(b)** in different concentrations of NH_4Cl solution.

Table 1. Settlement rates of $nTiO_2$ (10 g·L^{-1}) in different electrolyte solutions

PH of solution	Concentration of NH_4Cl /mmol·L^{-1}	Settlement rate V_s / mm·min^{-1}	PH of solution	Concentration of NaCl /mmol·L^{-1}	Settlement rate V_s / mm·min^{-1}
6.0	1	0.570	6.0	1	0.507
	5	0.688		5	0.524
	10	0.782		10	0.534
0.4598.0	1	0.142	8.0	1	0.214
	5	0.196		5	0.459
	10	0.363		10	0.466

4. Conclusion

Experimental results show that high pH helps to improve $nTiO_2$ stability in the electrolyte solution because the increased pH leads to more negative particle surface potential, larger electrostatic repulsion between particles, causing particles to reunite and eventually lead to settle. In the same pH and ionic strength, NH^{4+} in water than Na^{+} can improve particle stability and suspension, and the settlement rate of $nTiO_2$ increases with NH^{4+} concentration.

Conflict of interest

The authors declare that they have no conflict of interest.

Acknowledgements

This paper was supported by the National Natural Science Foundation (21777110).

References

1. Wang H, Zhao W, Fang Y, *et al.* Study on the photocatalytic killing of tumor cells by titanium dioxide. Chinese Journal of Catalysis 1999; 20(3): 373–374.
2. Yu B, Wu H, Zhang W. Application of photocatalytic nanomaterials in Environmental Protection (in Chinese). Petrochemical Industry 2005; 34(5): 491–495.
3. Kim SA, Kamala-Kanana S, Lee KJ, *et al.* Removal of Pb(II) from aqueous solution by a zeolite-nanoscale zero-valent iron composite. Chemical Engineering Journal 2013; 217: 54–60.
4. Wang C, Li M, Li H. Field electron emission properties of ordered array membranes of highly oriented carbon nanotubes (in Chinese). Scientia Sinica (Mathematica) (Series A) 2000; 30(11): 1019–1024.
5. Fujishima A, Rao TN, Tryk DA. Titanium dioxide photocatalysis. Journal of Photochemistry and Photobiology C: Photochemistry Reviews 2000; 1(1): 1–21.
6. Kiser MA, Westerhoff P, Benn T, *et al.* Titanium nanomaterial removal and release from wastewater treatment plants. Environmental Science & Technology 2009; 43(17): 6757–6763.
7. Robichaud CO, Uyar AE, Darby MR, *et al.* Estimates of upper bounds and trends in nano-TiO_2 production as a basis for exposure assessment. Environmental Science & Technology 2009; 43(12): 4227–4233.
8. Yamamoto A, Honma R, Sumita M, *et al.* Cytotoxicity evaluation of ceramic particles of different sizes and shapes. Journal of Biomedical Materials Research Part A 2004; 68A(2): 244–256.
9. Dunford R, Cai L, Serpone N, *et al.* Chemical oxidation and DNA damage catalysed by inorganic sunscreen ingredients. FEBS Letters 1997; 418(1-2): 87–90.
10. Subrahmanyam A, Arokiadoss T, Ramesh T P. Studies on the oxygenation of human blood by photocatalytic action. Artificial Organs 2007; 31(11): 819–825.
11. Li Y, Chen M, Xu T, *et al.* Immobilization of phosphorus in soils with the synthesized magnesium calcium carbonate. Journal of Suzhou University of Science and Technology (Natural Science Edition) 2015; 32(4): 35–39.
12. Zhang M, Tang W, Zhang W, *et al.* Photocatalytic properties of nano TiO_2 on the ammonia nitrogen at low content. Technology of Water Treatment 2016; 42(7): 65–69.
13. Chen X, Liu L, Yang F, *et al.* Removing ammonia nitrogen from water using CdS/TiO_2 photocatalysis. Photographic Science and Photochemistry 2007; 25(2): 89–101.
14. Liu C, Sun Q, Zhang G, *et al.* Influence of phosphate on the transport of $nTiO_2$ in soil column. Journal of Suzhou University of Science and Technology (Natural Science Edition) 2018; 36(3): 44–50.
15. Xu X, Wang C, Xu N. Effect of humic acid and phosphate on the transport of titania nanoparticles. Journal of Suzhou University of Science and Technology (Natural Science Edition) 2017; 35(4): 42–46.
16. Feng G, Xu N, Li Z, *et al.* Influence of flow rate on the transport of $nTiO_2$ and phosphate and its modeling. Journal of Suzhou University of Science and Technology (Natural Science Edition) 2018; 36(1): 56–61.
17. Fang J, Xu M, Wang D, *et al.* Modeling the transport of TiO_2 nanoparticle aggregates in saturated and unsaturated granular media: effects of ionic strength and pH. Water Research 2013; 47(3): 1399–1408.
18. Quik JTK, Stuart MC, Wouterse M, *et al.* Natural

colloids are the dominant factor in the sedimentation of nanoparticles. Environmental Toxicology and Chemistry 2012; 31(5): 1019–1022.
19. Veleber I, Quik JTK, Dik VDM, *et al.* Rapid settling of nanoparticles due to heteroaggregation with suspended sediment. Environmental Toxicology and Chemistry 2014; 33(8): 1766–1773.
20. Elimelech M, Gergory J, Jia X, *et al.* Particle deposition and aggregation: Measurement modeling and simulation. Woburn: Buaer Worth Heinemann; 1995.
21. Hunter RJ. Foundations of colloid science. New York: Oxford University Press; 1987.

Characterization and Application of Nanomaterials (2021) Volume 4 Issue 2
doi:10.24294/can.v4i2.1324

ORIGINAL RESEARCH ARTICLE

Research progress of nanoarray structure transport layers in perovskite solar cells

Fangxin Tan[1], Shan Cong[1*], Qinghua Yi[1], Zhida Han[1,2], Yushen Liu[1]

[1] *School of Electronic and Information Engineering, Changshu Institute of Technology, Changshu 215500, China. E-mail: congshan@cslg.edu.cn*

[2] *Jiangsu Laboratory of Advanced Functional Materials, Changshu Institute of Technology, Changshu 215500, China*

ABSTRACT

The electron/hole transport layer can promote charge transfer and improve device performance, which is used in perovskite solar cells. The nanoarray structure transport layers can not only further promote carrier transport but also reduce recombination. It also has a great potential in enhancing perovskite light absorption, improving device stability and inhibiting the crack nucleation of different structure layers in perovskite solar cells. This paper reviewed the research progress of perovskite solar cells with different nanoarray structure transport layers. The challenges and development directions of perovskite solar cells based on nanoarray structure transport layers are also summarized and prospected.

Keywords: Perovskite Solar Cells; Nanoarray; Transport Layers

ARTICLE INFO

Received: 5 July 2021
Accepted: 29 August 2021
Available online: 5 Septemper 2021

1. Introduction

Organic-inorganic hybrid perovskite materials have attracted much attention because of their adjustable bandgap, long carrier diffusion length and high light absorption coefficient. They are the preferred materials for solar cells prepared by the low-temperature solution method[1,2]. At present, the certified conversion efficiency of perovskite solar cells (PSC) has exceeded 25%[3]. Conventional perovskite solar cells mainly include planar perovskite solar cells and mesoporous perovskite solar cells. The electron/hole transport layer can accelerate the electron/hole transport in the device and reduce the interface recombination, which plays an important role in improving the efficiency and stability of the device.

At present, various organic and inorganic materials are widely used in perovskite solar cells, such as 2,2', 7,7' -Tetra [N, N-bis (4-methoxyphenyl) amino]-9,9'-Spiro-OMeTAD, poly [bis (4-phenyl) (2,4,6-trimethylphenyl) amine] (PTAA), titanium oxide (TiO_2), zinc oxide (ZnO), tin oxide (SnO_2), nickel oxide NiO, and so on[4–7]. the researchers found that the transport layer of nanoarray structure ,such as titanium oxide nanorodarray, zinc oxide nanoarray, not only could promote charge transmission but also reduce interface recombination. It also could enhance perovskite light absorption, inhibit crack nucleation of different structural layers in perovskite solar cells, and improve the stability of flexible devices[8–10]. This paper introduces the research progress at home and abroad, which includes the design and prepara-

tion of nanoarray structures of different electron and hole transport layer materials.

2. Research progress of nanoarray electron transport layer

2.1 Metal oxide nanoarrays

The electron transport layer materials of a metal oxide represented by TiO_2, ZnO, and SnO_2, are widely used in perovskite solar cells, photodetectors and other optoelectronic devices with their excellent electron transport capacity, relatively good environmental stability and convenient preparation process[11–14].

2.1.1 Titanium oxide TiO_2

TiO_2 is easy to prepare, low-cost, with appropriate energy level and electron transport capacity. PSC use TiO_2 as an electron transport layer material widely. At present, the research on TiO_2 nanoarray mainly focuses on the preparation method and structural composition to optimize its performance and structure. It improve electron transport efficiency using TiO_2 nanoarray, reduces interfacial recombination, enhances the light absorption of photoactive layer, playing a good role in improving the stability of the device.

Kim *et al.* reported an efficient perovskite solar cell using submicron (~0.6 μm) rutile TiO_2[15]. TiO_2 nanorods were grown by hydrothermal method, and the reaction time adjusted the length of nanorods. Experiments showed that the current density would decrease due to the increase of nanorods. It is mainly due to the tilt of the nanorods during the growth process, which affects the filling of perovskite and ultimately affects the device efficiency (**Figure 1**).

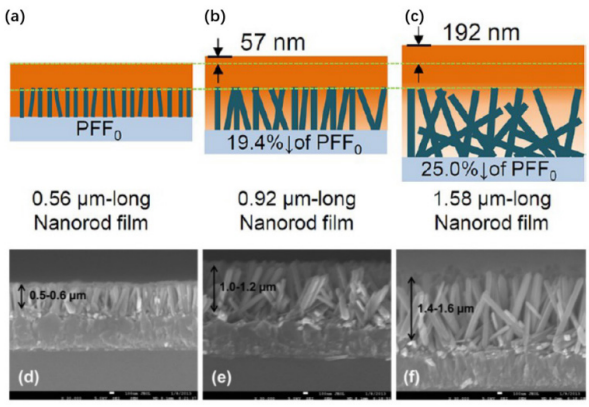

(a) ~ **(c)** effect of different TiO_2 nano array height on device performance; **(d)** ~ **(f)** scanning electron microscope images of different TiO_2 nano array heights[15].

Figure 1. Application of TiO_2 nanoarray.

Huh *et al.* enhanced the performance of PSC by selectively growing TiO_2 nanorods[16]. They selectively grew TiO_2 nanorod substrate by nanoimprint lithography and hydrothermal growth method. Experiments show that TiO_2 nanorods, as an electron transmission channel, can effectively improve the electron-hole separation energy, reduce interface recombination, and obtain an open circuit voltage of 1.12 V. In addition, TiO_2 nanorods can increase the optical path of the incident light, enhance the light absorption of the active layer and improve the device performance.

Hu *et al.* prepared a TiO_2 nano column array by grazing angle deposition[17]. Scanning electron microscope studied The TiO_2 nano column array, scanning near-field optical microscope, and UV-Vis absorption. It found that the TiO_2 nano column transport layer can enhance the optical absorption of perovskite through a large number of precursor penetration paths, near-field light concentration, and partial UV shielding. Thus it improves the short circuit current and stability of the device.

Liu *et al.* deposited the optimized CdS shell on TiO_2 nanoarray at room temperature by a simple chemical bath method, which significantly improved the efficiency and stability of PSCs[18]. Experiments show that, on the one hand, the CdS shell can passivate oxygen vacancies on the TiO_2 surface, prevent electron-hole recombination and protect the calcium titanium layer. On the other hand, the insertion of Cds shell on the surface of TiO_2 is helpful to form a type-II structure, which can further accelerate electron transfer and the Cds@TiO_2 coaxial nanoarray structure provides enough space for perovskite implantation. Xiao *et al.* successfully doped Nb in titanium oxide array by hydrothermal method[19]. The research shows that in the interface between TiO_2 and perovskite, TiO_2 doped with Nb is more efficient for electron transport and charge separation, which

provides an effective way to prepare PSCs with high performance and high stability.

2.1.2 Zinc oxide ZnO

Similar to TiO_2, ZnO is also a common electron transport material in perovskite solar cells. Its electron mobility is higher than TiO_2, and it is more controllable jn form and has a lower synthesis temperature. These advantages make it widely used in PSC[20,21]. At present, the research on ZnO nanoarrays mainly focuses on many ways, such as how to improve preparation methods,interface modification, increase perovskite filling, reduce carrier recombination as well as improve device efficiency.

Tulus *et al.* Deposited gold nanoparticles on the surface of ZnO nanorod array using vacuum deposition technology to increase the hole Schottky barrier at the interface of ZnO perovskite active layer, as shown in **Figure 2(a)**. Further block holes, passivate carrier composite defects on the surface of ZnO nanorods, reduce the loss of open-circuit voltage of devices, and improve the filling factor, thus, the conversion efficiency of the battery improved[22].

Dong *et al.* doped the ZnO nanorod array with Al and formed an Al-Zn-O layer on the surface of the ZnO nanorod. While passivating the surface defects of the ZnO nanorod, they also adjusted the energy level to make the energy level of the active layer better match that of the electron transport layer, improve the electron transport efficiency, and finally improve the device[23].

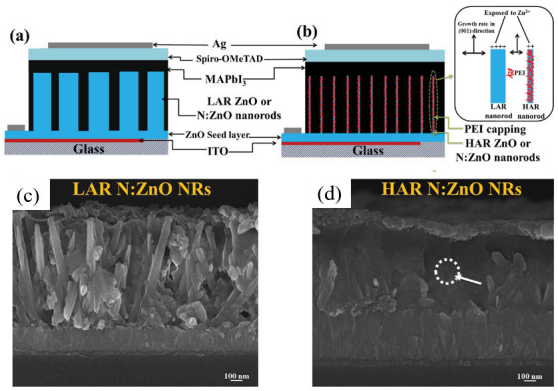

(a) device structure diagram of conventional low aspect ratio (LAR) ZnO nanoarrays and **(b)** high aspect ratio (HAR) ZnO nanoarrays with PEI coating (illustration: PEI as a capping agent for controlling nanotube growth); based on the scanning electron microscope cross-sectional images of 1,070 nm intact cells of LAR N: ZnO NRs **(c)** and HAR N: ZnO NRs **(d)** without PEI coating, the results show that HARZnO nanoarrays have better perovskite wetting properties[24].

Figure 2. Application of ZnO nanoarrays.

Mahmood *et al.* combined with the dual characteristics of polyethyleneimine (PEI) as dipole layer and selective polymer cover, prepared N: ZnO nanoarrays with high aspect ratio and electron-rich nitrogen doping through low-temperature solution-phase hydrothermal growth[24]. Then he applied them in PSC to effectively improve the penetration of calcium titanium ore in the array, inhibit carrier recombination and improve device efficiency (**Figure 2**). At the same time, they successfully applied PEI coating on the N: ZnO array adjusted the work function, and obtained stable and hysteresis-free devices with device efficiency > 16%.

More interestingly, Zhao *et al.* prepared highly ordered ZnO nanorod arrays at low temperatures (90°C)[25]. This nanoarray structure has excellent mechanical stability when combined with a flexible substrate, and its performance remains 90% after 1,000 bending cycles with a radius of curvature of 4 mm. It has excellent bending resistance and durability and has great application potential in foldable photovoltaic devices.

2.1.3 Stannic oxide SnO_2

In recent years, planar PSCs with SnO_2 ETLs have developed rapidly due to the excellent characteristics of SnO_2 materials, such as appropriate energy level, high electron mobility, good transmittance, excellent chemical stability, and inactive UV catalysis. Similar to zinc oxide, stannic oxide also faces many problems of morphology and defect states. Optimize the stannic oxide nanorod arrays using the same passivation strategy[26].

Song *et al.* doped SnO_2 nanocrystals with Y^{3+} by typical solvothermal method[27]. The results show that Y dopant has a more appropriate energy level structure and better carrier dynamics performance, and obtains devices with a total efficiency of 20.71%. Gao *et al.* proposed an effective in-situ template self-etching method on the basis of a series

of controllable experiments, stannic oxide nanotube arrays were prepared with zinc oxide nanorods as sacrificial templates, and the growth mechanism of nanotubes was studied[28]. By comparing stannic oxide nanotube array PSC devices with similar SnO_2 or ZnO PSCs, PSC with stannic oxide nanotube array as transport layer has better long-term stability and UV stability (**Figure 3**). This work emphasizes the importance of the material selection of an electron transport layer and provides an idea for realizing ideal electron transport layer/substrate homogeneous junction to promote electron transport.

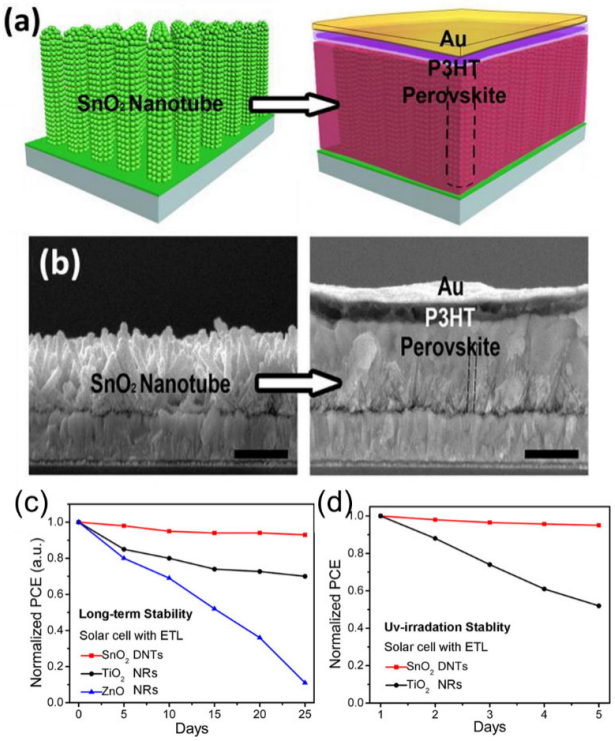

(a) schematic diagram based on SnO_2 nanoarray and its devices; **(b)** the corresponding scanning electron microscope cross-sectional image, with a scale of 500 nm; **(c)** comparison diagram of long-term stability based on SnO_2, TiO_2, and ZnO nanoarrays; **(d)** based on the UV stability comparison diagram of SnO_2 and TiO_2 nanoarray perovskite solar cells, the results show that SnO_2 nanoarray perovskite solar cells have better stability[28].

Figure 3. Application of SnO_2 nanoarray.

2.2 Other nanoarray electron transport materials

Through previous work, it finds that zinc compounds usually have excellent electrical properties. so it is also an important topic to develop the electron transport layer materials of zinc compound. Tavakoli *et al.* introduced Zn_2SnO_4 nanorod array as electron transport layer into perovskite solar cells, although the short-circuit current of the obtained devices increased and the hysteresis significantly reduced. However, the open-circuit voltage loss caused by energy level mismatch still needs to solve[29].

3. Research progress of hole transport layer of nanoarray

The hole transport materials commonly used in PSC mainly include organic materials and inorganic hole transport materials. These holes materials need to meet the conditions of good hole transport capacity, high stability, and matching with perovskite energy level. Organic hole transport materials, such as polyethylene dioxythiophene-poly(styrene sulfonate) (PEDOT: PSS), poly[bis (4-phenyl) (2,4,6-trimethylphenyl) amine] (PTAA), are of relatively complex synthesis, and it is not easy to prepare nanorod array structure. In addition, the acidity of PEDOT: PSS and the instability of unsaturated carbon bonds in organic materials are not conducive to the long-term stable operation of the device. The preparation process of inorganic hole transport materials, such as nickel oxide NiO, cuprous iodide CuI, cuprous thiocyanate CuSCN, is relatively simple and convenient structural regulation[30–32].

Gan *et al.* successfully synthesized CuSCN nanorod arrays with good crystallinity and electrical properties at room temperature by adjusting the synthesis temperature and deposition potential, which opened an opportunity for their application in the field of optoelectronic devices[33]. Xi *et al.* applied CuSCN nanowire array and its similar derived microstructure to perovskite solar cells to achieve a photoelectric conversion efficiency of more than 7.5%. At the same time, the research results show that the introduction of CuSCN nanowire array and its derived microstructure is conducive to obtaining a more regular perovskite active layer interface, improving the crystal orientation of perovskite and reducing crystal defects at the active layer and interface, reducing carrier recombination and improving device performance[34].

Anandan *et al.* introduced the wet prepared CuO nanorod array into the dye-sensitized solar cell and obtained a cell with 0.29% conversion efficiency, which proved that the CuO nanorod array could be used as the photoanode (hole transport layer) of the dye-sensitized solar cell. But the CuO band gap was small (about 1.2 eV), such natural defect makes it impossible to completely separate photogenerated electron-hole pairs, resulting in the recombination of a large number of carriers at the CuO interface, affecting the efficiency of the device and greatly limiting its application[35].

Cong *et al.* prepared well-crystallized nickel oxide nanorod arrays at room temperature by grazing angle deposition. It proved that the introduction of nickel oxide arrays reduced the reflection of the light incident surface, increased the light capture of the device, passivated the interface defects between the hole layer and the active layer, induced perovskite crystal growth, obtained high-quality perovskite films, and finally obtained more than 20% photoelectric conversion efficiency. At the same time, the advantages of low-temperature preparation make this structure also have a conversion efficiency of more than 17% on the flexible substrate. Moreover, due to the mesoporous structure of the array, the device stress is relieved and the stable operation of the devices on the flexible substrate is guaranteed, which proves the application potential of nanorod array in flexible devices[36] (**Figure 4**).

Zheng *et al.* introduced copper phthalocyanine (CuPc) nanorod arrays into organic solar cells. Through close engagement with PCBM molecules in the active layer, the dark current intensity of the device reduces, and the device performance is doubled compared with the device based on planar CuPc structure. It also shows that this structure can effectively passivate the defects between the active layer and the electrode[37]. Zhang shows that it can effectively replace the current mainstream Spiro-OMeTAD hole transport materials doped with a lithium salt, which integrates the undoped CuPc nanorod array with the electrode from the perspective of chemical stability. And obtain a battery with high repeatability with an efficiency of 16.1%[38].

4. Conclusion

This paper describes the application and research progress of nanoarray transport layer materials in PSC. Generally, these devices mainly focus on the preparation and optimization of oxide materials. The preparation methods are a popular such as hydrothermal method, vacuum deposition, template method. Generally, the devices with nanoarray transport layer materials can improve the carrier transport efficiency, and enhance the absorption of the photoactive layer. At present, most of the devices prepared by these materials are still small-area devices based on a glass substrate. There is still great potential in the preparation of flexible devices and large-area de-

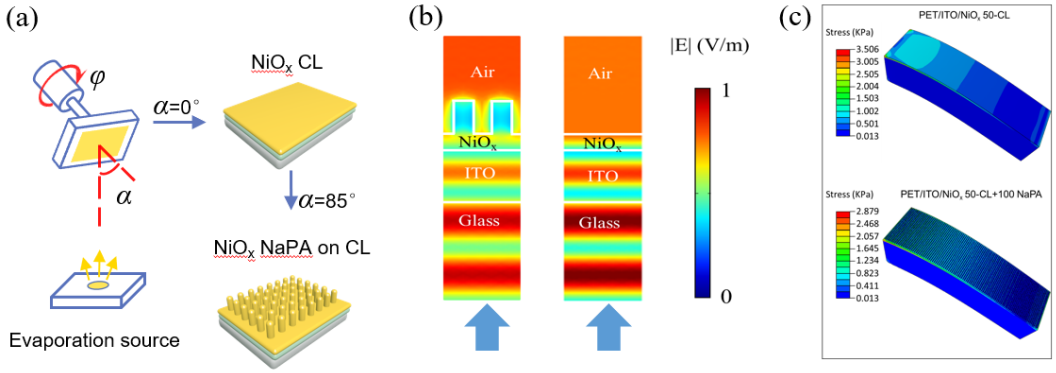

(a) grazing angle deposition of NiO nanoarrays; **(b)** the finite element analysis of the electric field distribution diagram with/without NiO nanoarray substrate. The results show that NiO nanoarray structure is conducive to increasing light transmission and reducing light reflection; **(c)** the finite element analysis stress distribution diagramof the flexible substrate with/without NiO nanoarray.The results show that the NiO nanoarray structure has better bending resistance[36].

Figure 4. Application of NiO nanoarrays.

vices. In the future, it is necessary to select appropriate flexible substrates for the high-quality growth of nanoarrays through interface modification or doping to improve the carrier mobility, reduce the carrier recombination, improve the device stability, and realize the preparation and application of flexible wearable devices.

Conflict of interest

The authors declare that they have no conflict of interest.

Acknowledgements

Project: The National Natural Science Foundation of China Project "Study on stability mechanism of perovskite solar cells based on NiO nano arrays" (62005027); Jiangsu Natural Science Foundation Project "Growth of efficient and stable TiO_2 array @(rGO/Cu_2O) heterojunction electrode by polymer assisted deposition and its photoelectrochemical hydrolysis mechanism" (BK20181037).

References

1. Kim HS, Lee CR, Im JH, *et al.* Lead iodide perovskite sensitized all-solid-state submicron thin film mesoscopic solar cell with efficiency exceeding 9%. Scientific Reports 2012; 2(1): 591.
2. Chen Q, Zhou H, Hong Z, *et al.* Planar heterojunction perovskite solar cells via vapor-assisted solution process. Journal of the American Chemical Society 2014; 136(2): 622–625.
3. Ma C, Park NG. A realistic methodology for 30% efficient perovskite solar cells. Chemistry 2020; 6(6): 1254–1264.
4. Kung PK, Li MH, Lin PY, *et al.* A review of inorganic hole transport materials for perovskite solar cells. Advanced Materials Interfaces 2018; 5(22): 1800882.
5. Shin SS, Suk JH, Kang BJ, *et al.* Energy-level engineering of the electron transporting layer for improving open-circuit voltage in dye and perovskite-based solar cells. Energy and Environmental Science 2019; (12): 958–964.
6. Tan B, Raga SR, Chesman ASR, *et al.* LiTFSI-free Spiro-OMeTAD-based perovskite solar cells with power conversion efficiencies exceeding 19%. Advanced Energy Materials 2019; 9(32): 1901519.1–1901519.10.
7. Tang G, You P, Tsi Q, *et al.* Solution-phase epitaxial growth of perovskite films on 2D material flakes for high-performance solar cells. Advanced Materials 2019; 31(24): e1807689.
8. Huh D, Oh KS, Kim M, *et al.* Selectively patterned TiO_2 nanorods as electron transport pathway for high performance perovskite solar cells. Nano Research 2019; 12(3): 601–606.
9. Lv Y, Wang P, Cai B, *et al.* Facile fabrication of SnO_2 nanorod arrays films as electron transporting layer for perovskite solar cells. Solar RRL 2018; 2(9): 1800133.
10. Sun J, Hua Q, Zhou R, *et al.* Piezo-phototronic effect enhanced efficient flexible perovskite solar cells. ACS Nano 2019; 13(4): 4507–4513.
11. Boro B, Gogoi, B, Rajbongshi, BM, *et al.* Nano-structured TiO_2/ZnO nanocomposite for dye-sensitized solar cells application: A review. Renewable and Sustainable Energy Reviews 2018; 81(2): 2264–2270.
12. Zhang P, Wu J, Zhang T, *et al.* Perovskite solar cells with ZnO electron-transporting materials. Advanced Materials 2018; 30(3): 1703737.
13. Jiang Q, Zhang X, You J. SnO_2: A wonderful electron transport layer for perovskite solar cells. Small 2018; 14(31): 1801154-1–1801154-14.
14. Seo JY, Uchida R, Kim HS, *et al.* Boosting the efficiency of perovskite solar cells with CsBr-modified mesoporous TiO_2 beads as electron-selective contact. Advanced Functional Materials 2018; 28(15): 1705763.
15. Kim HS, Lee JW, Yantrar N, *et al.* High efficiency solid-state sensitized solar cell-based on submicrometer rutile TiO_2 nanorod and $CH_3NH_3PbI_3$ perovskite sensitizer. Nano Letters 2013; 13(6): 2412–2417.
16. Huh D, Oh K, Kim M, *et al.* Selectively patterned TiO_2 nanorods as electron transport pathway for high performance perovskite solar cells. Nano Research 2019; 12(3): 601–606.
17. Hu Z, García-Martín JM, Li Y, *et al.* TiO_2 nanocolumn arrays for more efficient and stable perovskite solar cells. ACS Applied Materials & Interfaces

2020; 12(5): 5979–5989.
18. Liu W, Chu L, Liu N, *et al.* Simultaneously enhanced efficiency and stability of perovskite solar cells with TiO_2@CdS core-shell nanorods electron transport layer. Advanced Materials Interfaces 2019; 6(5): 1801976.
19. Xiao G, Shiu C, Lv K, *et al.* Nb-doping TiO_2 electron transporting layer for efficient perovskite solar cells. ACS Applied Materials & Interfaces 2018; 1(6): 2576−2581.
20. Bi D, Boschloo G, Schwarzmüller S, *et al.* Efficient and stable CH3NH3PbI3-sensitized ZnO nanorod array solid-state solar cells. Nanoscale 2013; 5(23): 11686–11691.
21. Liu D, Wang Y, She Z, *et al.* Suppressed decomposition of perovskite film on ZnO via a self-assembly monolayer of methoxysilane. Sol RRL 2018; 2(12): 1800240.
22. Tulus, Olthof S, Marszalek M, *et al.* Control of surface defects in ZnO nanorod arrays with thermally-deposited au nanoparticles for perovskite photovoltaics. ACS Applied Energy Materials 2019; 2(5): 3736–3748.
23. Dong J, Zhao Y, Shi J, *et al.* Impressive enhancement in the cell performance of ZnO nanorod-based perovskite solar cells with Al-doped ZnO interfacial modification. Chemical Communications 2014; 50(87): 13381–13384.
24. Mahmood K, Swain BS, Amassian A. 16.1% efficient hysteresis-free mesostructured perovskite solar cells based on synergistically improved ZnO nanorod arrays. Advanced Energy Materials 2015; 5(17): 1500568.
25. Zhao X, She H, Sun R, *et al.* Bending durable and recyclable mesostructured perovskite solar cells based on superaligned ZnO nanorod electrode. Sol RRL 2018; 2(5): 1700194.
26. Liu D, Wang Y, Xu H, *et al.* SnO_2-based perovskite solar cells: Configuration design and performance improvement. Sol RRL 2019; 3(2): 1800292.
27. Song J, Zhang W, Wang D, *et al.* Colloidal synthesis of Y-doped SnO_2 nanocrystals for efficient and slight hysteresis planarsperovskite solar cells. Solar Energy 2019; 185: 508–515.
28. Gao C, Yuan S, Cao B, *et al.* SnO_2 nanotube arrays grown via an in situ template-etching strategy for effective and stable perovskite solar cells. Chemical Engineering Journal 2017; 325: 378–385.
29. Tavakoli MM, Prochowicz D, Yadav P, *et al.* Zinc stannate nanorod as an electron transporting layer for highly efficient and hysteresis-less perovskite solar cells. Engineered Science 2018; 3: 48–53.
30. Pattanasattayavong P, Yaacobi-Gross N, Zhao K, *et al.* Hole-transporting transistors and circuits based on the transparent inorganic semiconductor copper (I) thiocyanate (CuSCN) processed from solution at room temperature. Advanced Materials 2013; 25(10): 1504–1509.
31. Truong NTN, Hoang HHT, Park C. Improvement of vacuum free hybrid photovoltaic performance based on a well-aligned ZnO nanorod and WO_3 as a carrier transport layer. Materials 2019; 12(9): 1490.
32. Boix PP, Larramona G, Jacob A, *et al.* Hole transport and recombination in all-solid Sb2S3-sensitized TiO_2 solar cells using CuSCN as hole transporter. Journal of Physical Chemistry C 2011; 116(1): 1579–1587.
33. Gan X, Liu K, Du X, *et al.* Bath temperature and deposition potential dependences of CuSCN nanorod arrays prepared by electrochemical deposition. Journal of Materials Science 2015; 50(24): 7866–7874.
34. Xi Q, Gao G, Zhou H, *et al.* Highly efficient inverted solar cells based on perovskite grown nanostructures mediated by CuSCN. Nanoscale 2017; 9(18): 6136–6144.
35. Anandan S, Wen X, Yang S. Room temperature growth of CuO nanorod arrays on copper and their application as a cathode in dye-sensitized solar cells. Materials Chemistry and Physics 2005; 93(1): 35–40.
36. Cong S, Zou G, Lou Y, *et al.* Fabrication of nickel oxide nanopillar arrays on flexible electrodes for highly efficient perovskite solar cells. Nano Letters 2019; 19(6): 3676–3683.
37. Zheng Y, Bekele R, Ouyang J, *et al.* Organic photovoltaic cells with vertically aligned crystalline molecular nanorods. Organic Electronics 2009; 10(8): 1621–1625.
38. Zhang F, Yang X, Cheng M, *et al.* Boosting the efficiency and the stability of low cost perovskite solar cells by using CuPc nanorods as hole transport material and carbon as counter electrode. Nano Energy 2016; 20: 108–116.

Characterization and Application of Nanomaterials (2021) Volume 4 Issue 2
doi:10.24294/can.v4i2.1335

ORIGINAL RESEARCH ARTICLE

Defocused image restoration method based on micro-nano scale

Yongjun Liu[1,2*], Qiuyu Wu[1], Mingxin Zhang[1], Yi Wang[2]

[1] *School of Computer Science and Engineering, Changshu Institute of Technology, Changshu 215500, China. E-mail: yongjun1981@126.com*

[2] *School of Computer Science and Engineering, Northeastern University, Shenyang 110819, China*

ABSTRACT

An image adaptive noise reduction enhancement algorithm based on NSCT is proposed to perform image restoration preprocessing on the defocused image obtained under the microscope. Defocused images acquired under micro-nano scale optical microscopy, usually with inconspicuous details, edges and contours, affect the accuracy of subsequent observation tasks. Due to its multi-scale and multi-directionality, the NSCT transform has superior transform functions and can obtain more textures and edges of images. Combined with the characteristics of micro-nanoscale optical defocus images, the NSCT inverse transform is performed on all sub-bands to reconstruct the image. Finally, the experimental results of the standard 500 nm scale grid, conductive probe and triangular probe show that the proposed algorithm has a better image enhancement effect and significantly improves the quality of out-of-focus images.

Keywords: Micro-nano Scale; Defocused Image; NSCT; Image Restoration

ARTICLE INFO

Received: 27 July 2021
Accepted: 17 September 2021
Available online: 24 September 2021

1. Introduction

When observing samples with optical microscope, there is a problem of "Abbe limit" due to the limitation of diffraction limit[1,2]. When the observation scale reaches the micro-nano level, the observed images show fuzzy circular spots no matter how to adjust the focal length. Therefore, the images collected under micro-nano optical microscope have poor resolution, and unclear edges, details and contours not only affect the quality of the image, but also are not conducive to the subsequent observation of "depth" and other information[3].

Traditional image enhancement and preprocessing methods include histogram equalization algorithm[4], Retinex algorithm[5,6], homomorphic filtering algorithm[7], wavelet transform algorithm[8], etc., which have made great progress in recent years[4–8]. However, they have their own advantages and disadvantages, such as serious block effect and relatively complex operation in local equalization algorithm. Global equalization algorithm is also easy to cause color distortion due to over fitting. Retinex algorithm is based on color constancy. Homomorphic filtering algorithm needs to select reasonable filter parameters in frequency domain to realize image enhancement, but it is very difficult to select appropriate parameters.

For the defocus image collected under the microscope, we hope to avoid adding new noise as much as possible and make the enhanced image quality better. Non-subsampled Contourlet transform (NSCT)

has superior transformation function due to multi-scale and multi-directional, and can obtain more textures and edges of the image[9,10]. Therefore, this paper chooses NSCT transform. Firstly, the input image is transformed from spatial domain to frequency domain to obtain high-frequency sub-band and low-frequency sub-band; secondly, the low-frequency coefficients are enhanced by anti-sharpening mask algorithm, and the high-frequency coefficients are enhanced by adaptive filtering algorithm[11,12]; thirdly, NSCT is used to inverse transform the image to construct a new image; finally, in order to further enhance the effect of image details, the anti-sharpening mask algorithm is used for image processing.

2. NonsubsampledContourlet transformation (NSCT)

NSCT is conducive to better maintain the image edge information and contour and enhance the translation invariance of the image. It is divided into two processes: multi-scale decomposition and directional filtering. The two processes are independent of each other. **Figure 1** is the overall structure diagram.

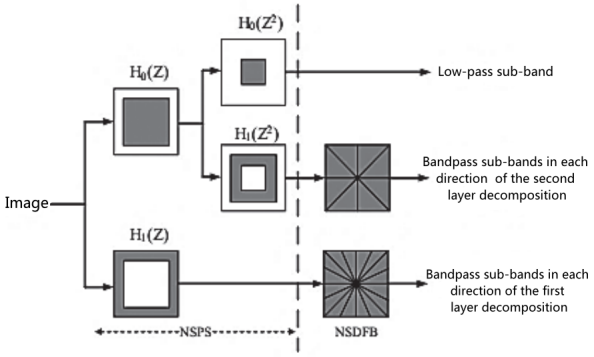

Figure 1. Overall structure diagram.

In view of the translation invariance of Laplace filter, the multi-scale nature of NSCT can be guaranteed by using non-subsampled pyramid for image decomposition. NSCT consists of low-pass decomposition filter module $H_0(z)$ and high pass decomposition filter module $H_1(z) = 1 - H_0(z)$, and some low-pass synthetic filtering modules, which are composed of high pass filtering module $G_0(z) = G_1(z) = 1$.

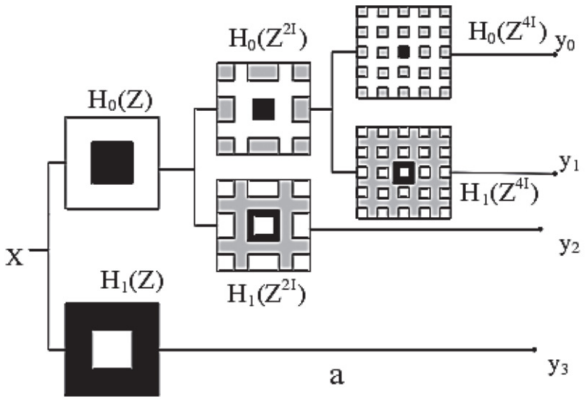

Figure 2. A schematic diagram of the decomposition of three layers of the pyramid.

Figure 2 is the decomposition diagram of three layers of the non-subsampled pyramid, in which the ideal band-pass support region of the low-pass filter decomposed in layer j is $[(\pi/2^J), (\pi/2^J)]^2$, while the ideal band-pass region of the high pass filter is the complement of the low-pass sub-bands $[(-\pi/2^J), (\pi/2^J)]^2/[(-\pi/2^J), (\pi/2^J)]^2$.

Non-subsampling direction filter banks: the filter is based on two channels and decomposes the coefficients into different sub-bands through a tree like structure. The non-subsampling direction filter banks remove the down-sampling module and up-sampling module in the directional filter bank, so that the sampling results at different scales are consistent, and effectively improves the distortion in the sampling process.

3. Micro-nano optical image enhancement algorithm based on NSCT

Due to the multi-scale and multi-directional nature, NSCT has superior transformation function and can effectively improve the image quality. Therefore, we propose a micro-nano optical image enhancement algorithm based on NSCT to preprocess the defocus image obtained under the microscope. Firstly, NSCT decomposes the input image to generate a series of low-frequency and high-frequency components; secondly, the low-frequency coefficients are enhanced by anti-sharpening mask algorithm; adaptive filtering algorithm is used for high-frequency coefficients; finally, all sub-bands are reconstructed by NSCT in-

verse transform.

3.1 NSCT low-frequency coefficient transformation

The low-frequency coefficients obtained by NSCT decomposition contain some basic information in the image. In this paper, the anti-sharpening mask algorithm is used to enhance it.

$$g(x,y) = f(x,y) + k^{*}(f(x,y) - \overline{f}(x,y)) \quad (1)$$

where, in the formula represent the input image and output image respectively, and K is the adjustment coefficient, taking 2. is the blurred image or approximate image, which can be obtained from equation (2).

$$\overline{f}(x,y) = median\{f(x-i,y-j),(i,j) \in W \quad (2)$$

Where, W is the filter window.

3.2 NSCT high-frequency coefficient conversion

High-frequency coefficients represent detailed information, such as image edges and textures, but also contain a lot of noise. High-frequency coefficient transformation aims to achieve enhancement based on noise reduction. High-frequency coefficients with large values contain image edge details and should be retained. Noise is distributed in NSCT high-frequency coefficients with small values. Threshold noise reduction is to set an appropriate threshold, and noise reduction is performed by comparing the absolute value of NSCT coefficient with the threshold. When the absolute value is greater than the threshold, NSCT coefficient is considered to contain important image information and is retained. When the absolute value of NSCT coefficient decreases or becomes 0 accordingly, it is used to filter noise. By using the coefficient processed by threshold, the NSCT inverse transformation is used to reconstruct the image, so as to eliminate the noise. Threshold de-noising eliminates the noise and retains the image coefficient as much as possible. Therefore, the key of de-noising is to determine the threshold. Less than the threshold is regarded as the noise to be suppressed, and more than the threshold is regarded as the edge information to be enhanced.

$$f_{in}(x,y) = \begin{cases} edges, others \\ noise, p \le T_{1,k} \end{cases} \quad (3)$$

$T_{l,k}$ is the noise threshold in the K direction of the 1 layer, and P is the coefficient value of the sub-band.

In this paper, an adaptive filtering algorithm based on BayesShrink is used. The threshold can be calculated by equation (4).

$$T_{1,k} = c\frac{\sigma^2}{\sigma_x^2} \quad (4)$$

Where, c is a constant between 0 and 1, σ^2 is the noise variance, and σ^2_x is the signal variance. The standard deviation of noise can be calculated by equation (5).

$$\sigma = \frac{median(|C_{j,k}|)}{0.6745} \quad (5)$$

Where, $C_{j,k}$ is the high-frequency coefficient of the first layer of the image after NSCT decomposition, i.e., take the median of the absolute value of NSCT coefficients, and calculate the noise standard deviation with 0.6745 as the adjustment coefficient.

$$\sigma_x = \sqrt{max\left(\frac{1}{mn}\sum_{i=1}^{m}\sum_{j=1}^{n} x_{i,j}^2(1,k) - \sigma^2, 0\right)} \quad (6)$$

Where, m and n represent the length and width of the image respectively, and the coefficient located in $X(i, j)$ in the K direction image of layer 1 is $X_{i,j}(1, K)$.

The obtained threshold is used to suppress the noise.

$$x'_{i,J} = \begin{cases} x_{i,j}, x_{i,j} > T_{1,k} \\ 0, x_{i,j} < T_{1,k} \end{cases} \quad (7)$$

Where, $X_{i,j}$ is the coefficient of the high-frequency sub-band of the original image and is the coefficient of the processed image.

The main steps of the algorithm are as follows:

Step 1: NSCT decomposes the defocus image obtained under the microscope to generate a series of low-frequency and high-frequency components;

Step 2: Calculate the low-frequency coefficient obtained by equation (1) to obtain a higher contrast of the image;

Step 3: Adaptive filtering algorithm is used for threshold de-noising of high-frequency coefficients;

Step 4: The image is inversely transformed into the spatial domain by NSCT, and the new image is reconstructed;

Step 5: The reconstructed image is further processed by anti-sharpening mask technology to obtain the optimized clear image.

4. Experimental results and analysis

The experiments are carried out by using the traditional histogram equalization algorithm (HE), Retinex image enhancement algorithm (MSR) and the algorithms proposed in this paper. The experiments are carried out by using the standard nano grid image obtained under the actual optical microscope, the conductive probe and triangular probe sample images collected under the atomic force microscope. **Figure 3**, **Figure 4**, **Figure 5** show the results of preprocessing three kinds of images by three algorithms. Among them, **(a)** is the original image, **(b)** is the image enhanced by histogram equalization algorithm (HE), **(c)** is the image enhanced by Retinex algorithm (MER), and **(d)** is the image enhanced by the algorithm proposed in this paper.

4.1 Subjective evaluation

(1) Standard 500 nm raster image

(2) Conductive probe image

(3) Triangular probe image

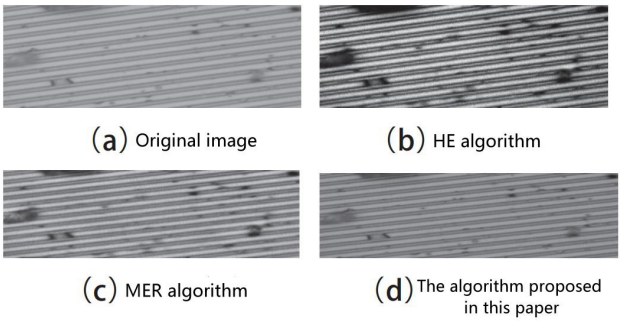

Figure 3. Grid image preprocessing results of three algorithms.

As can be seen from **Figure 3**, **Figure 4**, **Figure 5**, compared with the original image, the clarity and contrast of the three images processed by HE algorithm are greatly improved, and the overall enhancement effect is better. However, the image processed by this algorithm has more noise, and the processing of the edge details of the image is not ideal. Sometimes there will be local distortion and block phenomenon. For example, the standard 500 nm scale grid image is obviously noisy after being processed by HE algorithm; after the conductive probe and triangular probe are processed by HE algorithm, the probe tip appears local distortion.

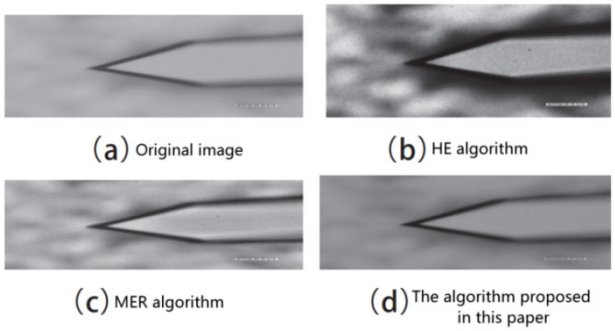

Figure 4. Preprocessing results of three algorithms on conductive probe.

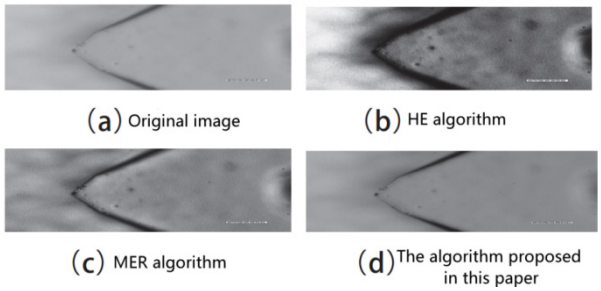

Figure 5. Preprocessing results of three algorithms on triangular probe.

Retinex algorithm decomposes the image into illumination image and reflectance image, and then eliminates or weakens the influence of illumination, so as to achieve the effect of image enhancement. Therefore, compared with the original image, the clarity and contrast of the three kinds of images processed by Retinex algorithm are greatly improved, and the overall enhancement effect is better. However, due to the logarithmic processing, the display range of the bright area of the image is compressed, resulting in the weakening of the details of the image. For example, the details of the edges and corners of the standard 500 nm scale grid, the needles of the conductive probe and the triangular probe are significantly weakened.

Compared with the original image, the sharpness and contrast of the three images processed by the proposed algorithm are improved, and the over-

all effect is better; moreover, the algorithm adopts an adaptive filtering algorithm for high-frequency coefficients to determine the noise determination threshold suitable for different sub-band coefficients. Therefore, compared with the original image, the noise of the three images processed by the algorithm proposed in this paper is very low.

4.2 Objective evaluation

Sharpness, contrast and peak signal-to-noise ratio are three objective indexes commonly used to measure the effect of image enhancement. These three indexes have been used for objective calculation and evaluation in this paper.

(1) Clarity

It mainly reflects the vein part of the image. The larger is the measured value, the clearer is the representative image, as shown in equation (8).

$$\bar{g} = \frac{1}{M \times N} \sum_{i=1}^{M} \sum_{j=1}^{N} \sqrt{\frac{(\Delta_m x(i,j))^2 + (\Delta_n x(i,j))^2}{2}} \tag{8}$$

$\Delta_m x(i, j)$, $\Delta_n x(i, j)$ are the difference points of points (i, j) in vertical and horizontal directions.

(2) Contrast

It represents the overall contrast intensity of the image. Generally, the greater is the contrast, the better is the image enhancement effect. The contrast calculation formula is:

$$Con = \frac{VAR}{\left[\frac{1}{M \times N} \sum_{i=1}^{M} \sum_{j=1}^{N} (x(i,j) - \mu_x)^2\right]^{\frac{1}{4}}} \tag{9}$$

Where, μ_x represents the average value of gray scale, M and N represent the number of pixels in image rows and columns. VAR is the variance of image, and the calculation formula is:

$$VAR = \frac{1}{M \times N} \sum_{i=1}^{M} \sum_{j=1}^{N} (x(i,j) - \mu_x)^2 \tag{10}$$

(3) Peak signal-to-noise ratio

According to the ratio of maximum signal power and noise power, the greater is the PSNR, the better is the image enhancement effect. The calculation formula of PSNR is:

$$PSNR = 10 \times 1g \frac{L \times L}{MSE} \tag{11}$$

Where, L is the gray level range, usually 255, and MSE is the mean square error, which can be calculated by equation (12).

$$MSE = \frac{\sum_{0<j<N} \sum_{0<i<M} (f_{ij} - o_{ij})^2}{M \times N} \tag{12}$$

Where, f_{ij} and O_{ij} are the gray values of the input image and the output image at points (i, j), and M and N represent the number of pixels in the rows and columns of the image.

Table 1, **Table 2** and **Table 3** respectively show the objective evaluation indexes of the images of standard nano grid, triangular probe and conductive

Table 1. Comparison of objective evaluation indexes of three algorithms for raster image processing

Evaluating indicators	Original image	HE algorithm	Retinex algorithm	Textual algorithm
Clarity	3.63	21.02	13.65	5.71
Contrast	10.92	64.65	41.98	14.56
Peak signal-to-noise ratio	—	10.84	15.79	20.49

Table 2. Comparison of objective evaluation indexes of three algorithms for processing conductive probe images

Evaluating indicators	Original image	HE algorithm	Retinex algorithm	Textual algorithm
Clarity	3.68	19.03	12.11	5.16
Contrast	20.35	64.50	29.64	26.76
Peak signal-to-noise ratio	—	10.68	15.12	17.67

Table 3. Comparison of objective evaluation indexes of three algorithms for processing triangular probe images

Evaluating indicators	Original image	HE algorithm	Ritinex algorithm	Textual algorithm
Clarity	3.71	25.32	17.52	5.91
Contrast	13.39	64.63	28.80	15.51
Peak signal-to-noise ratio	—	9.88	14.94	18.67

probe in atomic force microscope processed by three algorithms.

(1) Standard 500 nm scale grid

(2) Conductive probe

(3) Triangular probe

From **Table 1** to **Table 3**, it can be seen that the clarity of different defocused images processed by HE algorithm and Retinex algorithm is relatively high. Although the clarity of defocused images processed by the algorithm proposed in this paper is not very high, it also improves the clarity of different defocused images to a certain extent and can effectively improve the image quality.

The contrast of different defocused images processed by HE algorithm and Retinex algorithm is relatively high. Although the contrast of defocused images processed by the algorithm proposed in this paper is not very high, it also improves the contrast of different defocused images to a certain extent and can effectively improve the image quality.

It can be seen from the peak signal-to-noise ratio data that compared with HE algorithm and Retinex algorithm, the proposed algorithm has the largest peak signal-to-noise ratio, the most information retained, the least distortion and better visual effect.

Therefore, through the comparative experiments of standard nano-grid images obtained under the actual optical microscope, triangular probe and conductive probe sample images collected under the atomic force microscope, it can be seen that the image enhancement effect of the proposed algorithm is relatively better than that of histogram equalization algorithm (HE) and Retinex algorithm (MER), and can effectively improve the image quality.

5. Conclusion

The out of focus images collected under micro-nano optical microscope are not very clear in detail, edge and contour. Combined with NSCT image transformation method, which has multi-scale and multi-directional, and superior transformation function, more texture and edge of the image can be obtained. At the same time, an adaptive noise reduction and enhancement algorithm of micro-nano optical image based on NSCT is proposed to restore the defocus image obtained under the microscope. The experimental results of standard nano-grid images, triangular probe images and conductive probe images show that the enhanced image effect of the algorithm proposed in this paper is better than histogram equalization algorithm (HE) and multi-scale Retinex algorithm, which not only improves the quality of defocused images, but is also conducive to the depth information recovery of subsequent defocused images.

Conflict of interest

No conflict of interest was reported by the author.

Acknowledgements

Project: The next generation Internet technology innovation project of Saier network of the Ministry of Education, “Emergency and Critical Intelligent Medical Cloud Platform based on IPv6” (NGII20170709).

References

1. Hu R. Scanning near-field optical microscopy: Instrumentation and applications [Master’s thesis]. Nanjing: Nanjing University; 2018. p. 91.
2. Lv M, Yu Z. Study on automatic focusing algorithm of optical microscope. China Measurement & Test 2018; 44(6): 11–16.
3. He Z. Research on depth recovery based on defocused images [Master’s thesis]. Harbin: Northeast Agricultural University; 2014. p. 62.
4. Zhu Z, Yin H, Chai Y, *et al.* A novel multi-modality image fusion method based on image decomposition and sparse representation. Information Sciences 2018; 432: 516–529.
5. Chen BH, Wu YL. An entropy-preserving histogram modification algorithm for image contrast enhancement. Proceedings of the 2017 IEEE International Conference on Applied System Innovation (ICASI); 2017; Sapporo. New York: IEEE; 2017. p. 1285–1288.
6. Zhang S. Research on enhancement algorithms of low illumination images and videos based on Retinex

theory [Master's thesis]. Nanjing: Nanjing University of Posts and Telecommunications; 2018. p. 76.
7. Gao Y, Liu G, Ma C. Dense hazy image enhancement based on generalized imaging model. 2018 IEEE 3rd International Conference on Image, Vision and Computing (ICIVC); Jun 27–Jun 29, 2018; Chongqing. New York: IEEE; 2018. p. 410–414.
8. Zhang D. Research on adaptive compressive sampling imaging based on wavelet transformation [Master's thesis]. Chengdu: Southwest Jiaotong University; 2018. p. 69.
9. Liu Z, Xu T, Song Y, *et al.* Image fusion technology based on NSCT and robust principal component analysis model with similar information. Journal of Jilin University (Engineering and Technology Edition) 2018; (5): 1614–1620.
10. Liu L. Research on image enhancement algorithm based on NSCT [Master's Thesis]. Urumqi: Xinjiang University; 2016.
11. Pal NS, Lal S, Shinghal K. A robust framework for visibility enhancement of foggy images. Engineering Science and Technology 2019; 22(1): 22–32.
12. Chen B, Wu Y, Shi L. A fast image contrast enhancement algorithm using entropy-preserving mapping prior. IEEE Transactions on Circuits and Systems for Video Technology 2017; 20(2): 212–232.

Characterization and Application of Nanomaterials (2021) Volume 4 Issue 2
doi:10.24294/can.v4i2.1336

ORIGINAL RESEARCH ARTICLE

Spin thermoelectric effects on aluminum or phosphorus doped zigzag silicene nanoribbons

Jiali Song[1], Xue Zhang[1], Xuefeng Wang[2], Jinfu Feng[1,3], Yushen Liu[1,3*]

[1] *School of Physics and Electronic Engineering, Changshu Institute of Technology, Changshu 215500, China*

[2] *Jiangsu Laboratory of Advanced Functional Materials, Changshu 215500, China*

[3] *School of Physical Science and Technology, Soochow University, Suzhou 215006, China. E-mail: ysliu@cslg.cn*

ABSTRACT

Based on the density-functional theory (DFT) combined with nonequilibrium Green's function (NGF), this paper investigates the effects of either single aluminum (Al) or single phosphorus (P) atom substitutions at different edge positions of zigzag-edged silicene nanoribbons (ZGNRs) in the ferromagnetic state on the spin-dependent transport properties and spin thermoelectric effects. It has been found that the spin polarization at the Fermi level can reach 100% or –100% in the doped ZSiNRs. Meanwhile, the spin-up Seebeck effect (for –100% case) and spin-down Seebeck effect (for 100% case) are also enhanced. Moreover, the spin Seebeck coefficient is much larger than the corresponding charge Seebeck coefficient at a special doping position and electron energy. Therefore, the study shows that the Al or P doped ZSiNRs can be used to prepare the ideal thermospin devices.

Keywords: Silicene Nanoribbons; Doping; Spin Seebeck Coefficients

ARTICLE INFO

Received: 10 August 2021
Accepted: 4 October 2021
Available online: 9 October 2021

1. Introduction

Since graphene was successfully prepared by mechanical method for the first time in 2004, people have become more and more interested in other two-dimensional honeycomb structural materials[1]. Among them, silicone material is such a structure-silicon atoms of two-dimensional hexagonal lattice. Unlike graphene with planar structure, because the distance between silicon atoms is farther than that between carbon atoms, therefore, silene has a low degree of fold structure, and the distance between its two silicon atoms is about 0.44 Å[2]. Its unique geometry brings many interesting properties, such as quantum Hall effect[3], large spin orbit interaction[4] and mechanically adjustable energy gap[5]. Similar to graphene, in the Fermi level and zero band gap structure, silene has a semi metallic low energy state. Although spin orbit coupling can open an energy gap at the Dirac energy point, its value is only 1.5 meV[3]. However, from the perspective of application, we need to open a relatively large energy gap. Silene nanoribbons provide a feasible method. Recent experimental studies have confirmed that one-dimensional silene nanostructures can be prepared[6]. Similar to graphene ribbons, silene nanoribbons also have two types of edges, namely serrated silene ribbons (ZSiNRs) and armrest silene ribbons (ASiNRs). Hydrogen saturated armrest nano ribbons can behave as semiconductors and metals according to the change of their length. However, the

ground state of hydrogen saturated sawtooth silene nano ribbons is the boundary antiferromagnetically coupled semiconductor state[6]. Under the action of the transverse electric field, for boundary doping with phosphorus or nitrogen atoms in the serrated silene nanoband, its magnetic semiconductor state can be converted into a semimetallic state[7].

Recently, molecular dynamics studies have shown that the boundary hydrogen saturated silene nanoribbons have very good stability, and their geometry even exists under 800 K temperature[8]. This shows that hydrogen saturated silene nanoribbons can be used to prepare very stable thermoelectric devices. Based on the first principle method, Zberecki *et al.* found that due to a conductivity gap on the Fermi surface, its conductivity is extremely suppressed. Due to the inverse relationship between Seebeck coefficient and conductivity in the low temperature region, it leads to the great increase of its thermoelectric coefficient[9]. In addition, with the maturity of spin detection technology, people can detect spin current through spin Hall effect. In 2008, the phenomenon that a spin flow can arise when a temperature gradient is applied at both ends of the magnetic metal Ni81Fe19 connected to the Pt line was found by Uchida et al[10]. Similar to the traditional charge thermoelectric effect, this effect is called "spin Seebeck effect" or "thermal spin effect". This pioneering experiment has stimulated a large number of relevant theoretical and experimental studies[11–17]. When the silene nanoribbons are in the boundary ferromagnetic coupling state, they exhibit spin degenerate metal behavior at the Fermi plane. Because the boundary antiferromagnetic state shows semiconductor behavior, such a large magnetoresistance behavior can be found[18].

In this paper, the spin thermoelectric effect of single aluminum (Al) or phosphorus (P) atomic boundary instead of doped ZSiNRs double probe structure will be studied in the first principle (see **Figure 1**). This device consists of the left electrode part, the intermediate scattering region, and the right electrode part. The width of ZSiNRs is 6. We consider four different boundary doping positions and find that for Al atom doping, the spin polarization at the Fermi plane is close to –100% at the second and third positions, but it is just the opposite for P atom doping. The results show that for phosphorus atom doping, at position 3, the spin polarizability at the Fermi surface reaches 100%. The main reason is that there are transmission nodes at the Fermi surface. At the same time, the spin thermoelectric coefficient at the Fermi is also significantly strengthened By adjusting the electron energy, the spin thermoelectric coefficient of doped ZSiNRs can be similar to or even greater than the charge thermoelectric coefficient.

2. Model establishment

Bilateral monohydrogenated ZSiNRs are used as the original package of the nano system, and the bandwidth is generally taken as 6. Using VASP software package, we first optimized the FM state single package structure of hydrogenated ZSiNRs, and the cut-off energy is taken as 360 eV[19]. The exchange correlation function adopts generalized gradient approximation (GGAPBE). The maximum force per atom does not exceed 0.01 eVA^{-1}. After geometric optimization, based on the original package structure, this paper designed a nano double probe system as shown in **Figure 1**. The boundary Si atoms are saturated with H atoms. The Si atoms with middle marks 1–4 in the middle scattering region are replaced with other atoms respectively (i.e. only one Si atom is replaced for each doping). The atoms replaced in this paper include Al and P. Here, for simplicity, Al doped silene nanoribbons are referred to as Al-ZSiNRs; P-doped silene nanoribbons are abbreviated as P-ZSiNRs.

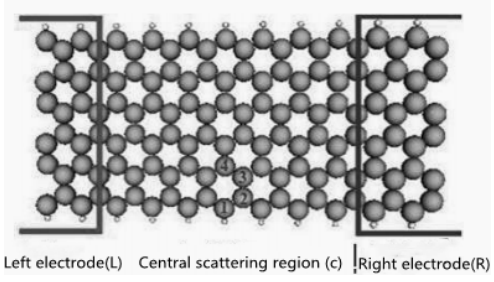

Figure 1. A spin device structure composed of 6-ZSiNRs. The box on the left represents the left electrode and the box on the right represents the right electrode. 1–4 in the figure represents different doping positions in the scattering region. The large ball represents Si atom and the small ball represents H atom.

In this paper, a software package Atomistix Toolkit (ATK) based on nonequilibrium Green's function and density functional theory is used to complete the calculation and Simulation of the electron transport process of the system. The system optimization adopts Newton optimization. The exchange correlation function adopts generalized gradient approximation (GGA), and the basis vector adopts DZP (Double Zeta Polarized). The size of the contracted Brillouin area is set to (1, 1, 100). In order to avoid the interaction between images, the vacuum layer is taken as 15 Å and the energy truncation radius is taken as 150 Ry.

The electron transmission coefficient of the eigenenergy of E is:

$$\tau_\sigma(E) = T_r[\,\Gamma_L(E)\,G^r(E)\,\Gamma_R(E)\,G^a(E)\,]_\sigma \quad (1)$$

Here $\Gamma_{L/R}(E)$ is the wire width function of the central center coupled to the left/right wire, σ is the spin exponential index and E is the energy. $G_{R/A}(E)$ is the delayed and advance Green function of the central scattering region and can be calculated by equations $G_\sigma^r = [E\mathrm{I} - H + i(\Gamma_{L\sigma} + \Gamma_{R\sigma})/2]^{-1}$ and $G_\sigma^a = [Gr_\sigma^r]$. I is the unit matrix and H is the Hamiltonian of the central scattering region.

The spin polarizability at the Fermi plane can be defined as:

$$P = \frac{\tau_\uparrow - \tau_\downarrow}{\tau_\uparrow + \tau_\downarrow} \times 100\% \quad (2)$$

In order to study the spin thermoelectric effect, we give the expression of spin dependent Seebeck coefficient in the linear region:

$$S_\sigma = -\frac{L_{1\sigma}(\mu, T)}{|e|TL_{0\sigma}(\mu, T)} \quad (3)$$

Where,

$L_n = \sum_\sigma L_{n\sigma}$, $L_{n\sigma} = -\frac{1}{h}\int dE T_\sigma(E)(E-\mu)^n \frac{\partial f}{\partial E}, n = 0,1,2$, $f_{L(R)}$ is the Fermi Dirac distribution function. Spin Seebeck coefficient is expressed as $S_s = (S_\uparrow - S_\downarrow)/2$, and the corresponding charge Seebeck coefficient is $S_c = (S_\uparrow + S_\downarrow)/2$[20].

3. Results and discussion

Formula (3) can be reduced at low temperatures to:

$$S_\sigma(\mu) \simeq -\frac{\pi^2 k_B^2 T}{3e}\frac{\tau_0'}{\tau_0}(\mu) \quad (4)$$

The formula (4) shows that the spin-dependent Seebeck coefficient and transmission odds are proportional to the slope of the energy, and inversely proportional to its size. **Figure 2(a)** shows the transmission spectrum of pure ZSiNRs in the energy range [–2 eV, 2 eV]. It can be seen from **Figure 2(a)** that the complete ZSiNRs shows typical metal behavior, that is, the transmission function value near the Fermi level ($E = E_F = 0$), $\tau_\sigma(E) = 1$ is a constant. The upper and lower spin channels are almost degenerate. For the spin-up channel, a peak is generated in the energy $E - E_F \approx -0.2$ eV region, and its transmission function value is $\tau_\sigma(E) \approx 3$. For the spin-down channel, a peak is generated near the energy $E - E_F \approx 0.1$ eV, and its transmission function value is $\tau_\sigma(E) \approx 3$. **Figure 2(b)** shows the relationship between the spin-dependent thermoelectric coefficient S_σ and the chemical potential μ for the pure ZSiNRs. Here the

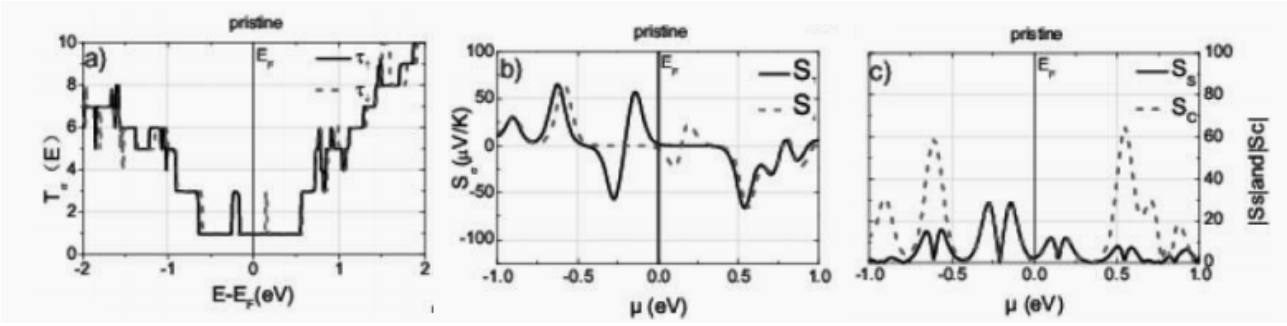

Figure 2. The transmission spectrum and thermal power coefficients of the full ZSiNRs at zero bias. **(a)** For the T_0-energy relation diagram, **(b)** and **(c)** for the absolute value of the spin-correlation thermoelectric coefficient Sσ and the spin (charge) Seebeck coefficient for the pure ZSiNRs $|S_S|(|S_C|)$.

temperature is taken as 300 K. We find that with the change of chemical potential μ, the spin-associated thermoelectric coefficient S_σ of the full ZSiNRs (FM state) is significantly enhanced at the position where the transport function has mutations. The spin polarizability at the Fermi surface is close to zero and its Seebeck coefficient is very weak. The main reason is that the slope of the transmission probability at the Fermi surface is almost zero.

Figure 3 shows the spin dependent transmission spectra of ZSiNRs with different doping types and doping positions. From the figure, we can see that when ZSiNRs is doped, the upper and lower spin electron transport characteristics appear non-degenerate phenomenon, and the non-degenerate phenomenon shows different behavior with different doping positions (position 1 turns to 4 in turn). There are some conductivity troughs on both sides of Fermi level (also known as local quantum state). The transmission spectrum of doped ZSiNRs is related not only to the spin direction, but also to the type and position of doping. As shown in **Figures 3(a)** and **(b)**, when the edge of pure ZSiNRs along Si atom (**Figure 1**, position 1) is replaced by Al or P atoms, the metal behavior near the Fermi level remains almost unchanged, and the spin degeneracy phenomenon is still obvious. For spin-up electrons both doping causes a conductance trough at energy slightly below E_F and for spin-down electrons a similar narrow decrease at energy slightly above E_F, there was a more pronounced decrease near the $|E - E_F| \approx 0.5$ eV, with a decrease in the transmission function of both the upper and lower spins. When the doping position is moved to position 2 in **Figure 1**, the transmission spectrum of Al-ZSiNRs in **Figure 3(c)** changes more obviously, and its spin degeneracy is destroyed. At the Fermi level ($E - E_F = 0$), the upper spin transmission function of Al doped ZSiNRs is obviously suppressed, while the lower spin transmission function remains unchanged. **Figure 3(d)** shows that the transmission function of P-ZSiNRs is just the opposite here. Compared with the change of the transmission spectrum of doped ZSiNRs at position 1, the spin dependent local quantum state of P-ZSiNRs near $E - E_F \approx -0.5$ eV disappears; while the spin dependent local quantum state of Al-ZSiNRs near $E - E_F \approx 0.5$ eV disappears, and there are more narrow falling states near $E - E_F \approx -0.5$ Ev. When the doping position moves to position 3, the spin degeneracy of the transmission spectra of Al-ZSiNRs or P-ZSiNRs in **Figures 3(e)** and **(f)** is further destroyed, and the former is more obvious. Interestingly, at the Fermi level ($E - E_F = 0$) nearby, the inhibition of the upper-spin transmission function of Al-ZSiNRs intensifies, $\tau_\uparrow = 0$, that is, the spin upward behavior of ZSiNRs changes from metallicity to insulation, while the lower-spin transmission function remains unchanged; its spin polarizability even reaches –100%. The case of P-ZSiNRs transmission function is just the opposite. Its spin polarizability can be close to 100%. Similarly, the transmission function of Al-ZSiNRs at $E - E_F \approx 0.5$ eV also has a trough, while the trough of P-ZSiNRs appears at $E - E_F \approx 0.5$ eV. When the doping is further to position 4, for the two spin channels, the transmission function of doped ZSiNRs shows cash properties near the Fermi level, and the metal behavior of the system is restored.

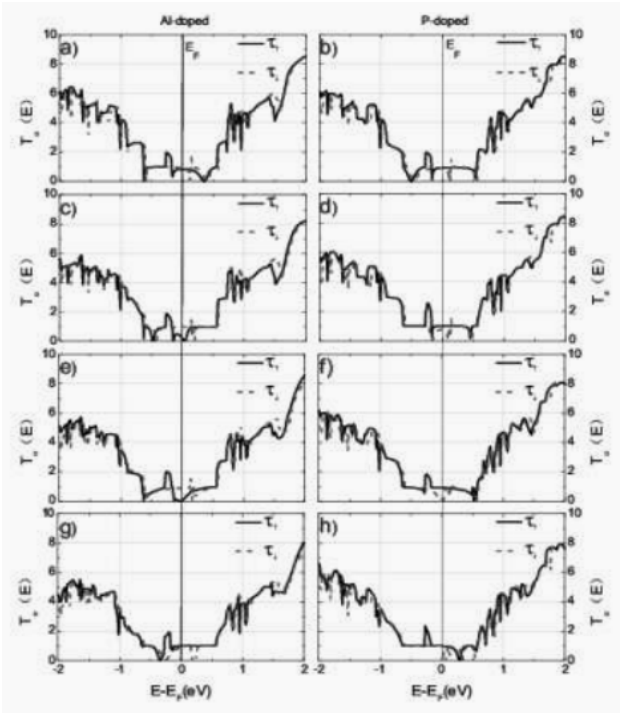

Figure 3. Transmission spectrum of the ferromagnetic state ZSiNRs doped with Al (left) and P (right) at zero bias. Black and red lines are represented, upper spin and lower spin electrons, respectively. The left and right columns represent the ZSiNRs transmission spectra at different doping positions of Al and P, respectively.

Figure 4 and **Figure 5** show the relationship between the spin-dependent thermoelectric coefficient S_σ and the spin (charge) Seebeck coefficient $S_s(S_c)$ and the chemical potential μ of the ZSiNRs for different doping positions and types, respectively. Here, the temperature T = 300 K. For each spin channel of the pure silene band, the transmission spectrum is spin-degenerate. Since $\tau_{E=E_F} = 1$ and $\tau'(E_F) = 0$, $S_\sigma = 0$, near the transmission probability node, the corresponding spin thermoelectric effect is significantly strengthened. For example, when the doping position is 1, both the spin-dependent thermoelectric coefficient S_σ of **Figure 4(a)** at $\mu \approx 0.2$ eV and (b) P-ZSiNRs at $\mu \approx -0.5$ eV, ZSiNRs is enhanced. Only the positions of the positive maximum and negative maximum of $S_\uparrow$ and $S_\downarrow$ are slightly different, which leads to the obvious strengthening of the spin thermoelectric effect, which is comparable to the corresponding charges (as shown in **Figures 5(a)** and **(b)**). However, the thermoelectric effect at the Fermi plane is relatively weak. With the doping position moving to position 2, the $S_\uparrow$ corresponding to the μ = 0 of Al-ZSiNRs is significantly strengthened, but $S_\downarrow$ maintains a relatively weak value. The main reason is that there is a node in the spin upward transmission probability at about 0.05 eV on the Fermi plane. Since the slope of $\tau_\uparrow$ at the Fermi plane is positive, according to the formula (4), its value should be negative, which is in good agreement with our numerical results (as shown in **Figure 4(c)**). While **4(d)** P-ZSiNRs shows that the spin dependent thermoelectric effect is relatively weak at $\mu = 0$.

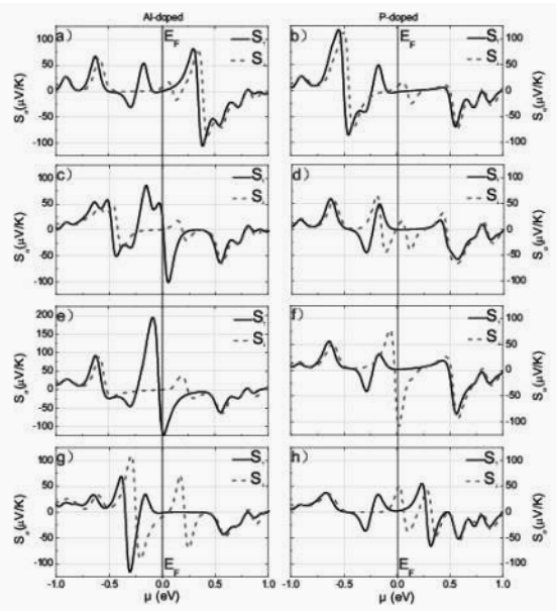

Figure 4. Spin-dependent thermoelectric coefficient function Sσ of chemical potential μ for the ferro ZSiNRs of Al (left) and P (right) at zero bias. Black and red lines represent upper spin and lower spin electrons, respectively. The left and right columns represent ZSiNRs at different doping positions of Al (left) and P (right), respectively.

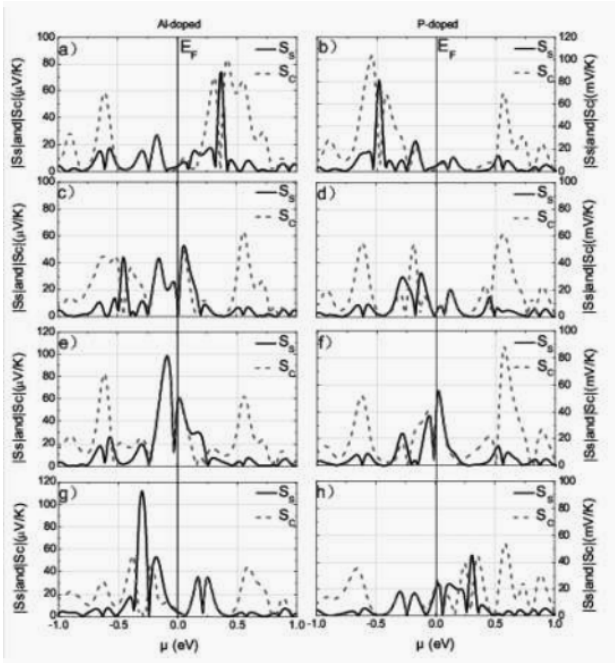

Figure 5. Ferromagnetic ZSiNRs (N = 6) doped with Al (left column) and P (right column) at zero bias with respect to chemical potential μ. The spin (charge) thermoelectric coefficient function $|S_s|(|S_c|)$. The black line and red line represent $|S_s|$ and $|S_c|$. The left and right columns represent $|S_s|(|S_c|)$ of ZSiNRs at different doping positions of Al (left) and P (right) respectively.

However, when the doping position is moved from position 2 to position 3, it can be seen from **Figures 4(e)** and **(f)** that in the Al-ZSiNRs (P-ZSiNRs) system μ = 0, $S_\uparrow(S_\downarrow)$ is greatly enhanced, but $S_\downarrow(S_\uparrow)$ is almost zero, resulting in $|S_s| \approx |S_c|$ (as shown in **Figures 5(e)** and **(f)**). When the doping position is moved to position 4, the spin related thermoelectric effect becomes relatively weak because the semi metallic property at the Fermi plane is transformed into metal property. Looking at **Figure 5(g)**, we find that for Al-ZSiNRs, at energy $\mu \approx -0.3$ eV, there is a high spin thermoelectric effect, while the corresponding charge thermoelectric coefficient is very small, al-

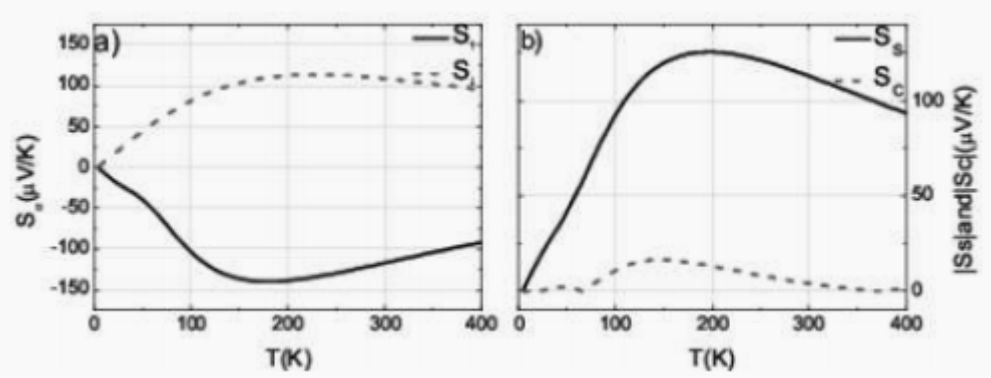

Figure 6. Chemical potential is fixed under zero bias voltage μ = –0.3 eV, when the doping position is 4, spin dependent thermoelectric coefficient S_σ of Al-ZSiNRs spin (charge) thermoelectric coefficient $|S_s|(|S_c|)$ versus temperature.

most zero. Therefore, we fix the chemical potential μ = –0.3 eV, and calculated the Al-ZSiNRs relation of S_σ and $|S_s|(|S_c|)$ with temperature T. The temperature range is taken as [0, 400 k] (as shown in **Figure 6**). As the temperature T changes from 0 to 400 K, the signs of $S_\uparrow$ and $S_\downarrow$ are opposite, and $|S_c|$ changes little in the whole temperature range, and its value is almost zero. Therefore, for the nano equipment based on ZSiNRs, we can obtain an almost ideal pure self-swirl generation device by doping Al atoms in specific parts.

4. Conclusion

We propose a spin thermoelectric device composed of doped silene nanoribbons (ZSiNRs). Here, the doping method of ZSiNRs is to replace the Si atom at the edge with Al and P atoms. We find that due to Al(P) doping, some spin up (down) quantum states appear near the Fermi level, which leads to the spin polarizability close to –100% (aluminum atom doping) and 100% (phosphorus atom doping). In addition, the thermoelectric coefficient of doped ZSiNRs, including spin dependent thermoelectric coefficient and spin (charge) thermoelectric coefficient, has been significantly strengthened. While Al atom doping at a specific position can obtain an ideal pure self-swirling thermoelectric device.

Conflict of interest

The authors declare that they have no conflict of interest.

Acknowledgements

This paper was supported by National Natural Science Foundation of China “Research on theory and application of molecular thermoelectric devices” (11247028).

References

1. Novoselov KS, Geim AK, Morozov SV, *et al.* Electric field effect in atomically thin carbon films. Science 2004; 306: 666–669.
2. Morishita T, Nishio K, Mikami M. Formation of single- and double-layer silicon in slit pores. Physical Review B, Condensed Matter 2008; 77: 081401(R).
3. Liu C, Feng W, Yao Y. Quantum spin hall effect in silicene and two-dimensional germanium. Physical Review Letters 2011; 107(7): 6802.
4. Liu C, Jiang H, Yao Y. Low-energy effective Hamiltonian involving spin-orbit coupling in silicene and two-dimensional Germanium and tin. Physical Review B 2011; 84(19): 5403.
5. Topsakal M, Ciraci S. Elastic and plastic deformation of graphene, silicene, and boron nitride honeycomb nanoribbons under uniaxial tension: A first-principles density-functional theory study. Physical Review B, Condensed Matter 2010; 81(2): 4107.
6. Padova PD, Quaresima C, Ottaviani C, *et al.* Evidence of graphene-like electronic signature in silicene nanoribbons. Applied Physics Letters 2010; 96(26): 1905.
7. Fang D, Zhang S, Xu H. Tuning the electronic and magnetic properties of zigzag silicene nanoribbons

by edge hydrogenation and doping. RSC Advances 2013; 3: 24075–24080.
8. Pan L, Liu H, Tan X, *et al.* Thermoelectric properties of armchair and zigzag silicene nanoribbons. Physical Chemistry Chemical Physics: PCCP 2012; 14: 13588–13593.
9. Zberecki K, Wierzbicki M, Barna J, *et al.* Thermoelectric effects in silicene nanoribbons. Physical Review B 2013; 88(11): 5404.
10. Uchida K, Takahashi S, Harii K, *et al.* Observation of the spin Seebeck effect. Nature 2008; 455(7214): 778–781.
11. Adachi H, Ohe J, Takahashi S, *et al.* Linear-response theory of spin Seebeck effect in ferromagnetic insulators. Physical Review B 2011; 83(9): 4410.
12. Jaworski CM, Myers RC, Johnston-Halperin E, *et al.* Giant spin Seebeck effect in a non-magnetic material. Nature 2012; 487(7406): 210–213.
13. Weiler M, Althammer M, Czeschka FD, *et al.* Local charge and spin currents in magnetothermal landscapes. Physics Review Letters 2012; 108(10): 6602.
14. Uchida K, Nonaka T, Kikkawa T. Longitudinal spin Seebeck effect in various garnet ferrites. Physical Review B, Condensed Matter 2013; 87(10): 4412.
15. Zeng M, Huang W, Liang G. Spin-dependent thermoelectric effects in graphene-based spin valves. Nanoscale 2013; 5(1): 200–208.
16. Liu Y, Yang X, Chi F, *et al.* A proposal for time-dependent pure-spin-current generators. Applied Physics Letters 2012; 101(21): 3109.
17. Liu Y, Wang X, Chi F. Non-magnetic doping induced a high spin-filter efficiency and large spin Seebeck effect in zigzag graphene nanoribbons. Journal of Materials Chemistry C 2013; 1(48): 8046–8051.
18. Chen A, Wang X, Vasiopoulous P, *et al.* Spin-dependent ballistic transport properties and electronic structures of pristine and edge-doped zigzag silicene nanoribbons: Large magnetoresistance. Physical Chemistry Chemical Physics 2014; 16(11): 5113–5118.
19. Kresse G, Hafner J. Ab-initio molecular dynamics for liquid metals. Physical Review B, Condensed Matter 1993; 47(1): 558–561.
20. Dubi Y, Ventra MD. Thermospin effects in a quantum dot connected to ferromagnetic leads. Physical Review B 2009; 79: 081302(R).

Characterization and Application of Nanomaterials (2021) Volume 4 Issue 2
doi:10.24294/can.v4i2.1337

ORIGINAL RESEARCH ARTICLE

Preparation and characterization of branched micro/nano Se

Yongjun Wu*

Software and Food Engineering Department, Maanshan Teacher's College, Maanshan 243041, Anhui, China. E-mail: wyj0555@126.com

ABSTRACT

Branched micro/nano Se was prepared by the redaction of L-Cys•HCl and H_2SeO_3 in hydrothermal method, as β-CD was used as soft template. The structures of products were characterized by SEM, TEM and XRD. Some important factors influencing the morphology of products were studied and discussed, including the amounts of soft template, the reaction temperature and the reaction time. The results showed that external causes had a potent effect on the morphology of micro/nano Se. The uniform branched micro/nano Se prepared under the optimal reaction condition was rhombohedral trigonal selenium t-Se^0, but its crystallinity degree was low.

Keywords: Branched Se; β-CD; Micro/Nanoparticles; Morphology; Rhombohedral Phase

ARTICLE INFO

Received: 15 Augest 2021
Accepted: 8 October 2021
Available online: 15 October 2021

1. Introduction

Selenium is an important elemental semiconductor material with excellent photoelectronic and catalytic properties and is widely used in photosensitive elements, solar cells, ceramic coatings, functional catalytic materials and other application fields[1]. Meanwhile, as an essential trace element in human body, selenium has important physiological functions such as scavenging free radicals, antagonizing toxins, promoting reproduction, regulating metabolism and enhancing immunity[2]. In the traditional selenium supplement products, inorganic selenium and organic selenium have some disadvantages, such as higher toxicity, difficult absorption and high price. In contrast, nano-selenium has significant low toxicity and high efficiency, making it an ideal selenium source for selenium supplement preparations[3].

At present, the reported synthesis methods of nano-selenium mainly include template method, microemulsion method, ultrasonic chemistry method, temperature control method, interface chemistry method, etc.[4,5]. In this study, Se^0 was prepared by hydrothermal method with reductive L-Cys•HCl and H_2SeO_3, and β-CD was used as template agent to control the growth of Se^0 particles. The effects of surfactant dosage, reaction temperature and reaction time on the morphology, particle size and structure of micro-nano Se^0 were studied.

2. Materials and methods

2.1 Materials and instruments

Materials: SeO_2(A.R), L-Cys•HCl(A.R), food-grade β-CD, industrial alcohol, re-steam water, deionized water.

Instruments: S-4,800 scanning electron microscopy (HITACHI), FEI Tecnai G2 F20 transmission electron microscopy (JEOL), Y-4Q X-ray diffractometer (Dandong Ray), DHG-9101-3SA type air blowing drying oven (Shanghai SANFA), DS-8510DTH ultrasonic cleaning instrument (Shanghai SXSONIC), TGL-16A centrifuge (Jintan Huanyu), F1004B electronic balance (Shanghai YUEPING).

2.2 Experimental methods

L-Cys•HCl with a weight of 0.6306 g (4.0 mmol was placed in a reaction kettle. A certain amount of template β-CD solution (0.5 g/L) was dropped and shaken evenly, then 80 mL 0.05 mol/L H_2SeO_3 was added. At this time, n (L-Cys•HCl) : n (H_2SeO_3) = 1:1 in the reaction system. After shaking well, the product was placed in a drying oven with air blast and heated at constant temperature for a certain time. The product was ultrasonic cleaned with deionized water for 4 times, and then ultrasonic cleaned with industrial alcohol for 4 times. Se^0 product was obtained after centrifugation and natural drying. The effects of β-CD dosage, reaction temperature and reaction time on Se crystal morphology and crystal state were studied by single factor experiment.

3. Experiment and analysis

3.1 The influence of the ratio of reactant substance to the reaction rate

Fixed H_2SeO_3 dosage as 4.0 mmol (80 mL 0.05 mol/L); used different reactant molar ratios, namely, n (L-Cys•HCl) : n (H_2SeO_3) = 1:3, 2:3, 1:1, 4:3, 5:3, 2:1; no β-CD template was added, and the reaction was conducted at 110 ℃. Three parallel experiments were conducted for each mole ratio, and the time of the solution turning into light orange was recorded and the average value was taken. The result is shown in **Figure 1**.

With the increase of the amount of L-Cys•HCl in the reactants, the discoloration time of the reaction solution is rapidly shortened within the range of 1:3 to 4:3 when the ratio of (L-Cys•HCl : H_2SeO_3) to the amount of reactants increases, indicating that the reaction speed is accelerated, but the ratio of the amount of reactants is greater than 4:3, the discoloration time basically remained unchanged, indicating that increasing the amount of L-Cys•HCl could not significantly accelerate the reaction rate.

3.2 Influence of the ratio of reactants to reactants on product yield

Fixed H_2SeO_3 dosage as 4.0 mmol (80 mL 0.05 mol/L); used different reactant molar ratio, namely n (L-Cys•HCl) : n (H_2SeO_3) = 1:3, 2:3, 1:1, 4:3, 5:3, 2:1; no β-CD template was added and the reaction was conducted at 110 ℃ for 2 h. Three parallel experiments were performed for each mole ratio. The product was cleaned by ultrasonic cleaning with deionized water once, and then by ultrasonic cleaning with industrial alcohol once. After natural drying, the product was weighed and the average yield was calculated. The result is shown in **Figure 2**.

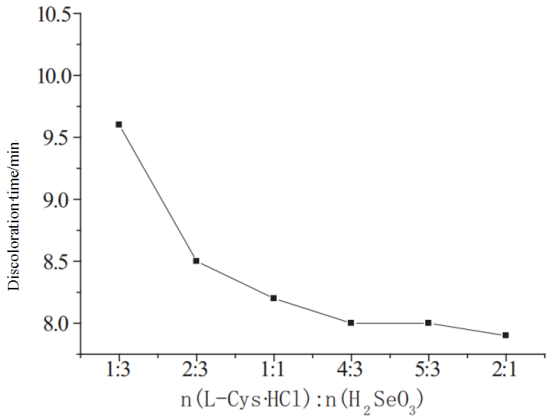

Figure 1. Effect of the ratio of reactants to substances on the reaction rate.

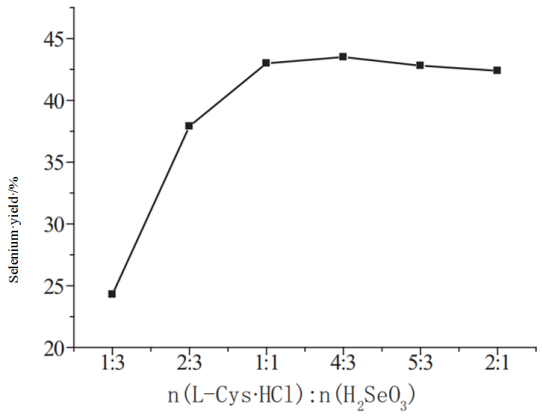

Figure 2. Effect of the ratio of reactants to substances on the yield.

With the increase of the dosage of L-Cys•HCl, the yield of reactant mass ratio *n* (L-Cys•HCl) : *n* (H_2SeO_3) was in the range of 1:3–1:1, but the increase rate gradually decreased. When the molar ratio of reactants was 1:1, the yield fluctuated slightly but did not increase significantly, indicating that the selenium in selenite could not be reduced by hydroxylamine hydrochloride under experimental conditions. Compared with the preparation of Se^0 by Vc and H_2SeO_3, the lower selenium yield in this method also confirms the weak reducibility of L-Cys•HCl. The fluctuation of yield after the molar ratio of 1:1 was related to the quality loss caused by cleaning products.

Based on the above facts, the molar ratio of the reactants *n* (L-Cys•HCl) : *n* (H_2SeO_3) = 1:1 is appropriate.

3.3 Influence of dosage of template agent on product morphology

Using the experimental method in 2.2, the reaction temperature was fixed at 110 ℃ and the reaction time was 2 h, and 0.5 g/L *β*-CD solution 0, 2.0, 4.0, 8.0, 16.0 ml (equivalent *β*-CD is 0, 1.0, 2.0, 4.0 and 8.0 mg) was added respectively, and the single factor comparison test is carried out. After ultrasonic cleaning, the product is detected by SEM, as shown in **Figure 3(a)** ~ **Figure 3(e)**.

The product prepared without *β*-CD was severely adhered selenium balls, similar to ginger cubes, as shown in **Figure 3(a)**. At this time, because there is no soft template in the reaction solution, the selenium grains cannot be stable after generation, and inevitably adsorb and combine with each other. In the deposition, the nucleation rate in solution is less than the nuclear growth rate, and the small-scale selenium nanoparticles cannot be obtained. When 2.0 mL *β*-CD solution was added, the aggregation and adsorption of selenium grains were prevented under the control of *β*-CD macromolecules, and the products were dispersed to a certain extent. At this time, dispersed selenium pellets were obtained, with cracks visible on the surface, as shown in **Figure 3(b)**. When 4.0 mL *β*-CD solution was added, selenium pellets increased and a large number of short selenium buds grew on some selenium pellets, as shown in **Figure 3(c)**. When 8.0 mL *β*-CD solution was added, the buds of selenium grew significantly and became selenium filaments. Some of the selenium filaments connected to each other and formed branched selenium, as shown in **Figure 3(d)**. When 16.0 mL *β*-CD solution was added, the selenium in the branches was significantly reduced and the diameter of selenium pellets was slightly increased, as shown in **Figure 3(e)**.

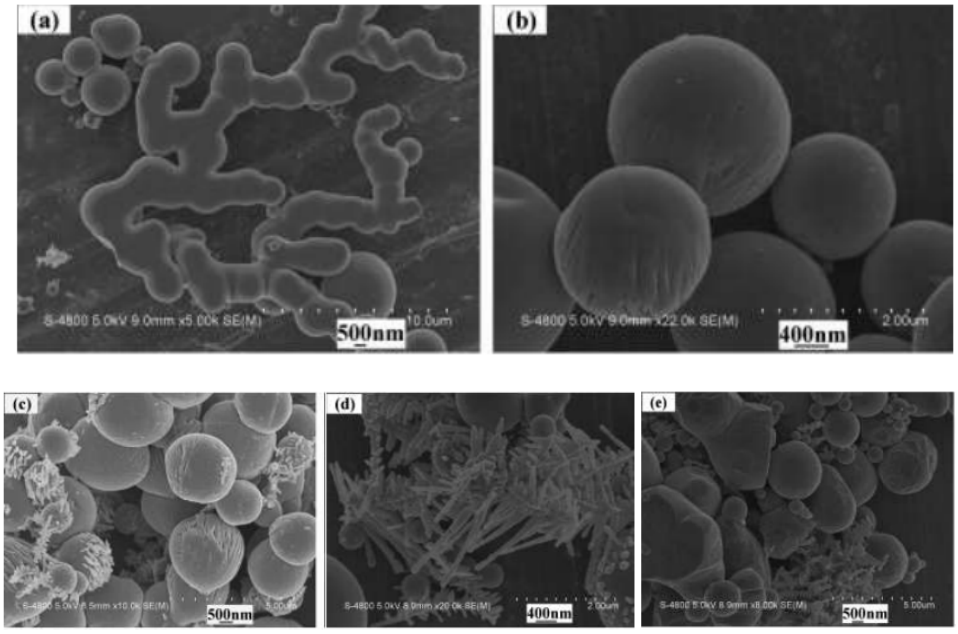

Figure 3. Effect of the amount of *β*-CD on the morphology of the product.

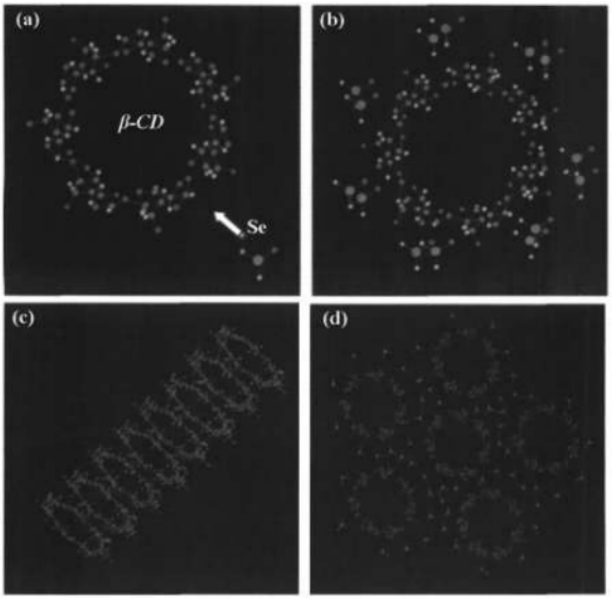

Figure 4. The self-assembly principle for *β*-CD adsorbing Se.

The appearance of selenium with the above morphology is related to the soft template *β*-CD, which has many hydroxyl groups in the structure, and its self-assembly principle is as follows[6]: the Se nuclei generated in aqueous solution preferentially adsorb on the active hydroxyl groups through hydrogen bonds (**Figure 4a**, **Figure 4b**), and complete self-assembly in two directions with the assistance of template agent *β*-CD. Among them, *β*-CD molecules interact longitudinally (**Figure 4c**), extending and assembling into a one-dimensional long chain structure as a whole. In the transverse direction (**Figure 4d**), under the guidance of its special inner hydrophobic and outer hydrophilic structure, *β*-CD assembles a planar two-dimensional structure. Finally, *β*-CD self-assembled into a three-dimensional ordered supramolecular shell, which became a reticular limiting template to guide the growth of selenium grains. Selenium nanocrystals are deposited and grown into selenium spheres. With the increase of the concentration of *β*-CD, the volume of the cross-linked macromolecules will increase, and the particle size of the selenium materials grown by its guiding limit will inevitably increase.

Based on the above experimental results, the optimal concentration of *β*-CD solution (0.5 g/L) was determined to be 8.0 mL (equivalent to 4.0 mg *β*-CD).

3.4 Influence of reaction temperature on product morphology

Using the experimental method described in step 2.2, the amount of soft template *β*-CD solution was 8.0 mL (equivalent to 4.0 mg *β*-CD). The reaction temperature was set at 90, 110, 130, 150, 170 ℃ for 2 h, and the single factor comparison test was conducted. The morphologic changes of ultrasonic cleaning products were shown in **Figure 5(a)** ~ **Figure 5(e)**.

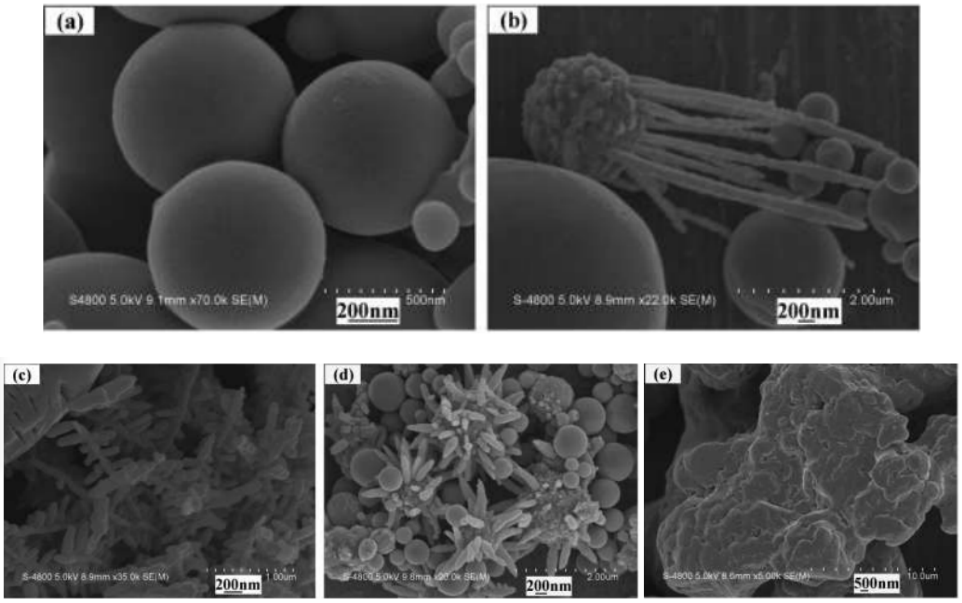

Figure 5. Effect of reaction temperature on the morphology of products.

A small number of light red products were prepared at 90 °C. The morphologies were relatively smooth selenium spheres with a diameter of about 500 nm, as shown in **Figure 5(a)**. At 110 °C, slender selenium filaments grow on the surface of some selenium pellets. The surface of these selenium pellets is uneven, and the protrusions are suspected to be selenium buds without growth and formation, as shown in **Figure 5(b)**. At 130 °C, selenium filaments increased significantly, and selenium appeared as shown in **Figure 5(c)**. The products prepared at 150 °C contained both smooth selenium balls and a selenium ball with large selenium buds, shaped like sea urchins, as shown in **Figure 5(d)**. When the reaction temperature was set at 170 °C, the selenium pellets disappeared and the products turned into large particles bonded together, as shown in **Figure 5(e)**.

Relevant studies have shown that β-CD has different inclusion ability at different temperatures[7]. At low temperature, β-CD has a strong inclusion ability for (quasi-) metallic elements, and it is easy to obtain selenium pellets with large particle size under the guidance of β-CD limit, as shown in **Figure 5(a)**. With the increase of reaction temperature, the solubility of β-CD increases, which is conducive to the formation of cysteine-cyclodextrin copolymerization hydrogel that can better disperse and stabilize selenium grains, resulting in the emergence of fine selenium buds and selenium branches, as shown in **Figure 5(b)** and **(c)**[8]. However, heating also has adverse effects: on the one hand, it will intensify the thermal movement of grains, increase the probability of collision and binding of crystal nuclei, and destroy the stability of β-CD soft template on selenium grains, resulting in the fusion of small selenium filament and selenium bud, and selenium bud becomes significantly thicker. As shown in **Figure 5(d)**, Johnson's sintering model shows that reaction temperature has a great influence on grain growth, and grain agglomeration will become more serious with increasing sintering temperature[9]. Therefore, high temperature causes selenium crystals to "sinter" together, as shown in **Figure 5(e)**.

According to the above facts, the optimum temperature for the growth of selenium was determined to be 130 °C.

3.5 Effect of reaction time on product morphology

Using the experimental method described in step 2.2, the amount of fixed template agent β-CD solution (0.5 g/L) was 8.0 mL, and the reaction temperature was set at 130 °C. The reaction time was set as 0.5, 1, 2, 3 and 4 h, respectively, and the single-factor comparison test was conducted. The products obtained were repeatedly cleaned by ultrasonic and detected by SEM, as shown in **Figure 6(a)** to **Figure 6(e)**.

The products prepared by reaction of 0.5 h are selenium balls of different sizes, as shown in **Figure**

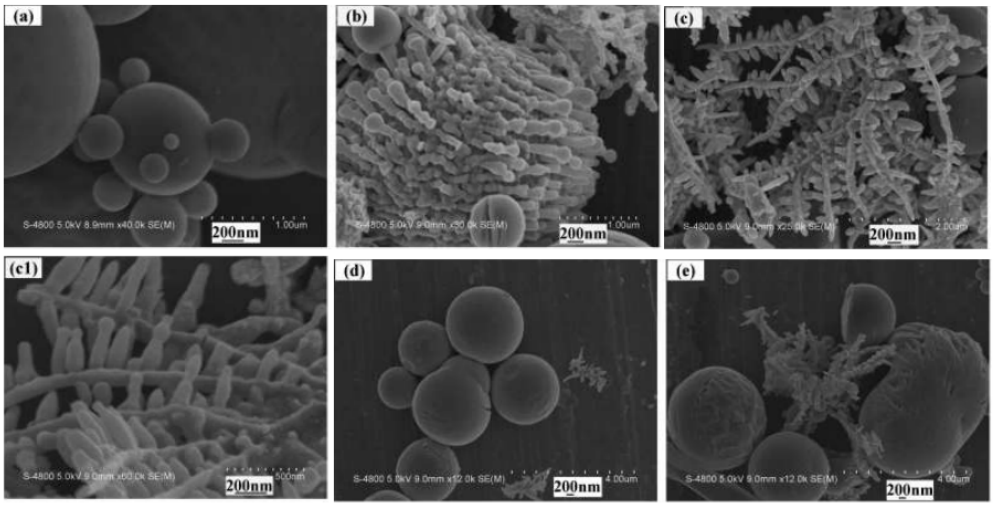

Figure 6. Effect of reaction time on the morphology of products.

6(a). After heating for 1 h, a large number of selenium buds appeared, as shown in **Figure 6(b)**. After 2 h of reaction, selenium buds grew and cross linked with each other, and a large number of selenium shoots began to emerge, as shown in **Figure 6(c)** and **Figure 6(c1)**. After reaction for 3 h, there were few selenium buds, selenium filaments and selenium branches, and cracks appeared on the surface of selenium ball, as shown in **Figure 6(d)**. After heating for 4 h, the selenium pellets continued to increase, and the diameter was 2–4 μm. The selenium sticks were obviously stuck together, as shown in **Figure 6(e)**. The morphology was not significantly different from that of the product after heating for 3 h.

The reason for the above changes may be that *β*-CD can self-assemble into supramolecular shells through adsorption and hydrogen bonding, but this process requires time, and prolonged reaction time is conducive to *β*-CD self-assemble into supramolecular shells[10]. Under the guidance of *β*-CD supramolecular shells, selenium crystals grow in a limited position in this three-dimensional template, and finally the dendritic selenium with neat appearance is obtained. However, at higher temperatures, the long-term reaction will lead to aggregation and fusion of small-scale products. Gao Shanmin *et al.* pointed out that there is a competitive process of grain dissolution and crystallization in the reaction system[11]. If the reaction time is prolonged at a higher reaction temperature, the crystallization speed will gradually exceed the dissolution speed, resulting in the gradual reduction of small grains, the continuous settlement of large grains, the smaller and smaller suspended grains in the solution, and the product has an obvious tendency of floccumulation.

Based on the above facts, the optimum reaction time for selenium growth was determined to be 2 h.

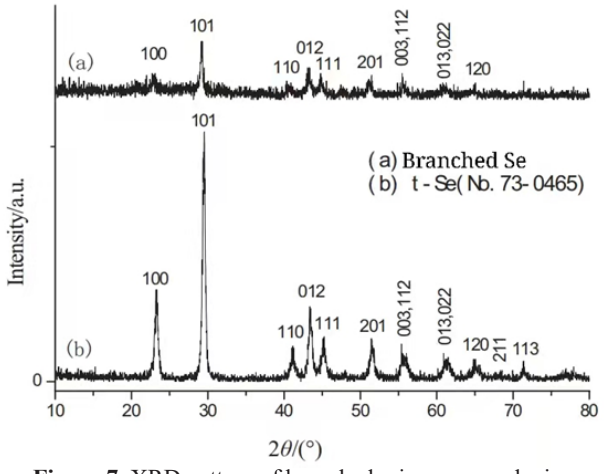

Figure 7. XRD pattern of branched micro nano selenium.

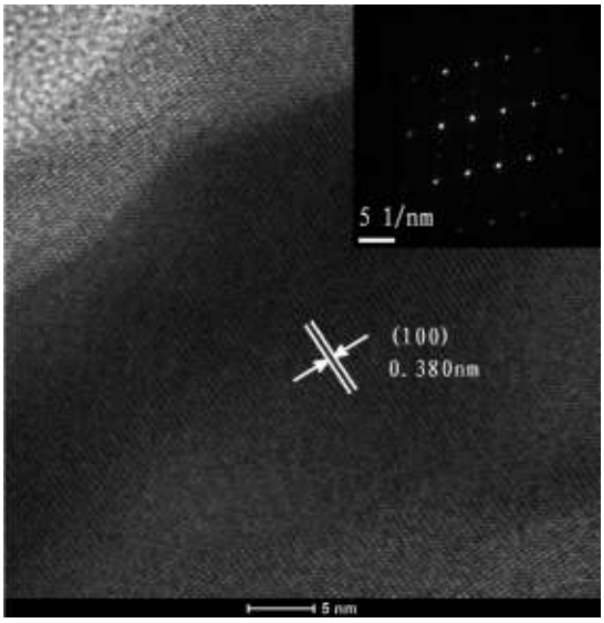

Figure 8. HRTEM spectra of branched micro nano selenium.

3.6 XRD and TEM characterization

The branched selenium prepared under the corresponding experimental conditions in **Figure 6(c)** was naturally dried and made into powder. Dandong Y-4Q X-ray diffrotometer was used for detection. The XRD pattern (**Figure 7**) showed that the absorption peak intensity was weak, but the background intensity was large. The whole peak shape was basically consistent with the tripartite selenium absorption peak data in JCPDS card (No.73-0465), and only a few weak absorption peaks could not be displayed. **Figure 8** shows the HRTEM (high resolution transmission electron microscopy) pattern of the dendritic selenium. The illustration shows the SAED (selective electron diffraction) pattern of the corresponding region. The aperture diameter is 0.1 μm, and the diffraction pattern shows that the product has a single crystal structure. The crystal lattice fringes in **Figure 8** are clear, indicating that the product has good crystallinity. The distance between adjacent crystal planes is about 0.380 nm, which is very close to that of t-Se (100) crystal plane at 0.3781 nm. The above

detection indicated that the prepared selenium was tripartite t-Se under experimental conditions, and the micro-nano Se^0 of such a dendritic structure had not been reported in the literature before.

4. Conclusions

The results showed that the reducibility of L-Cys•HCl was weak, and the yield of selenium was not high. *β*-CD soft template has a great influence on the morphology of selenium nanoparticles. *β*-CD has hydrophilic outer surface and hydrophobic inner surface, under the combined action of hole effect, coordination effect and steric hindrance effect, it can effectively inhibit the growth and agglomeration of selenium nuclei, slow down the growth rate of selenium nuclei, promote the rapid nucleation and slow growth of selenium crystals, and finally obtain dendritic selenium with unique morphology. Selenium spheres with large particle size also appeared in the test. According to the hydrogen bond theory explaining powder agglomeration, the hydrogen bond initiated by hydroxyl group is the root of hard agglomeration[12]. *β*-CD, as a macromolecular, contains a lot of hydrogen bonds, and its ability as a soft template to stabilize nanoparticles is weaker than that of anionic surfactant. Hence, the particle size of selenium crystal prepared with *β*-CD as template is large. In this study, the amount, reaction temperature and reaction time of *β*-CD have different effects on the morphology of the product. After comparison, the most suitable reaction conditions for the growth of branch selenium are as follows: adding in 0.6306 g L-Cys•HCl in turn 8.0 mL of *β*-CD solution (0.5 g/L), 80 mL of H_2SeO_3 solution (0.05 mol/L), and *n* (L-Cys•HCl): *n* (H_2SeO_3) = 1:1 in the reaction system. After the reaction kettle is shaken evenly, it is placed in a blast drying oven and heated at 130 ℃ for 2 h to prepare gray products. The gray products are cleaned for many times with deionized water and industrial alcohol, centrifuged and naturally dried to obtain dendritic micro nano selenium.

Conflict of interest

No conflict of interest was reported by the author.

Acknowledgements

Project: provincial key research project of Natural Science in Anhui province “Preparation and Properties of Nano-selenium Compound Nutrition Sustained-release Agent” (KJ2014A246).

References

1. Du Y, Liu X. Research progress of trace element selenium (in Chinese). Studies of Trace Elements and Health 2007; (3): 56–58.
2. Li L, Lin Q, Chen H. The biological functions of selenium and research development of Se-enriched foodstuff. Modern Food Science & Technology 2005; 21(3): 198–200.
3. Wu Y. Study on the sustained-release profile of nano selenium chitosan composite. Science and Technology of Food Industry 2012; (22): 141–146.
4. Wu Y, Ni Y. Low temperature rapid preparation of selenium nanostructures in the presence of food surfactants. Chemical Engineering Journal 2012; (187): 328–333.
5. Hua P. Preparation and application of selenium nano-particles [Master’s Thesis]. Baoding: Hebei University; 2009. p. 53.
6. Li L, Sun X, Yang Y, *et al.* Synthesis of anatase TiO_2 nanoparticles with beta-cyclodextrin as a supramolecular shell. Chemistry–An Asian Journal 2006; 1(5): 664–668.
7. Sun Y, Xia D, Xiang Y. Influence of temperature on the inclusion of *β*-Cyclodextrin with various mercaptans. Chinese Journal of Applied Chemistry 2007; (10): 1201–1205.
8. Liu Y, Fan X. A novel hydrogel prepared from water-soluble *β*-Cyclodextrin macromonomer and N-isopropylacrylamide. Polymeric Materials Science & Engineering 2004; (2): 77–80.
9. Johnson DL. New method of obtaining volume, grain boundary and surface diffusion coefficients from sintering data. Journal of Applied Physics 1969; 40(1):192–200.
10. Sun X, Zheng C, Zhang F. Synthesis of $BaTiO_3$ nanocrystals with *β*-Cyclodextrin as a supramolecular shell. Chinese Journal of Inorganic Chemistry 2008;

(1): 93–97.
11. Gao S, Sun S, Cui D, *et al.* Influence of water and oxygen in the media on the process of benzene-thermal synthesis of GaP nanocrystals. Acta Chimica Sinica 2000; (6): 643–646.
12. Han BH, Polarz S, Antonietti M. Cyclodextrin-based porous silica materials as in situ chemical "nanoreactors" for the preparation of variable metal-silica hybrids. Chemistry of Materials 2001; 13(11): 3915–3919.

Characterization and Application of Nanomaterials (2021) Volume 4 Issue 2
doi:10.24294/can.v4i2.1334

REVIEW ARTICLE

Review of super-hydrophobic materials research

Chengbao Liu[1,2*], Minjia Li[1], Xiaojie Liu[1,2], Zhigang Chen[1,2]

[1] *School of Chemistry, Biology and Materials Engineering, Suzhou University of Science and Technology, Suzhou 215009, Jiangsu Province, China. E-mail: lcb@mail.usts.edu.cn*

[2] *Jiangsu Key Laboratory for Environmental Functional Materials, Suzhou 215009, Jiangsu Province, China*

ABSTRACT

We reviewed the research on super-hydrophobic materials. Firstly, we introduced the basic principles of super-hydrophobic materials, including the Young equation, Wenzel model, and Cassie model. Then, we summarized the main preparation methods and research results of super-hydrophobic materials, such as the template method, soft etching method, electrospinning method, and sol-gel method. Among them, the electrospinning method that has developed in recent years is a new technology for preparing micro/nanofibers. Finally, the applications of super-hydrophobic materials in the field of coatings, fabric and filter material, anti-fogging, and antibacterial were introduced, and the problems existing in the preparation of super-hydrophobic materials were pointed out, such as unavailable industrialized production, high cost, and poor durability of the materials. Therefore, it is necessary to make a further study on the application of the materials in the selection, preparation, and post-treatment.

Keywords: Super-hydrophobic Materials; Basic Principles; Preparation Method; Application

ARTICLE INFO

Received: 22 June 2021
Accepted: 14 August 2021
Available online: 21 August 2021

1. Introduction

Super-hydrophobic material refers to a material with a contact angle of the material surface and water greater than 150° and a rolling angle less than 10°[1,2]. In nature, many plant foliage and waterfowl feathers have super-hydrophobic water characteristics, such as dragonfly wing[3], water strider leg[4], lotus leaf[5], etc. (**Figure 1**), among which the most typical is the "lotus leaf effect". The surfaces of these moving, plants contain special geometry with contact angles with water above 150°. In the lotus leaf[6–8], the lotus leaf surface (**Figure 2**) is composed of many papillae with an average diameter of 5 to 9 m, and the contact and rolling angles of water on that surface are (161.0 ± 2.7)° and 2°, respectively[6–8]. Each papilla is composed of a nanostructured branching with an average diameter of (124.3 ± 3.2) nm. These nanostructures on micromastoid especially, play an important role in super-hydrophobicity.

Figure 1. Dragonfly wings **(a)**, water strider legs **(b)**, lotus leaf **(c)**.

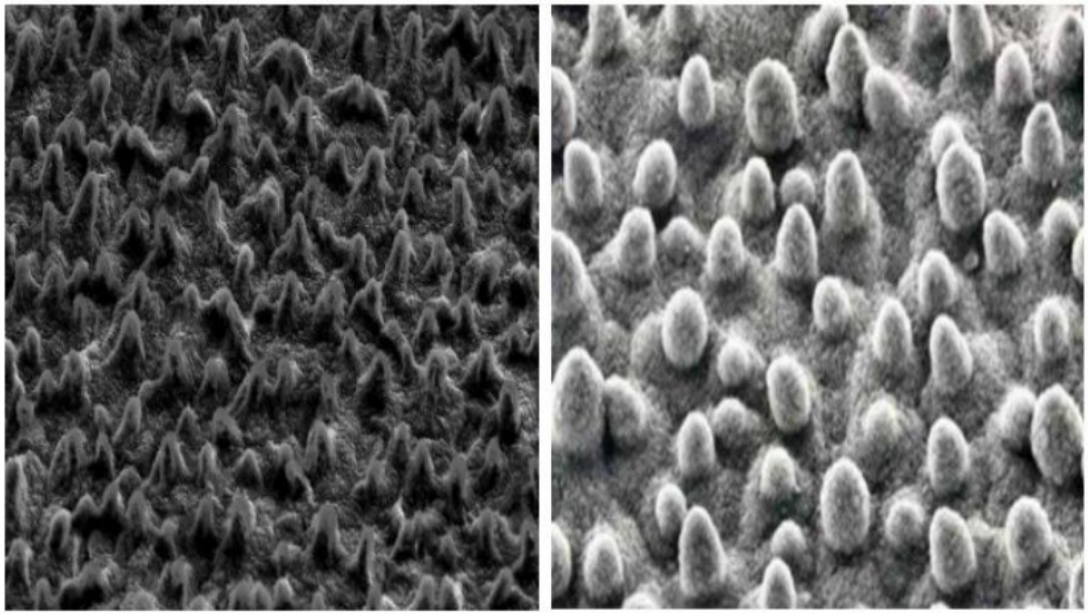

(a) SEM plot of the surface of the lotus leaf (b) SEM plot of high magnification

Figure 2. Microstructure of the surface of the lotus leaf.

Through the research, people do not only find many super-hydrophobic phenomena in nature and their surface structures but also make artificial synthetic super-hydrophobic surfaces by various methods. At present, there are two ways to prepare super-hydrophobic surfaces[9]: (1) modification of low surface energy material on a surface with micro-nano rough structure; and (2) construction of a micro-nano rough structure on the surface of the material with low surface energy.

In recent years, the preparation of super-hydrophobic surface materials with biological tissues and structures as bionic objects has become one of the hotspots in the field of material research. Jiang Lei research group is the first research group involved in this field in China. Their main preparation methods are the template method, soft etching method, electrospinning method, and at present, its research focus is ultra-super-hydrophobic materials, namely ultra-hydrophobic ultra-hydrophobic oil. It will introduce the super-hydrophobic materials from the basic principles of super-hydrophobic water, its preparation method and its application.

2. The rationale of super-hydrophobic water

The wettability of the solid surface is mainly determined by the chemical composition of the solid surface and surface microstructure. The wettability of the solid liquid, that is, hydrophilic and hydrophobicity is generally expressed by the contact angle θ of the liquid and solid phase. The shape formed when the droplet stays on a smooth solid surface by the droplet on its surface is determined by the interface tension of the three-phase contact surface of the solid, liquid and gas, whose contact angle can be described by the Young equation[10]:

$$\cos\theta = (\gamma_{SA} - \gamma_{SL})/\gamma_{LA} \quad (1)$$

γ_{SA}, γ_{SL} and γ_{LA} represent the interface tension of solid-gas, solid-liquid and liquid-gas individually. At this time, the three surface tension interactions are at equilibrium.

But the Young equation is an idealized model suitable only for ideally smooth solid surfaces. If it is a solid surface with a certain roughness, there are some D-value between the apparent and intrinsic contact angles. The actual contact area of solid and liquid is more than the apparent contact area. The droplets fully enter the empty groove of the rough surface structure. Therefore, it must consider the impact of roughness on the hydrophobic performance. At present, Wenzel model[11] and Cassie model[12] are

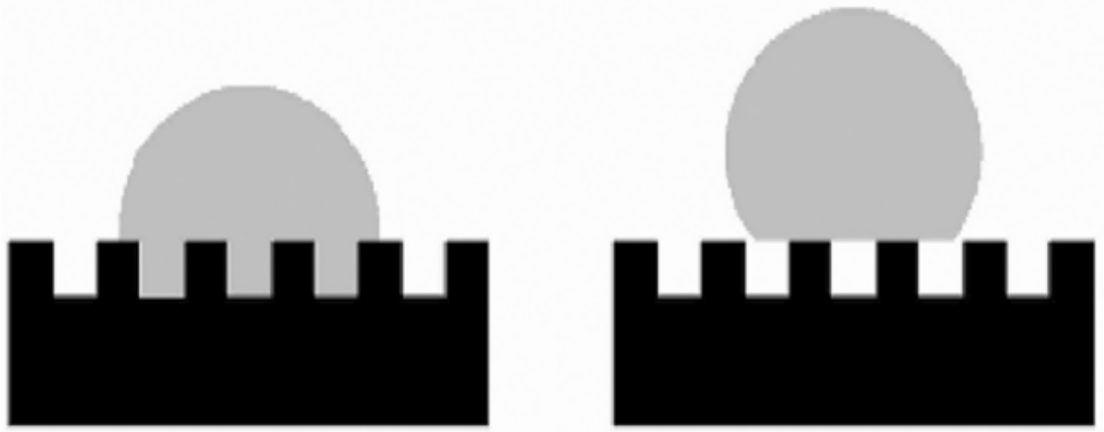

Figure 3. Schematic diagram of the Wenzel and Cassie models[13].

relatively mature in the related basic theoretical research. The schematic diagram shows in **Figure 3**.

2.1 Wenzel model

The Wenzel model considers that the droplets contact with the solid surface, and infiltrate into the surface groove. It increases the surface contact area, and the apparent geometrically observed contact area is less than the actual solid-liquid contact area when the apparent contact angle is greater than the intrinsic contact angle:

$$\cos\theta_w = r(\gamma_{SA} - \gamma_{SL})/\gamma_{LA} = r\cos\theta \quad (2)$$

In the formula, r is the surface roughness factor, the ratio of the actual surface area to the projected area, and θ_w is the apparent contact angle of the rough surface.

From Equation (2), increasing the value of the surface rough factor r can make the original hydrophobic surface more hydrophobic. However, the Wenzel model also has its limitations, which do not apply in the case of solid surfaces composed of different types of chemicals.

2.2 Cassie model

The Cassie model suggests that water droplets are suspended on solid surface convex grooves and that liquid droplets fall on a composite phase composed of solid-liquid and solid-gas interfaces. Therefore, its equation is:

$$\cos\theta' = f_1\cos\theta_1 + f_2\cos\theta_2 \quad (3)$$

θ' is the apparent contact angle in the Cassie model, f_1 and f_2 are the ratio of liquid contact to the solid surface and air, respectively, and 1 and 2 are the contact angles of liquid to solid surface and air, respectively. Where $f_1 + f_2 = 1$, $2 = 180°$, the formula (3) can be written as:

$$\cos\theta' = f_1\cos\theta_1 - f_2 = f_1\cos\theta_1 + f_1 - 1 \quad (4)$$

From the above model, preparing a surface with a special structure can improve the contact angle of the surface. The Cassie model suggests that droplets are suspended on solid surface convex grooves and do not seep into the surface topography. In the Cassie model, droplets are usually scrollable on the surface.

The Wenzel and Cassie models provide a strong theoretical basis for the preparation of super-hydrophobic surfaces, and although they are currently under some controversy[14,15].

Moreover, the contact angles in the above three cases characterize the performance of water droplets on the horizontal surface and are more oblique in reality. The state of the droplet on the slope can be characterized by the rolling angle, the critical surface tilt angle of the drop when the droplet begins to roll on the solid surface. The smaller tilt angle if the droplet begins to roll indicates that the super-hydrophobic water on this surface is better[16].

In conclusion, the contact and rolling angles jointly characterize the mutual permeability of the solid-liquid and the hydrophilic-hydrophobicity exhibited. The larger contact angle and the smaller rolling angle indicate the stronger hydrophobicity of the material surface[17–19].

3. Preparation method of super-hydrophobic materials

3.1 Template method

The template method takes a substrate with a cavity structure as a template, and covers the casting film liquid on the template by dumping, casting and spin coating. The proposed method has the advantages of simplicity, effectiveness and large area replication, and has good application prospects in practice.

Zheng Jianyong *et al.* used calcium carbonate particles to form a polymer super-hydrophobic surface by thermal pressure and acid etching[20]. After the test, its droplet static contact angle reached 152.7° while its rolling angle was < 3°.

Liu *et al.* coated a PDMS film with candle soot as a template, and calcination removed the template to form super-hydrophobic fiberglass cotton with a rough fiber mesh surface on the glass substrate[21]. After detection, the material has a contact angle with the water of up to 163° and can be used to optimize oil-water separation and air filtration, showing excellent thermal stability.

Ke *et al.* took taro leaves as the parent plate, constructed the surface structure with subtle cavity by template method, and then modified by an impregnated coating method, which significantly improved the hydrophobic performance[22].

3.2 Etching method

Etching technology refers to the process of etching the target surface into a micro rough appearance by physical or chemical methods. Laser etching, plasma, chemical and, photo etching are several commonly used micro etching methods. The etching method can make more accurate operation and design of the surface structure to regulate surface hydrophobicity. While the cost is high, and it is not suitable for large-scale production.

Qi *et al.*[23] used the chemical etching method assisted by metal ions (e. g., Ag^{+}, Cu^{2+}, Cr^{3+}) to process Zinc substrate to get rough structure surface, and the water contact angle measured by fluoro silane modification is up to (161 ± 2)°. In addition, they explored the effects of different metal ions on the surface morphology and hydrophobic properties, and then they found that the addition of metal ions could enhance the strength and stability of the super-hydrophobic surface.

Sung-Woon *et al.*[24] took SF_6 as a plasma source, obtained with the plasma etching method, and then C_4F_8 as a plasma source, and then a carbon-fluorine membrane was deposited on the silicon surface with a micron-grade rod structure. After testing, the contact angle with water is 165°.

3.3 Phase separation method

The phase separation method is the membrane form in which the system produces two or multiple phases during the control conditions. This method is easy to regulate and simple to operate. It can prepare uniform and large areas of superhydrophobic films, which has great value in practical aspects.

Liu *et al.*[25] put butyl methacrylate (BMA) and glycol dimethyl acrylic (EDMA) in a mixture of 1, 4-cis-butanediol (BDO) with N-methyl-pyrrolidone (NMP) to in situ polymerization. A super-hydrophobic porous polymer surface with a micro-nano rough structure with a water contact angle of 159.5° and a rolling angle below 3.1°.

Liu Jianfeng *et al.*[26] used butyl methyl acrylate (BMA) and ethylene glycol dimethyl acrylate (EDMA) as monomers and azo diisonitrile (AIBN) as an initiator for thermal polymerization on the glass substrate, thus forming a micro/nanocomposite roughness structure on the surface with a static water contact angle of up to 159.5°.

3.4 Chemical vaporous deposition

Chemical vapor deposition is a simple, efficient, inexpensive, and effective method, which prepares rough structures without the limitation of substrate shape.

Deng Tao *et al.* prepared aligned dense nanowire structures on silicon wafers by chemical vapor deposition[27]. They placed washed silicon wafers in inductively coupled plasma bins, deposited silicon nanowires while etching, and then modified them with fluoro silane to create a silicon nanowire surface structure with a line width of about 100 nm.

3.5 Electrospinning method

Electrospinning is a new technology to prepare micro/nanoscale fibers. It places a polymer solution or melt in a high-pressure electrostatic field, and is stretched under the electric field Coulomb force to form a jet fine flow that falls on the substrate to form a micro/nanofiber membrane.

Jiang Lei *et al.*[28] used electrospinning technology to build a rough surface and then used cheap low surface-energy silicon oil during calcination to prepare TiO_2 super-hydrophobic surfaces with a contact angle greater than 150° and a rolling angle less than 5°.

Huang *et al.*[29] constructed a coating with SiO_2 nanoparticles and silicic acid solution. They adjusted the roughness of the coating by changing the ratio of SiO_2 nanoparticles and silica acid. The coating was modified by perfluorooctyl trichlorosilane with a water contact angle of 160°, less than 10°. It also has high light transmittance, excellent thermal stability and mechanical stability. However, when the organic modifier of the coating surface contacts water for a long time, the turnover of its hydrophilic group results in poor hydrophobic stability, increasing the uncertainty in its practical application.

Li Fang *et al.*[30] used polyvinylidene difluoride (PVDF) and N, N-dimethylformamide (DMF) as the test materials, and prepared the ultra hydrophobic material with hollow microsphere structure by electrospinning. and the ultra hydrophobic material has super lipophilic properties. The contact angle between the material and the water was 153.5°.

3.6 Layer upon layer assembly method

Layer assembly technology refers to the technology of membrane layer by layer deposition under the action of electrostatic action, hydrogen bonding, and coordination bonding. Zhang Qunbing, Wang Jun *et al.* of Ningbo University used layer by layer assembly method to prepare the superhydrophobic surface of sea urchin TiO_2 with silicon sheet as the substrate[31]. The contact angle of the surface was 151.2° and a rolling angle of 4.5°.

Shang *et al.*[32] used polypropylene dimethyl ammonium chloride (PDDA) and poly4-styrene sodium sulfonate (PSS) as the polyelectrolyte, and then dipped the glass in the polyelectrolyte solution. Then dipped it in polystyrene modified SiO_2 particle suspension. Finally, a high transparent superhydrophobic porous SiO_2 glass coating made from perfluoroctane by chemical gas deposition, measuring water contact angle greater than 150° and a rolling angle of less than 10°.

3.7 Sol-gel method

The sol-gel method is a preparation method for condensing the solvent obtained after hydrolysis of high chemical activity compounds and drying the resulting gel to form a micro/nanopore structure to make it superhydrophobicity, but there are disadvantages such as long preparation process route, poor surface structure control, and solvent contamination.

Sanjay *et al.*[33]. prepared a methyl triethoxysilane (MTES) and porous silicon membrane into superhydrophobic surfaces with contact angles up to 160° on a glass substrate by solvent-gel method It is shown that the superhydrophobic films prepared by this method are transparent, adherent, good thermal stability and moisture resistant.

Wei *et al.*[34] used potassium titanate and TEOS as precursors and used a solvent-gel method to prepare a perfect titanium-silicon mesh composite aerosol structure, and the water contact angle of aerogel samples obtained after trimethylchlorosilane modification reached (145 ± 5)°.

After Zheng Yansheng *et al.*[35] hybridized TFE with a SiO_2 solvent modified by epoxy propoxy propyl trimethoxysilane, the glass was coated with a hyper-hydrophobic coating with a contact angle of up to 156°.

3.8 Electrochemical deposition method

Su *et al.*[36] deposit a layer of nickel on the copper substrate, and then fluoro silane modification yields a superhydrophobic surface with a contact angle of 162°. The material is capable of maintaining superhydrophobic by moving 1 m on silicon carbide (SiC) sandpaper for 800 at a load pressure of 4.8 kPa, indicating that the surface has excellent micro

hardness and mechanical wear resistance.

Ding, *et al.* used electrochemical method, and deposited a layer of micro/nanostructure copper oxide (Cu_2O) membrane on the conductive glass (ITO) surface. It has a water contact angle up to about 170°, achieving a superhydrophobic effect. Meanwhile, it could obtain the Cu_2O films of different micromorphology by regulating electrodeposition time.

Xu *et al.*[38] electrochemical deposition of Tridecafluoroctyl triethoxysilane (POTS) on a films of poly pyrene and SiO_2 prepared a superhydrophobic complex coating of petal micronano layered structures highly transparent, thermal and mechanical stability with a static water contact angle up to (163 ± 1)° and a rolling angle below 2°

Hyper hydrophobic ZnO films were prepared on an aluminum alloy substrate after Huang *et al.*[39] functionally tionalized nanoZnO to 0. 01 $mol \cdot L^{-1}$ stearate ethanol solution, a mixture of isopropanol and butanol. It found that the roughness of the surface and the water contact angle of the surface gradually increased with the deposition temperature, and the film obtained at 50 ℃ had excellent superhydrophobic properties, with a water contact angle reaching (1553)°.

3.9 Solution immersion method

Li *et al.*[40] first impregnated the aluminum alloy plate in lanthanum nitrate aqueous solution for heat treatment to form a nano structure similar to Ginkgo biloba leaves on the surface, and then modified the super hydrophilic aluminum alloy surface with Dodecafluoroheptyl propyl trimethoxysilane. The water contact angle reached 160°, and the superhydrophobic surface had a relatively good surface Strong thermal stability, corrosion resistance, wear resistance and other advantages.

Yao Jiannian *et al.*[41] prepared superhydrophobic materials by solution soaking. After first soaking the smooth copper sheet in a specific $[Ag(NH_3)_2]OH$ solution for 6 h, a structure similar to the rose petals could appear on the surface of the copper sheet, and its contact angle reached 156°.

3.10 Other methods

Yang and *et al.*[43]were prepared by microemulsion, then heated on a glass plate to form porous rough structural films during the volatile process, and then modified with Xinji trimethoxysilane to make honeycomb-like superhydrophobic films with a contact angle of 156.3°, which is simple, fast and economical[42]. Furthermore, inspired by the microstructure of plant leaf surfaces, researchers like Liu *et al.* prepared superhydrophobic surfaces with a high contact angle of around 170° and a rolling angle of about 6° on an aluminum alloy by a one-step anodized method.

4. Application of hytra hydrophobic materials

Hyper hydrophobic materials have self-cleaning, pollution resistance and other characteristics, therefore, superhydrophobic materials can be developed and applied, so that they have broad prospects in the fields of aerospace and military industry, agriculture, pipeline nondestructive transportation, housing construction, as well as the equipment working in various open-air environments.

4.1 Application of superhydrophobic materials in fabric and filter materials

Various micronanostructural fibers with superhydrophobic water are produced by electrophospinning or treatment of the material surface to obtain anti-polluting superhydrophobic fabrics. Such materials can be used to make waterproof film, hydrophobic filter film, etc., or make the fabric have new functions such as hydrowaterproof, pollution prevention and dust prevention due to hydrophobic properties. For example, Xue *et al.* creates a friction-resistant superhydrophobic fiber fabric coating with sodium hydroxide etched polyethylene terephthalate (PET) fiber fabric[44].

4.2 Application of superhydrophobic materials in building coatings

Due to their unique hydrophobic properties, superhydrophobic materials have wide application prospects in water resistance, snow prevention and pollution resistance. At present, the ultra-hydropho-

bic surface materials in building pollution prevention materials are mainly coating and protective fluid, for example, Ji Haiyan, Chen Gang *et al.*[45] using etching glass also prepared ultra-hydrophobic glass surface. Yang *et al.*[46] developed a modified dodecthiol ZnO/PDMS complex with a water contact angle of 159.5° and 8.3° and excellent ice resistance at –10 and –5 ℃, showing great potential for application.

4.3 Application of superhydrophobic materials in fog prevention and self-cleaning

Liquidation of water vapor in the air forms water mist covering the surface of transparent materials such as glass can cause reduced visibility of these materials[47]. Some bionic ultra-hydrophobic surface effectively reduce the condensation of water vapor, to achieve a certain anti-fog, self-cleaning effect. After alternating self-assembly of raspberry polystyrene and SiO_2 particles on slides, a highly transparent porous SiO_2 coating was obtained by high-temperature calcination. Finally, an ultra-hydrophobic transparent coating was obtained by chemical vapor deposition with a water contact angle of (1592)°. The coating improves the evaporation rate of water mist with excellent anti-fog performance.

4.4 Application of superhydrophobic surface materials in metal anticorrosion protection

Hyperhydrophobic materials have corrosion-resistant properties because a membrane of air occurs between solid and liquid, making it difficult for corrosive ions to contact the surface of the material[49,50].

Many people have researched in this regard, such as Guo Haifeng *et al.*[51] praying the inner surface of the natural gas pipeline to prepare superhydrophobic films to further improve the corrosion resistance of the pipeline. The subject group, Lu Si *et al.*, adhered the disordered carbon nanotubes to the surface of the substrate aluminum plate to form a composite structure surface and then modified with PTFE to form a hyper-hydrophobic PTFE.

4.5 Application of superhydrophobic surface materials in other aspects

Mobina *et al.*[52] co-modified the trimonomomer copolymer with methanol and nano SiO_2 and the water contact angle of the composite superhydrophobic coating was greater than 150° and could be applied to the surface of biomedical materials.

Wang *et al.*[53] immersed aluminum alloy, silicon plates, polypropylene and other substrate in a buffer of dopamine-hydrochloride for a period, transferred to different concentrations of silver ammonia solution, added formaldehyde solution, and finally modified the substrate into a mixture of ethanol and dodecyl thiol to make a superhydrophobic silver substrate with a water contact angle up to 170°.

5. Conclusion

The application range of superhydrophobic materials is quite wide, which has had certain development in various aspects, and its application prospect is very broad. However, due to the current technology and development costs are limited, the actual industrialization and commercialization are not much[54,55]. First, from a theoretical perspective, the geometry of superhydrophobic, size, functional group influence of superhydrophobic surface structure needs to be deepened. Secondly, in the preparation process, the low surface energy substances used are more expensive, mostly fluoride or silane compounds. Finally, in terms of technology, it is mainly the durability and aging resistance of surface coating. Many superhydrophobic structures are prone to lose superhydrophobicicity due to infirmness. Therefore, in the selection of materials, preparation process and post-processing, further research and solution. Research on how to automatically recover or regenerate superhydrophobic surfaces after reduced or disrupted performance will be an important research direction in this field.

Conflict of interest

The authors declare that they have no conflict of interest.

Acknowledgements

Fund Project: National Natural Science Foundation Grant Project (51478285); Natural Science Foundation of Jiangsu University Grant Project

(14KJA430004); Suzhou Science and Technology Development Plan Project (SYG201742); Jiangsu University Water Treatment Technology and Material Collaborative Innovation Center Project.

References

1. Manatunga DC, Silva RMD, Silva KMND. Double layer approach to create durable superhydrophobicity on cotton fabric using nano silica and auxiliary non fluorinated materials. Applied Surface Science 2016; 360: 777–788.
2. Brassard JD, Sarkar DK, Perron J. Studies of drag on the nanocomposite superhydrophobic surfaces. Applied Surface Science 2015; 324: 525–531.
3. Darvizeh M, Darvizehv A, Rajabi H, *et al.* Freevibration analysis of dragon fly wings using finite element method. The International Journal of Multiphysics 2009; 3(1): 101–110.
4. Khila A, Abouheif E, Rowe L. Evolution of a novel appendage ground plan in water striders is driven by changes in the hox gene ultrabithorax. Plos Genetics 2009; 5(7): e1000583.
5. Barthlott W, Neinhuis C. Purity of the sacred lotus, or escape from contamination in biological surfaces. Planta 1997; 202: 1–8.
6. Xiao, Tian J, Zhang B, *et al.* Research progress of superhydrophobic self-cleaning coatings. Modern Paint & Finishing 2017; 20(3): 32–35.
7. Minehide Y, Naoki N, Hiroyuki M, *et al.* Theoretical explanation of the lotus effect: superhydrophobic property changes by removal of nanostructures from the suface of a lotus leaf. Langmuir the Acs Journal of Surfaces & Colloids 2015; 31(26): 7355–7363.
8. Meng LY, Soo JP. Superhydrophobic carbon -based materials: a review of synthesis, structure, and applications. Carbon Letters 2014; 15(2): 89–104.
9. Yang M, Zhang L, Jiang H, *et al.* Effect factors and fabrication of superhydrophobic surface. Science & Technology in Chemical Industry 2016; 24(4): 78–82.
10. Young RN. The bakerian lecture: experiments and calculations relative to physical optics. London: Philosophical Transactions of the Royal Society of London; 1804. p. 1–16.
11. Wenzel RN. Resistance of solid surfaces to wetting by water. Industrial and Engineering Chemistry 1936; 28: 988–994.
12. Cassie ABD, Baxter S. Wettability of porous surfaces. Transactions of the Faraday Society 1944; 40: 546–551.
13. Chen J, Wang J, Wang W, *et al.* Preparation and Application of Hyperhydrophobic Surface Materials. China Materials Progress 2013; 32(7): 399–405.
14. Gao L, Mccaetgy TJ. How wenzel and cassie were wrong. Langmuir 2007; 23: 3762–3765.
15. Chen H, G T, Zhang X, *et al.* Research progress of superhydrophobic surface. Chemical Research 2013; 24 (4): 434–440.
16. Wang B, Nian J, Tie L, *et al.* Theoretical advances in stable hyper-hydrophobic surfaces. Physical Journal 2013; 62 (14): 1–15.
17. Yu M, Chen S, Zhang B, *et al.* Why a lotus-like superhydrophobic surface is self-cleaning? An explanation from surface force measurements and analysis. Langmuir the Acs Journal of Surfaces & Colloids 2014; 30(45): 13615–13621.
18. Cao M, Guo D, Yu C, *et al.* Water-repellent properties of superhydrophobic and lubricant-infused "slippery" surfaces： a brief study on the functions and applications. Acs Applied Materials & Interfaces 2016; 8(6): 3615–3623.
19. Spori DM, Drobek T, Zurcher S. *et al.* Beyond the lotus effect: roughness infuences on wetting over a wide surface-energy range. Langmuir the Acs Journal of Surfaces & Colloids 2008; 24(10): 5411–5417.
20. Zheng J. Feng J, Zhong M. Polymer superhydrophilic/superhydrophobic surfaces were prepared by the $CaCO_3$ particle template method. Polymer Journal 2010; 1 (10): 1186–1192.
21. Liu X, Xu Y, Ben K, *et al.* Transparent, durable and thermally stable PDMS-derived superhydrophobic surfaces. Applied Surface Science 2015; 339(1): 94–101.
22. Peng P, Ke Q, Zhou G, *et al.* Fabrication of microcavity-array superhydrophobic surfaces using an improved template method. Journal of Colloid and Interface Science 2013; 395: 326–328.
23. Qi Y, Cui Z, Liang B, *et al.* A fast method to fabricate superhydrophobic suefaces on zinc substrate with ion

assisted chemical etching. Applied Surface Science 2014; 305(7): 716–724.
24. Cho SW, Kim JH, Lee HM, *et al.* Superhydrophobic Si surfaces having microscale rod structures prepared in a plasma etching system. Surface and Coatings Technology 2016; 306: 82–86.
25. Liu J, Xiao X, Shi WL, *et al.* Fabrication of a superhydrophobic surface from porous polymer using phase separation. Applied Surface Science 2014; 297(4): 33–39.
26. Liu J, Xiao X, Cai X. Preparation of superhydrophobic porous polymer coating via phase separation. Polymer Materials Science and Engineering 2013; 29 (10): 113–117.
27. Tao D, Varanasi KK, Ming H, *et al.* Nonwetting of impinging droplets on textured surfaces. Applied Physics Letters 2009; 94(13): 3109.
28. Jiang L, Wang L, Zhao Y, *et al.* Superhydrophobic TiO_2 nanofiber mesh membranes were prepared by electrospinning (in Chinese). Journal of Higher Chemistry 2009; 30(4): 731–734.
29. Huang W, Lin CS. Robust superhydrophobic transparent coatings fabricated by a low-temperature sol-gel process. Applied Surface Science 2014; 305(3): 702–709.
30. Li F, Jia K, Li Q, *et al.* Farbrication of superhydrophobic and superoleophilic PVDF nanofibers with hollow beads structure by electrospinng for the separation of separation of oil and water. New chemical materials 2016; 44(3): 223–225.
31. Zhang Q. Preparation and characterization of super-hydrophobic surface of micro-nanocomposite (in Chinese). Ningbo: Ningbo University; 2012.
32. Shang Q, Zhou Y. Fabrication of transparent superhydrophobic porous silica coating for self-cleaning and anti-fogging. Ceramics International 2016; 42: 8706–8712.
33. Sanjay S, Latthe IH. Porous superhydrophobic silica films by sol-gel process. Microporous and Mesoporous Materials 2010; 130(1-3): 115–121.
34. Wei W, Lu XM, Jiang D, *et al.* A novel route for synthesis of UV-resistant hydrophobic titania-containing silica aerogels by using potassiumtitanate as precursor. Dalton Transactions 2014; 43(25): 9456–9467.
35. Zheng Y, He Y, QingY, *et al.* Preparation of a SiO_2/polytetrafluoroethylene hybrid superhydrophobic coatings. Chemical Industry and Engineering Progress 2012; 31(7): 1562–1566.
36. Su F, Yao K. Facile fabrication of superhydrophobic surface with excellent mechanical abrasion and corrosion resistance on copper substrate by a novel method. ACS Applied Materials & Interfaces 2014; 6(11): 8762–8770.
37. Ding Y, Li Y, Yang L, *et al.* The fabrication of controlled coral-like Cu_2O films and their hydrophobic property. Applied Surface Science 2013; 266: 395–399.
38. Xu L, Tong F, Lu X, *et al.* Multifunctional polypyrene/silica hybrid coatings with stable excimer fluorescence and robust superhydrophobicity derived from electrodeposited polypyrene films. Journal of Materials Chemistry C 2015; 3(9): 2086–2092.
39. Huang Y, Sarker DK, Chen XG. Superhydrophobic nanostructured ZnO thin films on aluminum alloy substrates by electrophoretic deposition process. Applied Surface Science 2015; 327: 327–334.
40. Li L, Huang T, Jie J, *et al.* Robust biomimetic-structural superhydrophobic surface on aluminum alloy. Acs Applied Materials & Interfaces 2015; 7(3): 1449–9457.
41. Cao Z, Xiao D, Kang L, *et al.* Superhydrophobic pure silver surface with flower-like structures by a facile galvanic exchange reaction with $[Ag(NH_3)_2]$ OH. Chemical Communication 2008; 23(23): 2692–2694.
42. Yang T, Tian H, Chen Y. Preparation of superhydrophobic silica films with honeycomb like structure by emulsion method. Journal of Sol-Gel Science and Technology 2009; 49: 243–246.
43. Liu Y, Liu J, Li S, *et al.* One-step method for fabrication of biomimetic superhydrophobic surface on aluminum alloy. Colloids and Surfaces A: Physicochemical and Engineering Aspects 2015; 466: 125–131.
44. Xue C, Li Y, Zhang P, *et al.* Washable and wear-resistant superhydrophobic surfaces with self-cleaning property by chemical etching of fibers and hydrophobization. ACS Applied Materials & Interfaces 2014; 2014(6): 10153–10161.
45. Ji H, Gang C, Hu J, *et al.* Preparation and properties of monodisperse poly(ethyl methacrylate). New

Chemical Materials 2011; 39(8); 106–108.
46. Yang C, Wang F, Li W, *et al.* Anti-icing properties of superhydrophobic ZnO/PDMS composite coating. Applied Physics A 2015; 122(1): 1–10.
47. Shang Q, Zhou Y. Fabrication of transparent superhydrophobic porous silica coating for self-cleaning and anti-fogging. Ceramics Inter-national 2016; 42(7): 8706–8712.
48. Hou L, Fang L. Preparation and application development of superhydrophobic surface. Chemistry 2016; 79(10): 897–904.
49. Zhou Y. Preparation and properties of artificial bionic superhydrophobic functional surfaces [PhD thesis]. Beijing: University of Science and Technology of China; 2012.
50. Li H, Gu X, Liu L, *et al.* Advances in studying hyperhydrophobic surfaces (in Chinese). Applied Chemical Industry 2016; 45(12): 2347–2350.
51. Guo H, Zhang, Z, Li G, *et al.* Super-hydrophobic molecular film on the inner wall surface of steel for natural gas pipelines and its corrosion resistance. Oil & Gas Storage and Transportation 2011; 30(10): 781–784.
52. Xue C, Li Y, Zhang P, *et al.* Super-hydrophobic molecular film on the inner wall surface of steel for natural gas pipelines and its corrosion resistance. Oil & Gas Storage and Transportation 2011; (10): 781–784, 717.
53. Wang Z, Ou J, Wang Y, *et al.* Anti-bacterial superhydrophobic silver on diverse substrates based on the mussel-inspired polydopamine. Surface & Coatings Technology 2015; 280: 378–383.
54. Xu W, Song J, Sun J, *et al.* Progress in fabrication and application of superhydrophobic surfaces on metal substrates. Journal of Materials Engineering 2011; 1(5): 93–98.
55. Liang W, Zhang Y, Wang B, *et al.* Biological applications of biomimetic superhydrophobic surfaces. Acta Chimica Sinica 2012; 70(23): 2393–2403.

Characterization and Application of Nanomaterials

Focus and Scope

Characterization and Application of Nanomaterials (CAN) is an open access peer-reviewed journal allowing maximum visibility of articles published in it as they are available to a wide, global audience. We are interested in the scientific topics from all fields of nano. CAN provides a forum to share scholarly practice to advance the use of nanomaterials in the context of scientific application.

CAN publishes original research articles, review articles, editorials, case reports, letters, brief commentaries, perspectives, methods, etc.

Examples of relevant topics include but are not limited to:

1. Nanoparticle composites
2. Nanoscale quantum physics
3. Modeling
4. Simulation
5. Nanotechnology and its application
6. Nanochemistry
7. Nanoscience, nano-medicine and bio-nanotechnology
8. Nanomaterials and energy applications
9. Micro-nano scale
10. Fabrication of thin film
11. Nanomaterial synthesis, characterization, and application
12. Nanotechnology and environmental protection
13. Photocatalytic degradation properties
14. Preparation of nanostructured materials

EnPress Publisher, LLC

EnPress Publisher, LLC, is a scholastic conduit for an assembly of professionals in the domains of science, technology, medicine, engineering, education, social sciences and many more, as a roundtable for their intellectual discourse and presentation, and as an instrument to galvanize research designs, policy implementation and commercial interests, to facilitate the prevailing over their challenges and to encourage to the full advantage of their resources and true potential.

We are the intellectual and academic home for academic, educators, scholars, clinicians, corporate researchers, who all play important roles in a wide range of national and international research organisations, and whose interests, expertise, research approaches and industry objectives from around the world coalesce together to advance significant contributions in their research and professional fields.

As an instrument of information purveyor, we seek to combine academic rigor and originality with the nuanced development of policy and practice. Via our journals, client database, online campaigns and social media presence, we offer a platform for industry professionals to interconnect, as well as opening doors towards cost-effective solutions for them to succeed, and we confidently hope to inspire a new generation of multidisciplinary researchers, think-tank experts, policymakers and business entities to innovate and advance their knowledge across fields.

EnPress Publisher, LLC

Add: 14701 Myford Road, Suite B-1, Tustin, CA 92780, United States

Tel: +1 (949) 299 0192

Email: contact@enpress-publisher.com

Web: https://enpress-publisher.com